Structure and function of the membrane protein Opa60 by solid-state NMR

Dissertation

for the award of the degree

"Doctor rerum naturalium"

of the Georg-August-Universität Göttingen

within the doctoral program *"Biomolecules: Structure – Function – Dynamics"*

of the Georg-August University School of Science (GAUSS)

submitted by

Marcel Christian Forster

from Frankfurt am Main, Germany

Göttingen 2021

Thesis Committee

Prof. Dr. Christian Griesinger, NMR-based Structural Biology, Max Planck Institute for Biophysical Chemistry, Göttingen, Germany

Prof. Dr. Ralf Ficner, Molecular Structural Biology, Institute for Microbiology & Genetics (GZMB), Georg-August-Universität, Göttingen, Germany

Dr. Loren Andreas, Solid-State NMR Spectroscopy, Max Planck Institute for Biophysical Chemistry, Göttingen, Germany

Members of the Examination Board

Referee: Prof. Dr. Christian Griesinger, NMR based Structural Biology, Max Planck Institute for Biophysical Chemistry, Göttingen, Germany

2nd Referee: Prof. Dr. Ralf Ficner, Molecular Structural Biology, Institute for Microbiology & Genetics (GZMB), Georg-August-Universität, Göttingen, Germany

Further members of the Examination Board

Dr. Loren Andreas, Solid State NMR Spectroscopy, Max Planck Institute for Biophysical Chemistry, Göttingen, Germany (Name, Department/Group, Institution)

Prof. Dr. Markus Zweckstetter, Translational Structural Biology in Dementia, German Center for Neurodegenerative Diseases (DZNE), Göttingen, Germany

Prof. Dr. Helmut Grubmüller, Theoretical and Computational Biophysics, Max Planck Institute for Biophysical Chemistry, Göttingen, Germany (Name, Department/Group, Institution)

Prof. Dr. Marina Bennati, Electron-Spin Resonance Spectroscopy, Max Planck Institute for Biophysical Chemistry, Göttingen, Germany

Date of oral examination: 06/07/2021

Ich habe fertig.

Giovanni Trapattoni, 1998

Contents

Acknowledgments

I would like to thank Dr. Loren Andreas for giving me the opportunity to write this thesis and for his supervision, his willingness to always lend an ear to my questions and his constant positive attitude which kept me motivated. Thank you to Prof. Dr. Christian Griesinger for hosting me in his department and being part of my thesis advisory committee. Thank you to Prof. Dr. Ralf Ficner for being part of the committee. Moreover, I would like to thank Prof. Dr. Markus Zweckstetter, Prof. Dr. Helmut Grubmüller and Prof. Dr. Marina Bennati for their willingness to be part of my examination board.

Thank you to my collaborators from Prof. Dr. Kai Zhang's group – Shuang Wang and Hua Zhang. I also appreciated working with my students Dilaray Tüfekçi and Sudharsanan Srinivasan, and wish them all the best for their future. Thanks also to Anas Malki, with whom I worked and went to the gym for the gains.

This work would not have been possible without the support of the past and present members of the solid-state NMR group – Rıza Dervişoğlu, Yuliya Miloslavina, Evgeny Nimerovsky, Michele Salvi and Brigitta Angerstein. Thank you also to Melanie Wegstroth and everyone in the labs of NMRII for letting me work there and being always helpful. A very special thank you to my colleagues who have become close friends on the way – Xizhou Cecily Zhang, Vrinda Sant and Kai Xue. Worth a special mention in this context are Eszter Najbauer, for teaching me so many things on the spectrometer when I came here, and Kumar Tekwani Movellan, for teaching me everything in the lab, and for always being there to discuss even the smallest details. And, of course, most of all, for being good friends.

None of this would have been possible without my friends. There's the Frankfurt-gang, who is now dispersed over this planet – Tilman "Das war schon Diablo?" Hohenberger, Fritz Nieborowski, Yannick "Dr." Geiger and Patrick Grosmann. Thank you to Andreas "Du hast noch ein Getränk bei mir in der Tasche" Peter, for your constant and never-giving-up friendship. Thanks to Şerif Gören, whom I got to know during civilian service. Thanks to Ann-Sophie Frombach, for helping me survive the first two years in Göttingen. And thanks to Christina Weber and Christian Bengs for making the university and what came next a joy. Thank you, Alexander Hirschhäuser, for your constant friendship and the way we've come – I said I would include that, so here goes:

Manche sind gestorben, andere gingen weg
Doch wir hier haben einfach immer alles überlebt
Wir sind anders als die Anderen, auch wenn's keine Anderen gibt
Wir schwören uns immer wieder, dass das Beste vor uns liegt

Most importantly – thanks to Dhanya Ramachandran, you know, for existing and finding me and not ever stopping to motivate me, even when I would claim to "quit it all and forever". Who would have thought that in Bad Salzdetfurth…

Thank you to Brunhilde Schneider and Gerd Kratz for continuing to inspire and support me throughout my life. Thanks to my sister Natalie Wittmann and her husband Kai Wittmann, and Lukas and Linus, for making family visits a joy. And thank you to my parents, Gisela and Helmut Forster – it seems obvious, but nonetheless: for raising me to become who I am today.

List of abbreviations

CEACAM	CarcinoEmbryonic Antigen-Related Cell Adhesion Molecule
CP	Cross Polarization
CS	Chemical Shift
CSP	Chemical Shift Perturbation
CV	Column Volume
CYANA	Combined Assignment and dynamics Algorithm for NMR Applications
DARR	Dipolar Assisted Rotational Resonance
DMPC	1,2-DiMyristoyl-sn-glycero-3-PhosphoCholine
DMPE-PEG1000	1,2-DiMyristoyl-sn-glycero-3-PhosphoEthanolamine-N-[methoxy(PolyEthylene Glycol)-1000]
DMPG	1,2-DiMyristoyl-sn-glycero-3-Phospho-(1'-rac-Glycerol)
DNA	DesoxyriboNucleic Acid
DPC	DodecylPhosphoCholine
DREAM	Dipolar Recoupling Enhanced by AMplitude
DSS	2,2-Dimethyl-2-Silapentane-5-Sulfonate
E. coli	Escherichia coli
FLYA	FuLlY Automated structure determination of proteins in solution
GST	Glutathione S-Transferase
HSPG	HeparanSulphate ProteoGlycan
HSQC	Heteronuclear Single Quantum Coherence
HV	HyperVariable
INEPT	Insensitive Nuclei Enhanced by Polarization Transfer
IPTG	IsoPropyl β-D-1-ThioGalactopyranoside
KLA	Kdo2-Lipid A
LB	Lysogeny Broth
LN_2	Liquid Nitrogen
LOS	LipoOligoSaccharide
LPR	Lipid-to-Protein-Ratio
LPS	LipoPolySaccharide
MAS	Magic Angle Spinning

MISSISSIPPI	Multiple Intense Solvent Suppression Intended for Sensitive Spectroscopic Investigation of Protonated Proteins
MWCO	Molecular Weight Cut-Off
N. gonorrhoeae	Neisseria gonorrhoeae
NMR	Nuclear Magnetic Resonance
NOE	Nuclear Overhauser Effect
OD_{600}	Optical Density at 600 nm
OMV	Outer Membrane Vesicle
Opa	OPacity-Associated
PDB	Protein Data Bank
REBURP	RE-Band-selective Uniform-Response Pure-phase
REDOR	Rotational-Echo DOuble Resonance
rf	radiofrequency
RFDR	Radiofrequency Driven Dipolar Recoupling
RMSD	Root-Mean-Square Deviation
SARS-CoV2	Severe Acute Respiratory Syndrome-CoronaVirus type 2
SDS-PAGE	Sodium Dodecyl Sulphate PolyAcrylamide Gel Electrophoresis
SEC	Size-Exclusion Chromatography
SH3	Src-Homology 3
STATES-TPPI	States Haberkorn Ruben-Time Proportional Phase Incrementation
SV	SemiVariable
TALOS	Torsion Angle Likelihood Obtained from Shifts and sequence similarity
TEDOR	Transferred-Echo DOuble Resonance
TM	TransMembrane
TPPM	Two-Pulse-Phase-Modulated
TREDOR	Transferred-Rotational-Echo DOuble Resonance
UV-VIS	UltraViolet-VISible
WALTZ-16	Wideband, Alternating-phase, Low-power Technique for residual splitting decoupling
WATERGATE	WATER suppression by GrAdient Tailored Excitation
zf	z-filter
αPET	α Proton Exchange by Transamination

List of figures

List of tables

1. Abstract

Studying the structure of transmembrane (TM) proteins is an important task since many of them are drug targets and are involved in essential cellular functions. However, new techniques are urgently needed, as TM proteins are not amenable to conventional techniques. The recent development of ultrafast magic angle spinning solid-state NMR with proton detection provides a promising avenue. The protein Opa60 is a β-barrel TM protein found in the outer membrane of the human pathogen *Neisseria gonorrhoeae* and mediates adhesion to human host cells via the hCEACAM-family of TM proteins with its large extracellular loops. Its structure has been determined previously in detergent micelles by solution NMR. However, structural insight in a native-like environment is needed to study the binding of Opa60 to its receptor under more physiological conditions and therefore, proton-detected solid-state NMR was chosen in this thesis as a technique to study Opa60 in DMPC lipid bilayers. In this work, the structure of the β-barrel was successfully determined and shows an extension of the length of the β-strands compared to the solution structure. The loops retain their dynamic behavior and are not visible in cross polarization based solid-state NMR experiments. The binding of Opa60 to the N-terminal domain of hCEACAM1 (hCEACAM1-N) could not be shown in lipid bilayers, however solution NMR data indicated a possible interaction in detergent. Opa60 in DMPC was compared with Opa60 in two different LPS species and Kdo2-lipid A, which resemble the native outer membrane environment of *N. gonorrhoeae*, but no major structural changes were apparent from the spectra. In the future, the assignments should be completed and likely reveal the extension of the complete β-barrel to match the thickness of the lipid bilayer. The receptor binding conditions will need to be investigated systematically. Alternatively, a solution NMR assignment of hCEACAM1-N can be conducted and used as a starting point to target the binding surface of Opa60 employing various isotopic labeling schemes.

Method development in solid-state NMR is ongoing and of high importance. Techniques for accurate internuclear distance determination are sought for. In this thesis, a new technique was developed termed TRansferred Rotational DOuble Resonance (TREDOR), based on the TEDOR and REDOR sequences. In TREDOR, both starting and transferred signal are co-acquired and this enables a single parameter fit to the internuclear distance. After calibrating the fitting, the accuracy and ease of TREDOR was demonstrated on the microcrystalline protein SH3. The structure was determined using only TREDOR-derived distances and TALOS-N angle restraints. The superiority of TREDOR over TEDOR was shown in terms of distance

accuracy when compared to a known crystal structure of SH3. Moreover, TREDOR can be applied with only a single mixing time, drastically reducing the necessary measurement time. TREDOR was applied to the TM protein Opa60, and one long-distance contact was found. The technique is mostly limited by strong peak overlap, as seen for Opa60. The application of TREDOR to other challenging systems will likely prove it to be a valuable tool in structural biology.

2. Introduction

2.1. The transmembrane protein Opa60

2.1.1. Transmembrane proteins

Transmembrane (TM) proteins form an important class of proteins.[1] They are defined by their cellular location, spanning across the lipid bilayer membrane of the cell. TM proteins exhibit a large variety of functions. They are, for example, active or passive channels/transporters for ions or metabolites, enzymes, signal receptors and transducers, and are involved in energy generation. Intriguingly, TM proteins also account for around two thirds of all existing drug targets.[2,3] This highlights their importance as a research target, and their structural characterization forms the crucial step in understanding the function of a TM protein.

Structurally, TM proteins can be divided into two types. α-helical TM proteins span the membrane with one or multiple α-helices. The other type is the β-barrel TM protein, where the membrane is transversed by several β-strands in the form of a barrel, which is usually formed by an antiparallel sheet held together by hydrogen bonds. These are found in bacterial outer membranes and mitochondria. The structure of β-barrel TM proteins can be further characterized with the twist and shear of individual strands.[4]

The three major biophysical techniques for structure determination of proteins at atomic resolution are X-ray crystallography,[5] cryo electron microscopy[6,7] and Nuclear Magnetic Resonance (NMR) spectroscopy. In X-ray crystallography, the X-ray diffraction pattern of a protein crystal is the basis for structure determination, and in (single particle) cryo electron microscopy, the high resolution of an electron microscope and the averaging of thousands of individual protein molecules leads to the protein's structure. NMR spectroscopy offers the unique advantage of studying TM proteins in their native lipid environment without the need for crystallizing or freezing the sample, and moreover allows the study of their dynamic features as well.[8,9] Despite the fact that TM proteins account for 20-30% of the human genome and their medical importance,[10] structural data is heavily underrepresented when compared to other proteins. A simple search in the protein data bank (PDB, rcsb.org, 25/03/2021, search terms "membrane protein" and "protein") reveals that only 2.1% of the protein structures contain the term "membrane protein". This is likely a high estimate since the result has not been corrected for uniqueness of proteins. Only 22 solid-state NMR structures of membrane proteins have been

reported (see section 2.2.4). An overview of all determined membrane protein structures can be found online (blanco.biomol.uci.edu/mpstruc, 25/05/2021).

2.1.2. Opa60 and hCEACAM1-N

The TM protein Opa60 belongs to the family of OPacity Associated (Opa) proteins found in the outer membrane of several *Neisseria* bacteria, among which the most prominent are human pathogens *N. gonorrhoeae* and *N. meningitidis*.[11–13] Both species harbor different *opa* genes and their expression is subject to phase variation, which means that their expression can occur independently from the other genes.[14] The large variety of *opa* genes and their phase variation is thought to have evolved as an immune escape mechanism. Opa proteins mediate the adhesion to and uptake into human mucosal host tissues.[15]

Structurally, all Opa proteins are eight-stranded β-barrel TM proteins with four extracellular loops.[13] These feature one semivariable (SV), two hypervariable (HV1 and 2) and one conserved loop. The SV and HV loops are sites exhibiting most differences in between Opa variants. This is particularly pronounced for the HV regions.[13] Both HV regions and their interplay have been shown to be implicated in receptor binding and defining host tropism.[16–18] Intriguingly, most engineered chimeric Opa variants did not retain receptor specificity and in some cases, new heparansulphate proteoglycan (HSPG) binding capabilities were created. For meningococcal Opa variants, a conserved sequence on HV2 has been found and the importance of the presence of a distinct combination of HV1 and 2 was shown.[19]

Opa proteins can be divided into two classes by their receptor tropism. One set binds to the protein family of HSPGs[20,21] and the other set to the carcinoembryonic antigen-related cell adhesion molecule (CEACAM) proteins.[22–26]

Opa60 is found in *N. gonorrhoeae*, which is the causal pathogenic agent of the disease gonorrhea in humans. The structure of the 27.1 kDa protein (PDB: 2MAF) has been determined with solution NMR in detergent micelles.[27,28] In this study, dodecylphosphocholine (DPC) was used and enabled the assignment of 92% of residues within the β-barrel and 27% of residues in the extracellular loops. Because of the high flexibility of the loops a hybrid approach for structural refinement employing molecular dynamics (MD) simulations in 1,2-dimyristoyl-sn-glycero-3-phosphocholine (DMPC) lipid bilayers was used. The loops (SV, HV1 and HV2) were shown to be mobile on the nanosecond timescale with large amplitude motion. In the MD

simulations, short-lived contacts between HV1 and HV2 as well as the occupation of helical conformers for all three loop regions was shown. However, no structural consensus for these regions was reached and a membrane restraint was entered into the simulation to prevent the loops from crossing the membrane barrier. A hypothesized interaction, based on negatively charged residues above the membrane, with lipopolysaccharides (LPS) by a simple titration was not observed. Neisserial outer membranes contain lipooligosaccharides (LOS),[29] which are not commercially available. The structure of Opa60 has not been determined in more native lipid bilayers to date.

At the time of writing, there is only one study of the interaction of Opa60 with the native receptors human CEACAM1 (hCEACAM1) and hCEACAM3 which used a reconstituted protein rather than live bacteria as in former studies.[30] The interaction has been characterized with fluorescence anisotropy and shown to be in the low nanomolar range (K_D 1.6±0.6 nM for hCEACAM1 and 4.3±2.8 nM for hCEACAM3) and hypothesized to be necessary for competition with the native hCEACAM interactions. Recently, a fluorescence activated cell sorting (FACS) assay was developed for the characterization of Opa-CEACAM interactions using live bacteria.[31] The mode of binding and whether or not distinct residues in the HV regions of Opa60 play a role in the interaction is not known.

The CEACAM family of proteins comprise several members. Structurally, they are either TM or membrane-anchored proteins and expose a varying number of immunoglobulin (Ig) domains towards the extracellular side. *In vivo*, the CEACAM proteins are involved in homotypic and heterotypic cell adhesion as well as in TM signaling. They are expressed on epithelial cells and some other cell types, including immune cells[32] and are widely accepted as tumor markers.[33] The non-glycosylated face of the N-terminal Ig domain of the CEACAM proteins has been shown to interact with the Opa proteins and the interaction has been well characterized on a per-residue basis using mutagenesis and chimeric receptor constructs.[17,34] The structure of the N-terminal domain of hCEACAM1 (hCEACAM1-N) has been solved with X-ray crystallography.[35]

The study of Opa60 in lipid bilayers calls for the use of solid-state NMR spectroscopy. In section 2.2, the basic concepts of NMR spectroscopy and their application to TM proteins are introduced.

2.2. NMR spectroscopy

2.2.1. Basics of NMR spectroscopy and HSQC

On nuclear magnetic resonance (NMR) spectroscopy, several excellent introductory textbooks exist.[36–40] These form the basis for this introduction.

Several atomic nuclei possess an intrinsic property termed spin. It is the presence of this property which makes the acquisition of NMR spectra of the respective nucleus possible. The spin behaves as an angular momentum of the particle. It is characterized by a spin quantum number, I, which can take half-integer or integer values. The total angular momentum L of the particle is given as:

$$L = \sqrt{I(I+1)} * \hbar \tag{1}$$

Here, $\hbar$ is the reduced Planck constant ($h/2\pi$). With a given spin quantum number, the nucleus can adopt N_E different energy states:

$$N_E = 2I + 1 \tag{2}$$

Without an external magnetic field, these states are degenerate. When applying a magnetic field B_0, however, the individual states are not degenerate anymore. Their respective energy is given as:

$$E_m = -m\hbar\gamma B_0 \tag{3}$$

m denotes the individual energy states and can take values from -I to +I in integer steps. γ is the gyromagnetic ratio of the nucleus and an intrinsic property of it. In NMR spectroscopy, the transition between the lower and higher energy state is excited with radiofrequency (rf) waves. The transition energy for a spin-½ nucleus with positive gyromagnetic ratio (m=-½ is the low energy state) is given as:

$$\Delta E = E_{high} - E_{low} = \hbar\gamma B_0 \tag{4}$$

The quantity γB_0 has units of frequency (rad/s), and its negative is termed the nuclear Larmor frequency ω_0:

$$\omega_0 = -\gamma B_0 \tag{5}$$

NMR sensitivity, expressed as the signal-to-noise ratio S/N is determined by:

$$\frac{S}{N} \propto \frac{N\gamma_{ex}\gamma_{rec}^{3/2}B_0^{3/2}K}{\sqrt{\Delta f(T_C R_C + T_a[R_C + R_S] + T_S R_S)}} \quad (6)$$

Equation (6) includes a number of factors influencing the NMR sensitivity. N is the number of individual observed nuclei, γ_{ex} and γ_{rec} are the gyromagnetic ratios of the excited and detected nuclei, respectively, B_0 is the external magnetic field, K is a constant which depends on the exact design of the detection coil, Δf is the receiver bandwidth, R_C and R_S are the resistance of the coil itself and the resistance the sample induces in the coil, respectively, and T_C, T_a and T_S are the temperature of the coil, the noise temperature of the preamplifier and the sample temperature, respectively. This equation yields a number of ways to increase sensitivity. First and foremost, the development of higher field magnets led to an increase in sensitivity in the past years. Experiments have been developed to exploit the high gyromagnetic ratio of protons as the detected nucleus, and the development of cryoprobes with cooled electronics led to less noise and thus an increase in the S/N. Moreover, the sample temperature can be lowered.

In biological NMR spectroscopy, isotopes with spin quantum number ½ are commonly employed due to their favorable spectroscopic properties. Protons, or ^{1}H nuclei possess this quantum number and are also the most abundant hydrogen isotope in nature (99.99%). Their omnipresence in proteins, as well as their high gyromagnetic ratio, make them a prime candidate for protein NMR spectroscopy. However, the abundance of protons also has drawbacks, as explained in more detail in section 2.2.4. ^{12}C (natural abundance 98.9%) is not NMR active with I equals 0, and ^{14}N (natural abundance 99.6%) has a low gyromagnetic ratio and I equals 1 (a so-called quadrupolar nucleus), leading to unfavorable spectroscopic properties. Generally, samples are labeled with ^{13}C and ^{15}N, bot having I equals ½.

Simple NMR experiments are best understood using the vector model. Here, the important ground fact is that the application of a magnetic field B_0 leads to a partial alignment of the individual spins in a sample along the magnetic field. For I=½ nuclei, the substate with m=+½ is denoted α, and the one with m=-½ termed β. The low energy state will be populated higher than the high energy state according to a Boltzmann distribution (here given for I=½), where N_{high} is the number of spins in the high energy state and N_{low} in the low energy state:

$$\frac{N_{high}}{N_{low}} = e^{\frac{-\Delta E}{k_B T}} = e^{\frac{-\gamma \hbar B_0}{k_B T}} \tag{7}$$

k_B is the Boltzmann constant and T the temperature. For conventional NMR conditions, this leads to a net magnetization with only about 1 in 10,000 spins aligned in excess. This renders NMR a comparatively insensitive technique.

The net magnetization aligns with the magnetic field, conventionally placed along the z-axis of a coordinate system. In the simplest NMR experiment (pulse acquire, shown in Figure 1A), this magnetization is tilted into the xy-plane by the application of an rf pulse B_1 using an rf coil. This pulse is referred to as a 90° pulse because of the tilt angle. To effectively tilt the magnetization of a given spin species, the frequency of the rf pulse has to match the nucleus' Larmor frequency. This enables the excitation of a different set of spins with different pulses, which is important for multidimensional, heteronuclear NMR experiments. After initial excitation, the net magnetization will start to precess around the magnetic field, and eventually be aligned again in its equilibrium state. This free precession motion is detected via induction using a detection coil (generally the same coil as the excitation coil), and leads to a time dependent, oscillating signal. The motion can be described classically with a set of equations called the Bloch equations, which are given here with the static B_0 field present:

$$\begin{aligned} \frac{d}{dt}M_x(t) &= \gamma\big(M_y(t)B_0\big) - \frac{M_x(t)}{T_2} \\ \frac{d}{dt}M_y(t) &= -\gamma(M_x(t)B_0) - \frac{M_y(t)}{T_2} \\ \frac{d}{dt}M_z(t) &= -\frac{M_z(t) - M_0}{T_1} \end{aligned} \tag{8}$$

M denotes the individual magnetization components, or the equilibrium magnetization along the z-axis, M_0. As can be seen, a decay is imposed with time constants T_1 (along z) and T_2 (along x and y). These describe relaxation, and will be examined further in section 2.2.2. The resulting signal is termed the free induction decay (FID). A frequency dependent spectrum is then obtained by Fourier transformation of the FID, and individual Lorentzian peaks are obtained at the nucleus' Larmor frequency.

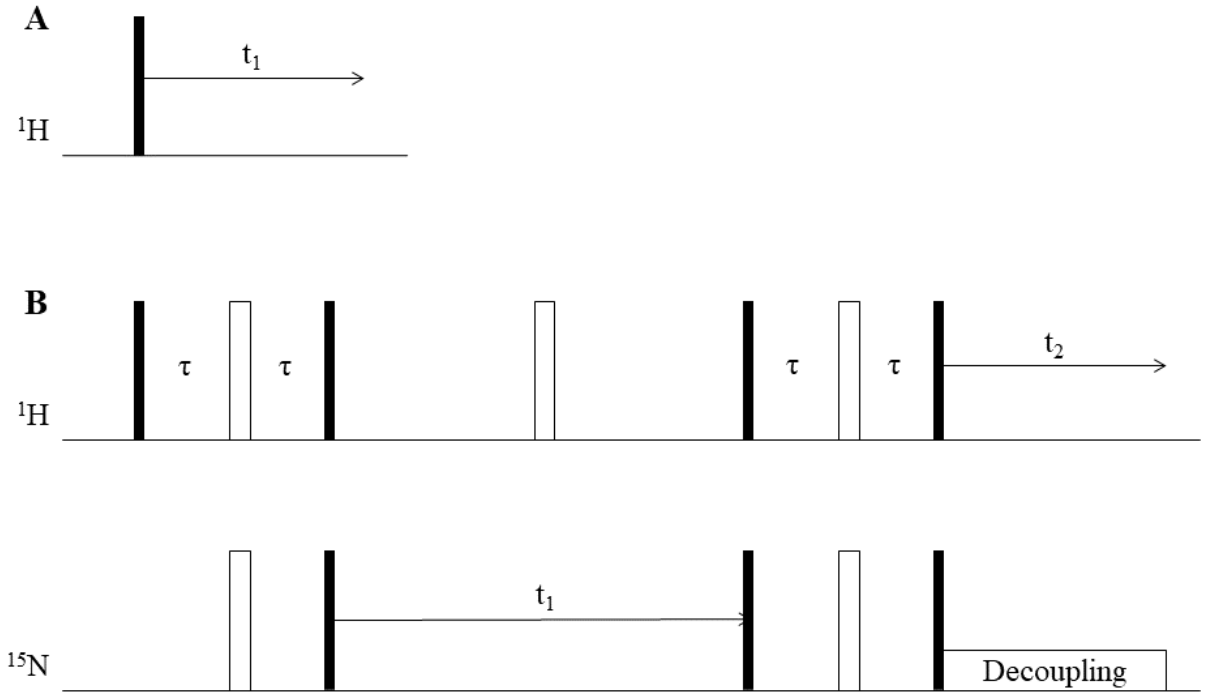

Figure 1: Two basic NMR pulse sequences. **A:** The pulse acquire experiment. **B:** The HSQC experiment. 90° pulses are shown as filled, 180° pulses as empty rectangles. Chemical shift evolution periods are denoted $t_{1/2}$ on the respective channels, and the delay τ depends on the J coupling between the nuclei.

Every nucleus' Larmor frequency not only depends on the externally applied magnetic field B_0, but also on the (much weaker) experienced local magnetic field B_{loc}. The field B_{loc} is mediated by the electron cloud surrounding the nucleus and is a highly sensitive probe for molecular structure. It leads to a modification of the Larmor frequency (after isotropic averaging):

$$\omega_{tot} = \omega_0 + \omega_{loc} = \omega_0 * (1 + \delta) \tag{9}$$

δ is called the chemical shift (CS), and it leads to the appearance of peaks at different frequencies in the spectrum depending on the molecular structure. It is one of the fundamental NMR interactions, and introduced formally in section 2.2.2.

Besides the simple pulse excitation experiment, a multitude of experiments exist. These are generally termed as pulse sequences, and among these, multidimensional NMR experiments are of particular importance for protein NMR spectroscopy. Because of the low chemical shift

dispersion of protons, a simple pulse excitation experiment will not yield site specific information since many signals will overlap. However, the individual peaks can be additionally frequency labeled in correlation experiments with the frequency of, for example, nearby ^{13}C or ^{15}N nuclei. In the following, the very important two dimensional experiment heteronuclear single quantum coherence (HSQC) will serve as an introductory example to multidimensional NMR as well as other concepts important in NMR spectroscopy. In this thesis, the HSQC experiment was used to detect a possible interaction between Opa60 and hCEACAM1-N (section 4.1.2). Its pulse sequence is shown in Figure 1B. Shown here is a ^{15}N-^{1}H-HSQC, as this is an important experiment used to fingerprint proteins spectroscopically.

The HSQC sequence starts out with a 90° pulse on the proton channel. In product operator formalism, which is a versatile tool to analyze pulse sequences, this can be written as:

$$\hat{I}_z \xrightarrow{90°_x(\,^1H)} \hat{I}_{-y} \tag{10}$$

$\hat{I}_z$ and $\hat{I}_{-y}$ are the quantum mechanical operators representing the angular momentum along the specified axis. With the 90° pulse with a phase of x, the z magnetization on any given proton spin I is converted according to the right hand rule into -y magnetization, which represents detectable magnetization. Subsequently, after a delay τ, one 180° pulse on each channel, followed by one 90° pulse on each channel after another delay τ, leads to the emergence of a two-spin coherence between the proton and the nitrogen nucleus:

$$\hat{I}_{-y} \xrightarrow{\tau,\ 180°_x(\,^1H,^{15}N),\ \tau,\ 90°_y(\,^1H),90°_x(^{15}N)} -\sin(2\pi J_{IS}\tau)\hat{I}_z\hat{S}_y + \cos(2\pi J_{IS}\tau)\hat{I}_{-y} \tag{11}$$

In brief, during the period 2τ the J coupling between the proton I spin and a nitrogen S spin evolves, but not the chemical shift due to the refocusing effect of the 180° pulses placed in the middle of the period. The J coupling is a coupling between nuclei mediated via the chemical bonds, and is introduced formally in section 2.2.2. The delay τ is usually chosen according to the one bond J coupling value between the adjacent proton and nitrogen nuclei (for proteins, this is in most cases the backbone amide group):

$$\tau = \frac{1}{4J_{IS}} \tag{12}$$

At the end of the experiment, this will lead to the disappearance of the undesired cosine-term in Equation (11) and the retainment of only the sine-term with the desired coupling. Equation (11) reveals the presence of a an antiphase term $\hat{I}_z\hat{S}_y$, modulated by the J coupling. This term

does not represent detectable magnetization, however, it reveals the transfer of polarization from the high γ proton to a two-spin coherence involving the low γ nitrogen. Besides the established correlation, this also leads to a signal enhancement due to the amplitude of the initial proton polarization being transferred to the nitrogen. The pulse sequence block described so far, followed by a refocusing period to convert the antiphase term to observable in-phase magnetization has been termed insensitive nuclei enhanced by polarization transfer (INEPT). The non-refocused INEPT is the first half of the HSQC experiment. INEPT transfers were used in this thesis to possibly detect mobile sites in Opa60 (Appendix 7.3.5).

In the period t_1, the chemical shift of the nitrogen nucleus is evolved in the indirect dimension. The shift on the protons is again refocused. The repetition of the HSQC experiment with different times t_1 leads to the possibility of extracting the chemical shift of the nitrogen by two dimensional Fourier transformation and is the basis for any multidimensional NMR experiment. After the chemical shift evolution period, the magnetization is:

$$-\cos(\Omega_S t_1)\sin(2\pi J_{IS}\tau)\hat{I}_z\hat{S}_y \tag{13}$$

Ω_S is the chemical shift of the nitrogen nucleus. The antiphase magnetization is then converted back to detectable in-phase magnetization with a second non-refocused INEPT block. After that, the chemical shift of the proton is detected in the direct dimension t_2. On the nitrogen channel, heteronuclear decoupling is employed, which leads to the absence of splitting in the spectrum.

2.2.2. NMR interactions and relaxation

Every NMR spectrum is determined by the interactions between the observed nuclei. Of these, the Zeeman interaction, CS and J coupling have been mentioned in section 2.2.1. In this section, these and other interactions are introduced as a theoretical foundation for this thesis.

The basic equation for any quantum mechanical system is the Schrödinger equation. Its time dependent form describing the evolution of any given system is:

$$\hat{H}|\psi(t)>= i\hbar\frac{d}{dt}|\psi(t)> \tag{14}$$

ψ is the quantum mechanical wave function, describing the state of any given system. The Hamilton operator $\hat{H}$ operates on the wave function, representing the total energy of the system. i is the imaginary unit.

The Hamilton operator (commonly called Hamiltonian) in NMR spectroscopy is used to describe the interactions and the associated energies of these. As a convention, any interaction strength in NMR is given in units of Hertz, and not in Joule, as this relates closely to the frequencies observed in the final spectrum. Physically, this amounts to a factor of the Planck constant h between the two magnitudes. The complete NMR Hamiltonian can be written as:

$$\begin{aligned}\hat{H}_{total} &= \hat{H}_{external} + \hat{H}_{internal} \\ &= \left[\hat{H}_{Zeeman} + \hat{H}_{rf} + \hat{H}_{gradient}\right] \\ &+ \left[\hat{H}_{CS} + \hat{H}_{dipole} + \hat{H}_{J} + \hat{H}_{quadrupole} + \hat{H}_{rotation}\right]\end{aligned} \tag{15}$$

The NMR Hamiltonian consists of an external and an internal part. The first consists of the interaction of the spin with the external field B_0 ($\hat{H}_{Zeeman}$), as well as with the rf pulses ($\hat{H}_{rf}$) and gradient fields ($\hat{H}_{gradient}$). The internal part consists of the CS ($\hat{H}_{CS}$), the dipolar coupling between two spins ($\hat{H}_{dipole}$), the J coupling ($\hat{H}_{J}$), a quadrupolar interaction for spins with I greater than ½ ($\hat{H}_{quadrupole}$), and the small spin-rotation interaction ($\hat{H}_{rotation}$).

Formally, any two-spin interaction has the form:

$$\hat{H} = \vec{I}\,\overleftrightarrow{T}\,\vec{S} \tag{16}$$

I and S are the two vectoral spin quantities in consideration, and T is a second-rank tensor (except for the quadrupolar interaction) describing the interaction. In case of external interactions, S is replaced with the respective magnetic field quantity in Equation (16). With this level of formalism, any interaction can be described also with all of its anisotropic components. In the following, the interactions will be described in a more practical fashion.

Already introduced in section 2.2.1 was the Zeeman interaction, describing the interaction of the spin with the external magnetic field B_0:

$$\hat{H}_Z = -\gamma B_0 \hat{I}_z = \omega_0 \hat{I}_z \tag{17}$$

The Larmor frequency ω_0 appears here as a prefactor to the angular momentum operator $\hat{I}_z$. Together with rf pulses and gradient fields, the Zeeman interaction forms the external interactions. The pulse interactions are not given explicitly in this introduction.

The internal interactions are concerned with interactions in between the individual spins. Described earlier already in section 2.2.1 was the CS interaction, which acts as a modification of the local magnetic field experienced by a spin due to its electronic environment (Equation (9)). The CS is an anisotropic interaction, and the observed shift of a given nucleus depends on the orientation of the CS tensor towards the magnetic field B_0. It can be described by the three principal components of the CS tensor δ_{11}, δ_{22} and δ_{33}. In isotropic liquids, only the isotropic chemical shift is observed due to fast molecular tumbling:

$$\delta_{iso} = \frac{1}{3}(\delta_{11} + \delta_{22} + \delta_{33}) \tag{18}$$

The dipolar interaction is a through-space coupling of two spins, based on the fact that spins also behave as magnetic dipoles. Its magnitude is given by:

$$b_{IS} = -\frac{\mu_0}{4\pi}\frac{\gamma_I \gamma_S \hbar}{r_{IS}^3} \tag{19}$$

μ_0 is the magnetic constant, and r the distance between the nuclei. The full Hamiltonian is (with • being the dot product):

$$\hat{H}_{dipole} = b_{IS}\left(\vec{I} \bullet \vec{S} - 3(\vec{I} \bullet \vec{r})(\vec{S} \bullet \vec{r})\right) \tag{20}$$

Importantly, the dipole coupling depends on the angle Θ of the coupling vector with respect to B_0. This is described with:

$$d_{IS} = b_{IS}(3cos^2(\Theta) - 1) \tag{21}$$

The coupling vanishes at an angle Θ of 54.74°. This is the so-called magic angle and the foundation for magic angle spinning (MAS) solid-state NMR as detailed in section 2.2.3. In

this thesis, dipolar couplings are used to establish the strand arrangement in the structure of Opa60 (section 4.1.1) and to measure internuclear distances (section 4.2).

The J coupling, or scalar coupling, is mediated via the chemical bonds (as opposed to the dipolar coupling) of involved nuclei, and can span one or several chemical bonds. Magnetization can be transferred in INEPT-type experiments through J couplings, and its general, isotropic Hamiltonian can be written as:

$$\hat{H}_{J,iso} = 2\pi \hat{I}\hat{S} \tag{22}$$

The J coupling is a comparatively small quantity when compared to dipolar couplings, but provides useful information about molecular structure and torsion angles. Its anisotropic component is exceedingly small.

The quadrupolar interaction can be large but is of no concern for this thesis, since it only exists for nuclei with a spin quantum number greater than ½. The spin-rotation interaction, which emerges from the rotation of molecules and their nuclei in the magnetic field, can usually be neglected in solid-state NMR.

Besides the described interactions, another important parameter in NMR is relaxation, first introduced in Equation (8). Relaxation describes the return of excited spin states to thermal equilibrium, and can be broken down crudely into two distinct processes.

Longitudinal, spin-lattice relaxation is the return of the magnetization after excitation to the equilibrium state along the field B_0. It is described with the time constant T_1, and the build-up of magnetization along the z-axis follows an exponential equation:

$$M_z(t) = M_{equilibrium} - \left[M_{equilibrium} - M_z(0)\right] e^{-\frac{t}{T_1}} \tag{23}$$

It governs the recycle delay of an NMR experiment, and this delay is usually chosen to be 1.3 - 5 times T_1.

Transverse, spin-spin relaxation describes the decay of magnetization in the xy-plane. It is described by the time constant T_2^*, and importantly, determines the linewidth LW of an NMR signal:

$$LW = \frac{1}{\pi T_2^*} \tag{24}$$

In general, longer T_2 times are a favorable feature of a sample. Two parts contribute to T_2, termed inhomogeneous (T_2') and homogenous (T_2) part. The inhomogeneous contribution can stem, for example, from magnetic field inhomogeneity, and it can be removed using a refocusing pulse (a spin echo sequence). This is not true for the homogenous contribution, which originates from incoherent spin-spin interactions and is an intrinsic sample property.

It is worth mentioning that both types of relaxation also exist in the rotating frame under a spin lock field and are then termed $T_{1\rho}$ and $T_{2\rho}$. The field of relaxation is a large and complex field, and an extensive treatment would go beyond the scope of this thesis.

2.2.3. Solid-state NMR spectroscopy

Fewer dedicated text books exist on solid-state NMR than on general/solution NMR.[41] Levitt's book[37] treats a sound foundation of concepts relevant in any type of NMR experiment. Excellent reviews exist.[42–44]

In opposition to liquid samples, the molecules in solid samples do not experience random molecular tumbling. In liquids isotropic tumbling leads to the effective averaging of dipolar and quadrupolar interactions and only the isotropic chemical shift is observed directly, while the effects of anisotropic interactions are evident in relaxation behavior. Brownian motion is absent in solid samples and as a consequence, the lines are broadened and generally tend to overlap with one another. In principle there is a more structural information in solid-state NMR spectra than in the solution spectra, however the information needs to be extracted from the broad, overlapping lines.

As Equation (21) shows, the dipolar interaction has an angular dependence with respect to the magnetic field. At an angle of 54.74°, the interaction is effectively averaged. Thus, by inclining the sample physically at this "magic angle" with respect to the magnetic field B_0 and spinning it around its own axis, the interaction can be artificially removed. This technique is known as magic angle spinning (MAS) and of crucial importance in modern solid-state protein NMR spectroscopy. It was first introduced in the 1950s.[45,46] In this way, the chemical shift anisotropy and dipolar couplings are removed, leading to the observance of the isotropic chemical shift in

solids as well. Moreover, the quadrupolar interaction is partly averaged out. A complete averaging of this interaction can only be achieved in Double Rotation (DOR) NMR, where the sample is spun at two different angles simultaneously. As a rule of thumb, the spinning has to be faster than the strength of the interaction to be entirely removed because the frequency of spinning has to be high enough such that the spin system does not change its state over one rotor period and thus appears constant. Usually, the quadrupolar interaction is strong and difficult to remove entirely. For dipolar couplings, the interaction strength depends on the gyromagnetic ratio of the nuclei and in case of homonuclear proton-proton couplings, the interaction has a magnitude of around 24 kHz (for vicinal protons in CH_2 groups). The desire to be able to detect protons pushed for the development of faster and faster spinning probes. At the time of writing, ultrafast MAS has conquered the regime of 100 kHz spinning and above,[47] and it is estimated that even faster spinning will be developed.[48] Spinning has been reported up to 150 kHz.[49]

The NMR Hamiltonians introduced in section 2.2.2 are time-dependent in general. Tools to analyze solid-state NMR pulse sequences can be formally analyzed with Average Hamiltonian theory (AHT) or Floquet theory[50] and make use of the concept of the Hamiltonian being constant over a certain period of time.

Removal of the interactions from a spectrum with MAS is different from the averaging observed in solution NMR in that they are coherently removed. They can be reintroduced (recoupled) using a variety of pulse sequences that match the rotor frequency in some way, and these form the basis of many modern solid-state NMR experiments. In this section, the important cross polarization experiment will be introduced. In section 2.2.5, the class of REDOR/TEDOR dipolar recoupling sequences will be introduced in more detail as a means of introducing the TREDOR pulse sequence, which has been developed as part of this thesis.

Cross polarization (CP) is an experiment which is routinely used for magnetization transfer/correlation as well as signal enhancement, analogous to the solution NMR experiment INEPT described in section 2.2.1. In contrast to INEPT, CP is a transfer via the dipolar coupling through space, and not trough bonds via J couplings. J-based transfers are only effective with longer coherence lifetimes, and these can usually only be achieved in solid-state NMR by employing ultrafast MAS above 55 kHz.[51] As mobile fragments tend to have a longer T_2 time, the comparison of INEPT and CP spectra informs about molecular structure.[52,53]

The CP sequence is shown in Figure 2 for a transfer between protons and ^{15}N nuclei. It starts with a 90° pulse on the proton channel to create initial transverse magnetization. Subsequently, spin lock fields are employed simultaneously on both channels. If the nutation frequencies fulfill the Hartmann-Hahn matching condition under MAS, magnetization will be transferred to the ^{15}N nuclei:

$$\omega_1(^1H) - \omega_1(^{15}N) = \gamma_{^1H} B_1(^1H) - \gamma_{^{15}N} B_1(^{15}N) = \pm n * \omega_r \quad (25)$$

ω_1 refers to the nutation frequency, and is related as given to the field strength of the rf pulse B_1. n can take an integer number in theory. Usually, it is 1 or 2 (sideband-matching). n equals 0 results in the conventional Hartmann-Hahn condition without MAS, but this condition will be ineffective the faster the MAS. Ramped CP has been developed and leads to a more robust transfer.[54]

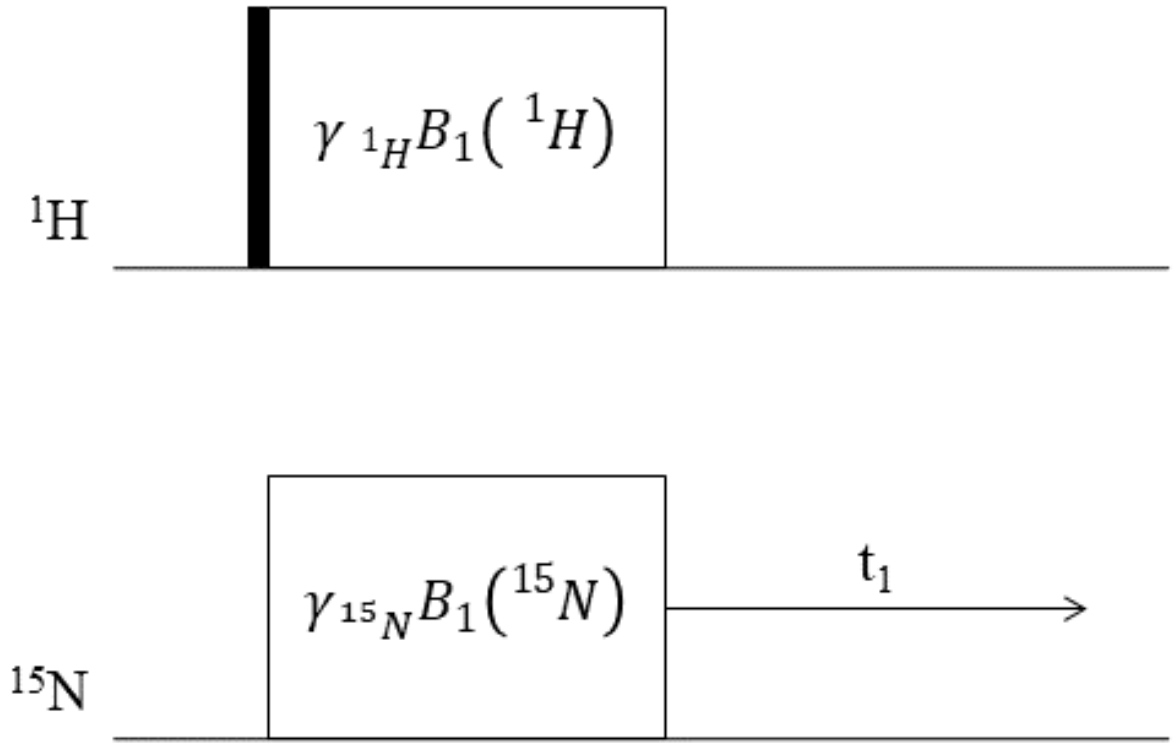

Figure 2: The basic CP element. Magnetization of protons is transferred to the xy-plane through a 90° pulse (black bar) and then via spin locking to the nitrogens, where the signal is then detected during t_1. The power of the spin lock fields has to be chosen to satisfy the Hartmann-Hahn condition.

The CP building block is the fundamental part of most solid-state NMR assignment experiments and is used to transfer magnetization and establish correlations between individual spins.

2.2.4. Solid-state NMR spectroscopy studies of (transmembrane) proteins

Solid-state NMR offers the unique strength of assessing both structure and function of (TM) proteins. The assessment of dynamic features is possible over a wide range of time scales.[55–58]

Solution NMR studies of TM proteins rely on detergent solubilization of the protein, which has been implicated in disturbing the native protein structure.[59,60] In contrast, solid-state NMR can be used to study TM proteins with no principal size limitation reconstituted in lipid bilayers,[8,9] which is closer to the native membrane environment. Studies using extracted native membranes,[61–63] outer membrane vesicles[64] or even in-cell[65] studies of TM proteins are possible and an emerging field.[66] The sample preparation of proteins for solid-state NMR has been extensively described and reviewed.[67] Methods for studying the interaction of TM proteins with the surrounding lipids have been developed.[68]

The first step towards the NMR-based study of any protein is the assignment of resonances of individual atoms within protein residues. The CP experiment described in section 2.2.3 forms the basis for protein assignment sequences in the solid state,[69–74] and can be supplemented with INEPT-type sequences.[51] Typically, the backbone atoms can be assigned in what is usually termed the backbone walk, and subsequently, side chain assignments can be added, including proton assignments.[75,76] In theory, there is no upper limit to protein size in solid-state NMR, however in practice signal overlap poses a difficulty for these studies. The assignment experiments used in this thesis are listed and their parameters are detailed in section 3.2.5 and include backbone Cα/Cβ/CO connectivity as well as amide N-N correlation.

Ideally, the nucleus of detection is proton due to the high gyromagnetic ratio as compared to other nuclei as well as their abundance in proteins and the wealth of structural information that comes with it. The use of fully protonated proteins in solid-state NMR is by far the easiest and cheapest method of sample preparation.[77] The full protonation of side chains enables access to these.[78–80] However, fully protonated proteins have the drawback of inherently lower resolution due to the dense proton network. This makes the development of faster spinning probes necessary to effectively average out proton dipolar couplings.[8,48] Fully protonated Opa60 was used in this thesis (section 4.1.1) to attain structural restraints via Hα.

In order to decrease signal overlap and to enhance spectral resolution in proton detected spectra, a multitude of labeling schemes aimed at proton dilution have been developed. The most straightforward method is to perdeuterate the protein and subsequently reintroduce protons at

exchangeable sites.[81–83] This approach can in principle be applied to TM proteins as well, however in the absence of a refolding protocol, problems can arise due to the inaccessibility of exchangeable protons in the TM part.[84,85] In this thesis, the perdeuterated/back-exchanged Opa60 sample was used for structure determination. Approaches with different levels of deuteration have been developed and can partly compensate the loss in sensitivity.[86,87] More sophisticated are tailored labeling schemes. Reduced adjoining protonation (RAP) uses deuterated glucose in a D_2O-based expression medium with low levels of H_2O (5-15%) present.[88,89] This approach results in an increase in resolution while retaining more sensitivity as compared to perdeuteration. Moreover, it enables access to side chain protons and the important structural information these carry. A similar approach, using protonated glucose in a deuterated medium, results in a higher proton content (up to 40%) and has been termed fractional deuteration (FD).[90] Inverse fractional deuteration (iFD) uses deuterated glucose in protonated medium and has the distinct advantage of enabling expression in H_2O, making the approach suitable for a multitude of expression systems and enabling access to side chain protons.[84] The development of more targeted approaches has led to labeling exclusively methyl groups via metabolic precursors (CH_3 or CHD_2)[91–94], as these are important reporters of protein structure.[95,96] Other approaches include stereo-array isotope labeling[97] (SAIL) where amino acids with an optimized labeling scheme are employed, and proton cloud labeling where protonated amino acids are introduced into an otherwise deuterated background.[98] The specific labeling of protons in the α position via transamination has been developed and termed αPET.[99] Specific amino acid labeling and metabolic scrambling have been thoroughly characterized.[100] The optimal level of deuteration with regard to MAS frequency has been systematically investigated.[101]

As detailed in section 2.1.1, the study of TM proteins with solid-state NMR is still in its infancy. Recent structures of β-barrel TM proteins solved with solid-state NMR include AlkL,[102,103] OmpG[104] and YadA.[62,105] For AlkL, a translocation pathway for hydrophobic substrates was described and the importance of lipids and the membrane composition highlighted. Minor differences in between the solution and solid-state NMR structures were observed for OmpG, and for YadA and the access to dynamic information in the solid state was demonstrated. α-helical TM proteins have also successfully been studied with solid-state NMR. This includes the largest (monomeric) protein whose structure has been determined with solid-state NMR so far, the chemokine receptor CXCR1 with a size of 35.2 kDa.[106] For this study, techniques also from oriented-sample solid-state NMR spectroscopy were employed.[107] Anabaena sensory rhodopsin is a trimer with a monomeric size of 27.5 kDa and is thus the largest system studied

so far considering the oligomeric state.[108,109] The double electron-electron resonance (DEER) technique from the realm of electron paramagnetic resonance (EPR) spectroscopy was employed to generate additional distance restraints.[110] Another example of utmost importance due to the ongoing SARS-CoV2 pandemic at the time of writing is the recent structure determination of the SARS-CoV2 Envelope protein in Endoplasmic-Reticulum-Golgi Intermediate Compartment (ERGIC) membranes, paving the way for the targeted design of inhibitors.[111] The Influenza A M2 protein has been thoroughly studied with solid-state NMR,[112–114] and a functionally important hydrogen bond has been measured via a J coupling between histidine side chains.[115]

2.2.5. REDOR, TEDOR and TREDOR

The foundation for structure determination with solid-state NMR of proteins is the accurate measurement of internuclear distances. Typically, homonuclear restraints are entered as rough distance restraints for structure calculation, obtained from recoupling sequences such as RFDR[116], DARR[117] and DREAM.[118] The need for accurate distance measurements led to the recent development of an RFDR-based technique for solids,[119] analogous to the development of the eNOE technique for solution NMR.[120,121]

For heteronuclear distance measurements, the techniques rotational-echo double resonance (REDOR)[122] and transferred-echo double resonance (TEDOR)[123] have been developed. Both techniques reintroduce the dipolar coupling, averaged by MAS, by a train of rotor-synchronized 180° pulses on a heteronucleus.[124] The recoupled Hamiltonian in TEDOR takes the form of the J-coupling Hamiltonian (Equation (22)) and thus, the experiment works in a similar fashion as HSQC. In REDOR, the dephasing of a signal with increasing mixing time is observed, whereas in TEDOR, the dephasing nucleus and the corresponding signal buildup is observed. The corresponding dipolar oscillation curve can be fitted using a Bessel approximation to extract internuclear distances.[125]

Both REDOR and TEDOR have distinct advantages. For REDOR, it is possible to account for transverse coherence decay by recording a spectrum without dephasing. This is not possible for TEDOR such that the coherence decay and an additional amplitude scaling factor become fitting parameters besides the dipolar coupling strength. The scaling factor can be estimated from strong couplings or a separate experiment.[123,126,127] The major advantage of TEDOR, however, is the direct observation of the dephasing nucleus (to which magnetization is

transferred) and this has been used to extract multiple internuclear distances using z-filters[126] or selective pulses.[128] The technique has been extended for protein assignment, also in combination with other techniques.[129–131]. For exact distance determination, TEDOR data need to be acquired to long mixing times to exactly capture the dipolar oscillation frequency. This is a major drawback of the method when applied to systems with short coherence lifetimes such as TM proteins. In addition, pulse imperfections and the presence of multiple couplings in uniformly labeled systems leads to faster coherence decay.[126,132] This results in more noise and thus unreliable fits with the two additional parameters present.[133]

Ideally, an experiment which incorporates both strengths of REDOR and TEDOR would be needed. Specifically, short mixing times and the recording of both the dephasing and the dephased nucleus would lead to accurate distance determination in complex samples such as TM proteins. Th technique introduced in this thesis has been published as transferred-rotational-echo double resonance (TREDOR)[134] and works by co-acquiring both chemical shifts simultaneously. In this way, also the two additional fit parameters amplitude scaling and coherence decay are removed and what remains is a single parameter fit to the dipolar coupling.

2.3. Aims of this thesis

The structure of Opa60 has to date not been determined in native-like lipid bilayers, as opposed to the detergent structure in DPC. Solid-state NMR holds the unique opportunity of assessing TM proteins like Opa60 both structurally and functionally under these conditions. The first aim is the structure determination of perdeuterated Opa60 in DMPC lipid bilayers in order to see whether this results in the same structure as found in detergent micelles. For this, proton-detected MAS solid-state NMR should be used. This will also add another structure to the sparse set of β-barrel TM proteins whose structure has been determined with solid-state NMR. The behavior of the loops should be described and compared with liquid-state data. Furthermore, the attainment of structurally relevant information on a fully protonated sample via Hα is investigated. Sections 4.1.1 and 5.1.1 are the results and discussion for this part.

The second aim is to investigate the interaction between Opa60 and hCEACAM1-N, ideally on a per-residue basis on Opa60. This should pave the way for future NMR investigations of the

interaction and ultimately to the description of the binding mode of Opa60 to the CEACAM proteins. The results for this part are shown in section 4.1.2, and the discussion in 5.1.2.

As a third aim, the structural behavior of Opa60 in a set of different lipids, resembling the native environment of the *N. gonorrhoeae* bacterial outer membrane with LOS/LPS, is investigated. This is shown in section 4.1.3 and discussed in 5.1.3.

The fourth aim is the characterization of the TREDOR method. This includes an analysis of the pulse sequence (section 3.2.7), the characterization of the fitting (results in section 4.2.1 and discussion in 5.2.1) and coherence decay (results in section 4.2.2 and discussion in 5.2.2) as well as the application of TREDOR to the structure determination of the model protein SH3 (results in section 4.2.3 and discussion in 5.2.3). The application of TREDOR and the possibility of recording long-range contacts for a challenging TM protein such as Opa60 is investigated (results in section 4.2.4 and discussion in 5.2.4).

2.4. TREDOR publication

The parts of this thesis regarding TREDOR (3.2.7.1, 0, 3.2.7.3, 4.2, 5.2, 7.5) have been published (https://pubs.acs.org/doi/10.1021/acs.jpca.0c09033, 10/05/2021).[134] The author of this thesis (Marcel C. Forster) and Xizhou Cecily Zhang contributed equally to all parts except to the simulations, which have been performed by Dr. Evgeny Nimerovsky. Kumar Tekwani Movellan helped with protein assignment. Loren B. Andreas supervised the project.

Any further requests regarding the reuse of material from the article should be directed to ACS Publications.

3. Materials and Methods

3.1. Materials

3.1.1. Media

Table 1 lists media used in this thesis. Derived from the original work,[135] a large variety of modified M9 medium recipes exist (see for example thelabrat.com/protocols/m9minimal.shtml, cshprotocols.cshlp.org/content/2010/8/pdb.rec12296.full or subtiwiki.uni-goettingen.de/wiki/index.php/M9_minimal_medium, all 20/05/2021). In this thesis an in-house version has been used.

Table 1: List of media used in this thesis.

Medium	Component	Concentration/Magnitude
Modified M9 minimal medium (H_2O/D_2O)	Trace Elements	10 ml/l
	Thiamin-HCl	30 mg/l
	Biotin	15 mg/l
	$CaCl_2$	0.1 mM
	$MgSO_4$	2 mM
	D-Glucose ($^{13}C_6$ or	4 g/l (Opa60, hCEACAM1-N)
	$^{13}C_6/d_7$)	3 g/l (SH3)
	$^{15}NH_4Cl$	1 g/l
	5xM9 salts	200 ml/l
	Antibiotics	50 ng/µl (kanamycin), 100 ng/µl (ampicillin)
Trace elements	$FeSO_4$•7 H_2O	21.6 mM
	$MnCl_2$•2 H_2O	5.81 mM
	$CoCl_2$•6 H_2O	3.36 mM
	$ZnSO_4$•7 H_2O	2.43 mM
	$CuCl_2$•4 H_2O	1.76 mM
	H_3BO_3	0.32 mM
	$(NH_4)_6Mo_7O_{24}$•4 H_2O	0.20 mM
	EDTA	17.11 mM
5xM9 salts	Na_2HPO_4	238.80 mM
	KH_2PO_4	110.22 mM
	NaCl	42.78 mM

	pH	7.4

3.1.2. Buffers

Table 2 contains a list of buffers used in this thesis.

Table 2: Lists of buffers used in this thesis.

Buffer	Component	Concentration/Magnitude
Opa60 Lysis	Tris	50 mM
	NaCl	150 mM
	cOmplete, EDTA-free Protease Inhibitor (Roche)	1 per 100 ml
	pH	8.0
Opa60 Solubilization	Tris	50 mM
	NaCl	150 mM
	Gmd-HCl	6M
	pH	8.0
Opa60 TALON Loading	Sodium phosphate	20 mM
	NaCl	150 mM
	Gmd-HCl	6 M
	Imidazole	2 mM
	pH	7.8
Opa60 TALON Washing	Sodium phosphate	20 mM
	NaCl	150 mM
	Gmd-HCl	6 M
	Imidazole	10 mM
	pH	7.8
Opa60 TALON Elution	Sodium phosphate	20 mM
	NaCl	150 mM
	Gmd-HCl	6 M
	Imidazole	250 mM
	pH	7.0
Opa60 Refolding	Tris	20 mM
	NaCl	500 mM
	DPC	0.25% (w/v)
	cOmplete, EDTA-free Protease Inhibitor (Roche)	1 per Refolding approach
	pH	8.0

Opa60 SEC	Sodium phosphate	20 mM
	NaCl	150 mM
	DPC	0.15% (w/v)
	pH	6.2
Opa60 Reconstitution	Sodium phosphate	20 mM
	NaCl	100 mM
	$MgCl_2$	20 mM
	pH	6.2
hCEACAM1-N Lysis	Tris	40 mM
	NaCl	150 mM
	EDTA	2 mM
	Glycerol	10% (v/v)
	DTT	2 mM
	PMSF	1 mM
	pH	8.0
hCEACAM1-N Elution	Tris	40 mM
	NaCl	150 mM
	EDTA	2 mM
	Glycerol	10% (v/v)
	DTT	2 mM
	Glutathione, reduced	20 mM
	pH	8.0
hCEACAM1-N SEC	Sodium phosphate	20 mM
	NaCl	150 mM
	pH	6.2
SH3 Lysis	Tris	25 mM
	pH	8.0
SH3 Elution	Tris	25 mM
	NaCl	1 M
	EDTA	1 mM
	pH	8.0
SH3 SEC	Citric acid	20 mM
	NaCl	200 mM
	EDTA	1 mM
	pH	3.5
SH3 Crystallization	Ammonium sulfate	200 mM
	Sodium azide	0.04% (w/v)

	pH	3.5
SDS-PAGE Stacking Gel	Acrylamide	5.1 % (w/v)
	Tris	125 mM
	SDS	0.1% (w/v)
	Ammonium persulfate	0.1% (w/v)
	TEMED	6.8 mM
	pH	6.8
SDS-PAGE Resolving Gel (15%)	Acrylamide	15% (w/v)
	Tris	375 mM
	SDS	0.1% (w/v)
	Ammonium persulfate (APS)	0.1% (w/v)
	TEMED	2.7 mM
	pH	8.8
4x SDS-PAGE Loading	SDS	3.4% (w/v) SDS
	Tris	150 mM
	Glycerol	46% (v/v)
	Bromphenol blue	1 mg/ml
	β-mercaptoethanol	141 mM
	pH	6.8
10x SDS-PAGE Running	Tris	250 mM
	Glycine	1.920 M
	SDS	1% (w/v)
SDS-PAGE Staining	Coomassie Brilliant Blue G-250	2.7 mM
	Acetic acid	10% (v/v)
	Isopropanol	25% (v/v)
SDS-PAGE Destaining	Acetic acid	10% (v/v)

3.2. Methods

3.2.1. Plasmid design and transformation

3.2.1.1. Opa60 plasmid design

A pET-28b(+) plasmid containing the sequence for expression of Opa60 was ordered from an external vendor (genscript.com, 28/02/2021). An initial DNA sequence was designed by

reverse transcribing the Opa60 sequence[27] with an online tool (bioinformatics.org/sms2/rev_trans.html, 28/02/2021).[136] A C-terminal hexa-histidine tag was attached via insertion of the sequence within restriction sites NcoI and HindIII. The DNA sequence was codon optimized by the vendor for expression in *Escherichia coli*. The complete expressed protein sequence was MASEDGGRGP YVQADLAYAY EHITHDYPEP TAPNKNKIST VSDYFRNIRT RSVHPRVSVG YDFGGWRIAA DYARYRKWNN NKYSVNIENV RIRKENGIRI DRKTENQENG TFHAVSSLGL SAIYDFQIND KFKPYIGARV AYGHVRHSID STKKTIEVTT VPSNAPNGAV TTYNTDPKTQ NDYQSNSIRR VGLGVIAGVG FDITPKLTLD AGYRYHNWGR LENTRFKTHE ASLGVRYRFK LAAALEHHHH HH. The insert DNA sequence is given in Appendix 7.1.1.

3.2.1.2. hCEACAM1-N plasmid design

A pGEX-4T-1 plasmid containing the sequence[35] for expression of the N-terminal domain of human CEACAM1 (hCEACAM1-N) fused via a thrombin cleavage site to an N-terminal GST-tag was ordered from genscript.com. The DNA sequence was codon optimized by the vendor for expression in *Escherichia coli*. Restriction sites BamHI and NotI were used. The hCEACAM1-N sequence after the cleavage of GST was GSGGAQLTTE SMPFNVAEGK EVLLLVHNLP QQLFGYSWYK GERVDGNRQI VGYAIGTQQA TPGPANSGRE TIYPNASLLI QNVTQNDTGF YTLQVIKSDL VNEEATGQFH VY. The insert DNA sequence is given in Appendix 7.1.2.

3.2.1.3. SH3 plasmid and sequence

For the expression of SH3, an in-house pET32a plasmid was used. The sequence of the expressed protein was MDETGKELVL ALYDYQEKSP REVTMKKGDI LTLLNSTNKD WWKVEVNDRQ GFVPAAYVKK LD.

3.2.1.4. Plasmid transformation

The plasmids for expression of Opa60 and hCEACAM1-N were transformed into chemically competent *Escherichia coli* strain BL21(DE3) cells. Cells were thawed on ice and 50-150 ng

of plasmid DNA were added. Cells were kept for 20 minutes on ice, followed by a heat shock for 1 minute at 42°C. Cells were put on ice for 8 minutes, and subsequently LB medium (Sigma-Aldrich) was added to a total volume of 300 µl. Cells were incubated with shaking for 1 hour at 37°C. Afterwards, cells were plated on LB-Agar plates (Sigma-Aldrich) containing the appropriate antibiotic or used directly for protein expression.

3.2.1.5. Glycerol stocks

Glycerol stocks were taken from overnight cultures. Medium with bacteria was mixed 50:50 with 50% sterile filtered glycerol. The mixture was frozen in liquid nitrogen (LN_2) and stored at -80°C.

3.2.2. Protein expression and purification

3.2.2.1. Expression of Opa60

For the expression of perdeuterated Opa60, transformed *E. coli* BL21(DE3), either from LB-Agar plates (Sigma-Aldrich), directly from transformation or from glycerol stocks were grown in LB (kanamycin, Sigma-Aldrich) medium shaking at 37°C overnight. The next morning, cultures were transferred to fresh LB (kanamycin) medium (OD_{600} of 0.05), grown for 3 more hours at 37°C and subsequently the same amount of D_2O was added. Cells were grown for an additional 3.5 hours, washed once in D_2O (via centrifugation, 10 minutes at 5,000 g and 4°C). Cultures were transferred into deuterated M9 medium (kanamycin) for overnight growth shaking at 37°C, and the next day used to inoculate the main deuterated M9 (kanamycin) culture. Cultures were incubated shaking and grown at 37°C until the OD_{600} reached 0.8. Before induction with 1 mM isopropyl β-D-1-thiogalactopyranoside (IPTG), the temperature was decreased to 25°C. Expression was carried out overnight (16 hours) and cells were harvested with centrifugation for 20 minutes at 5,000 g and 4°C. Cell pellets were either used directly for purification or stored at -80°C after freezing in liquid nitrogen (LN_2). Protein expression was assessed with SDS-PAGE.

For the growth of protonated Opa60, cells were grown as day cultures in LB medium (Sigma-Aldrich), transferred to M9 medium overnight and used to inoculate the main M9 culture the next day. Expression temperature was 20°C.

3.2.2.2. Purification of Opa60

The purification protocol was adapted and modified from a previously published work.[27] The cell pellet was resuspended in 35 ml of Opa60 Lysis buffer and bacteria were lysed by sonication on ice (BANDELIN SONOPULS HD2200, 6 × 60% power for 20 seconds, 1 minute pause). The lysate was centrifuged for 1 hour at 22,000 g and 4°C. The pellet was resuspended in 30 ml of Opa60 Lysis buffer with 1% (w/v) Triton X-100. The suspension was centrifuged for 1 hour at 22,000 g and 4°C and the pellet resuspended in 30 ml Opa60 Lysis buffer. After centrifugation for 1 hour at 22,000 g and 4°C, the pellet was solubilized in 30 ml Opa60 Solubilization buffer (with 6M Gmd-HCl). The solution was centrifuged for 45 minutes at 25,000 g and 22°C. The supernatant with additional 2 mM imidazole was loaded onto a 5 ml gravity-flow TALON (Takara Bio) column at room temperature, equilibrated in Opa60 TALON Loading buffer. After binding by passing the solution 2 times, the column was washed with 3 column volumes (CV) of Opa60 TALON Washing buffer. Inclusion body preparation and TALON purification were tracked with SDS-PAGE. Opa60 was eluted with 4 CV of Opa60 TALON Elution buffer and collected in 5 ml fractions. Individual fractions were concentrated (10,000 molecular weight cut-off (MWCO) in a centrifugal concentrator, 3,000-5,000 g, 4°C) to 2.5-5 mg/ml and refolded by 40-fold dilution into Opa60 Refolding buffer, stirring at room temperature for 2.5 days. Refolding success was assessed with SDS-PAGE.[137] The solution containing the refolded protein was concentrated (10,000 MWCO in a centrifugal concentrator, 3,000-5,000 g, 4°C) and purified by gel filtration. 900 µl were loaded into a 1 ml loop and passed over a Superdex 200 Increase 10/300 GL column (GE Healthcare) with Opa60 SEC buffer at room temperature with a flowrate of 0.75 ml/min. 1 ml fractions were collected and assessed with SDS-PAGE. Fractions containing Opa60 were pooled and used for NMR sample preparation. Concentration was determined using UV-VIS spectroscopy (absorbance at 280 nm) using an extinction coefficient ε of 41,870 M^{-1} cm^{-1}, determined with an online tool (web.expasy.org/protparam, 28/02/2021)[138] SDS-PAGE gels documenting the purification are shown in Appendix 7.2.1.

3.2.2.3. Expression of hCEACAM1-N

Transformed *E. coli* BL21(DE3) cells were used to inoculate an LB (Ampicillin, Sigma-Aldrich) day culture, either from plates, directly from a transformation or from glycerol stocks. Cells were transferred into M9 (ampicillin) medium overnight shaking at 37°C, and used

to inoculate the main M9 (ampicillin) culture the next day. Bacteria were grown shaking at 37°C until the OD_{600} reached 0.6-0.7, and before induction with 0.5 mM IPTG, temperature was decreased to 25°C. Expression was conducted overnight (16 hours) and cells were harvested for 20 minutes at 5,000 g and 4°C. Cell pellets were used directly for purification or frozen in LN_2 and stored at -80°C for purification at a later time. Expression was monitored with SDS-PAGE.

3.2.2.4. Purification of hCEACAM1-N

The purification protocol for hCEACAM1-N is based on a previously published protocol[35] and was modified where needed. The cell pellet was resuspended in 35 ml hCEACAM1-N Lysis buffer and cells were lysed using sonication (BANDELIN SONOPULS HD2200, 3 × 20% power for 20 seconds, 1 minute pause, on ice) and passage through Emulsiflex-C3 (Avestin) at 1,000 psi. The lysate was centrifuged for 15 minutes at 7,000 g and 4°C and subsequently the supernatant was centrifuged for 30 minutes at 22,000 g and 4°C. Lysis was controlled using SDS-PAGE. The supernatant was loaded onto a 5 ml GS-Trap HP column (Sigma-Aldrich), equilibrated in hCEACAM1-N Lysis buffer with 0.5 ml/min. After washing with the same buffer at 1-1.5 ml/min, protein was eluted with hCEACAM1-N Elution buffer at 1 ml/min. 2 ml fractions were collected and assessed with SDS-PAGE. Fractions containing GST-hCEACAM1-N were pooled, and thrombin (Sigma-Aldrich) was added (10U/mg of total protein, determined with UV-VIS absorbance at 280 nm, ε of 57,300 M^{-1} cm^{-1} with reduced cysteines, web.expasy.org/protparam, 28/02/2021)[138] for protein cleavage for 2.5 days at room temperature. Successful digestion was monitored with SDS-PAGE and when nearing completion, precipitation occurred. hCEACAM1-N was concentrated (3,000 MWCO in a centrifugal concentrator, 3,000-5,000 g, 4°C) and purified using gel filtration on a Superdex 75 10/300 GL column (GE Healthcare) in hCEACAM1-N SEC buffer with a flowrate of 0.7 ml/min and a loading volume of 900 µl at room temperature. 1 ml fractions were collected and assessed with SDS-PAGE. hCEACAM1-N containing fractions were pooled and protein concentration was determined using UV-VIS absorbance at 280 nm (ε of 14,440 M^{-1} cm^{-1}, web.expasy.org/protparam, 28/02/2021).[138] The protein solution was concentrated (3,000 MWCO in a centrifugal concentrator, 3,000-5,000 g, 4°C). In Appendix 7.2.2, SDS-PAGE gels documenting the purification process are shown.

3.2.2.5. Expression of SH3

Perdeuterated SH3 was produced from BL21(DE3) cells. Bacteria were adapted to D_2O as described for the purification of Opa60 in 3.2.2.1. Cells were grown shaking at 37°C, and before induction at an OD_{600} of 0.8 with 1 mM IPTG, the temperature was switched to 30°C. After overnight (16 hours) expression, cells were harvested as described in 3.2.2.1.

3.2.2.6. Purification of SH3

The purification protocol of SH3 is well established and based on previous publications.[139,140] The cell pellet was resuspended in SH3 Lysis buffer and lysed using sonication (BANDELIN SONOPULS HD2200, 3 × 30% power for 20 seconds, 1 minute pause, on ice) and Emulsiflex-C3 (Avestin) at 1,000 psi. The lysate was centrifuged twice (15 minutes at 7,000 g and 4°C and 30 minutes at 20,000 g and 4°C). Cell lysis was monitored with SDS-PAGE. The supernatant was loaded onto a 5 ml HiTrap Q XL (Sigma-Aldrich) column, equilibrated in the same buffer, at 0.5 ml/min. The column was washed at 1-1.5 ml/min, and elution was conducted with a linear gradient from 0-100% of SH3 Elution buffer over 20 CV. 1.5 ml fractions were collected and assessed with SDS-PAGE. SH3 containing fractions were pooled, concentrated with an $(NH4)_2SO_4$ precipitation (75% saturation, stirring at 4°C) and dialyzed (3,000 MWCO in a dialysis tube, 4°C) overnight against SH3 SEC buffer. SH3 was purified using gel filtration (Superdex 75 10/300 GL (GE Healthcare), in SH3 SEC buffer, room temperature, flow rate 0.75 ml/min). SH3 containing fractions were identified with SDS-PAGE, pooled, and extensively dialyzed against H_2O-HCl (pH 3.5, multiple times 5 l, 3,000 MWCO). Afterwards, the protein concentration was determined with UV-VIS absorption at 280 nm (ε of 15,470 M^{-1} cm^{-1}) and the protein solution was lyophilized and used for crystallization. In Appendix 7.2.3, SDS-PAGE gels documenting the purification process are shown.

3.2.3. Biochemical methods

3.2.3.1. SDS-PAGE

Sodium dodecyl sulphate polyacrylamide gel electrophoresis (SDS-PAGE) is a well-established method for separating proteins by their size. From its first description[141] it has matured into one of the most used techniques.[142] The protocol and buffers used in this

thesis have been adapted from in-house protocols. Protein samples to be analyzed were taken up in SDS-PAGE Loading buffer and boiled for 5 minutes at 95°C. Samples containing refolded Opa60 were not boiled to maintain the correct folding and separation behavior on the gel, as only refolded Opa60 appeared at the correct size.[137] Gels were cast (SDS-PAGE Stacking and Resolving Gel buffers) between 0.75 mm glass plates. APS and TEMED were added last to initiate polymerization. Combs with 15 wells were used. 5 µl of BenchMark™ Protein Ladder (Invitrogen) marker and 5-10 µl of sample were loaded into the wells. Gels were run in 1x SDS-PAGE Running buffer at constant voltage starting at 100 V. Voltage was increased after 10-15 minutes to 130-180 V. Gels were stained in SDS-PAGE Staining buffer by heating for 30 seconds in the microwave and incubating them for 5 minutes. Destaining was conducted in SDS-PAGE Destaining buffer by heating for 30 seconds in the microwave and gently shaking until destaining was complete.

SDS-PAGE samples of bacterial cultures were always adjusted to an OD_{600} of 0.4 before mixing with SDS-PAGE Loading buffer.

3.2.3.2. Interaction between Opa60 and hCEACAM1-N – solution

HSQC spectra of ^{15}N-hCEACAM1-N were recorded on a 800 MHz spectrometer as described in section 3.2.5. First, it was verified that the hCEACAM1-N did not unfold or exhibit major structural rearrangements in 0.15% DPC by recording spectra before and after addition of the detergent in hCEACAM1-N SEC buffer. 10% D_2O was added into the buffer. The spectrum of hCEACAM1-N alone was recorded at a concentration of 49 µM. Unlabeled Opa60 was added in Opa60 SEC buffer such that both proteins were present in equimolar ratios of 32 µM and an HSQC spectrum was recorded. Spectra were processed in Bruker TopSpin 3.5.7/4.0.8 and analyzed with Sparky.[143]

3.2.3.3. Interaction between Opa60 and hCEACAM1-N – solids

For the interaction of hCEACAM1-N and Opa60 in liposomes, Opa60 was reconstituted into a lipid mixture of DMPC, DMPG, cholesterol and DMPE-PEG1000 as described in section 3.2.4.1. A lipid control was prepared in the same way without protein. Protein and control were sonicated (BANDELIN SONOPULS HD3100, 20 minutes, 30 seconds on/off, 20% amplitude).

hCEACAM1(N) was added in threefold molar excess and samples incubated at 25°C for 30 minutes. Samples were centrifuged for 10 minutes at 10,000g and 25°C. The supernatant was taken out and the pellet resuspended in the same volume Opa60 Reconstitution buffer. Samples were analyzed with SDS-PAGE.

3.2.4. NMR sample preparation

3.2.4.1. Reconstitution of Opa60

Purified ^{2}H-^{13}C-^{15}N-Opa60 was reconstituted into lipid bilayers consisting of 1,2-dimyristoyl-sn-glycero-3-phosphocholine (DMPC, Avanti Polar Lipids) with a mass lipid-to-protein-ratio (LPR) of 0.25, corresponding to a molar ratio of 10.25. A dialysis method with the addition of methyl-β-cyclodextrin was used.[144,145] Opa60 was incubated together with detergent-solubilized lipid in a dialysis cassette (3,500 MWCO), and dialysis against Opa60 Reconstitution buffer was conducted for several days with daily buffer switching (500 ml each) and addition of cyclodextrin until precipitation was observed. After a dialysis step without cyclodextrin, 0.02% (w/v) sodium azide was added to the final sample. The reconstituted protein was packed into a 1.3 mm MAS-NMR rotor (Bruker) using centrifugation.[146]

For samples of perdeuterated Opa60 in Kdo2-lipid A (KLA, Sigma-Aldrich),[147] Rd2 LPS from *E. coli* strain F583 (Sigma-Aldrich)[147] and LPS from *E. coli* strain K235 (Sigma-Aldrich) the LPR was adjusted such that the number of acyl chains relative to DMPC (two chains) with the given LPR of 10.25 (molar ratio) was retained. For all three substances, the number of acyl chains was six and required thus a reduction in molar ratio by a factor of three.

Protonated ^{13}C-^{15}N-Opa60 was reconstituted into deuterated DMPC (d54-DMPC, Avanti Polar Lipids) and packed into a 0.7 mm MAS-NMR rotor (Bruker) using centrifugation.[146]

For the Opa60-hCEACAM1-N interaction experiments in solids (section 3.2.3.3), the lipid composition was derived from a previous publication.[30] Stocks of 1,2-dimyristoyl-sn-glycero-3-phosphocholine (DMPC, Avanti Polar Lipids), 1,2-dimyristoyl-sn-glycero-3-phospho-(1'-rac-glycerol, DMPG, Avanti Polar Lipids), cholesterol (Avanti Polar Lipids) and 1,2-distearoyl-sn-glycero-3-phosphoethanolamine-N-[methoxy(polyethylene glycol)-1000] (DMPE-PEG1000, Avanti Polar Lipids) were prepared in chloroform and mixed according to the molar ratio 63% DMPC, 16% DMPG, 16% cholesterol and 5% DMPE-PEG1000 as

previously published. Chloroform was evaporated with nitrogen gas and lipid films were lyophilized. Subsequently, they were resuspended in Opa60 SEC buffer and used for reconstitution as described above.

3.2.4.2. Crystallization of SH3

Purified SH3 was crystallized as previously described.[139,140] Lyophilized SH3 was resuspended at a concentration of 20 mg/ml in H_2O-HCl at pH 3.5, and the same volume of SH3 Crystallization Buffer was added. The pH was shifted to 7.0 with gaseous NH_4. After crystallization, the crystals were kept for 3 days at 4°C and packed into a 1.3 mm MAS-NMR rotor (Bruker).[146]

3.2.5. NMR spectroscopy

Spectrometers and probes used in this thesis were:

- Bruker 600 UltraShield spectrometer, 14.1 T field strength, Bruker MASDVT600W2 BL1.3 HXY probe
- Bruker 800US2 spectrometer, 18.8 T field strength, Bruker MASDVT800S6 BL1.3 C/N/H probed
- Bruker 950US2 spectrometer, 22.3 T field strength, Bruker MASDVT950S6 BL0.7 N/D/C/H probe
- Bruker ASCEND 1.2 GHz spectrometer, 28.2 T field strength, MASDVT1200S6 BL0.7 NCH probe
- Bruker 800 Ultrastabilized spectrometer, 14.1 T field strength, CP TCI 800S7 H-C/N-D-03 Z cryo probe (solution NMR)

In all names of NMR experiments, capital letters indicate the evolution of the chemical shift on the respective nucleus, whereas small letters indicate the magnetization transfer pathway.

Assignment spectra of Opa60 were acquired on a perdeuterated sample on 800 and 600 MHz spectrometers. Chemical shifts were referenced to sodium 2,2-dimethyl-2-silapentane-5-sulfonate (DSS).[148] MAS frequency was 55 kHz and the set temperature 240 K, with a resulting sample temperature of 298 K as determined using water chemical shift at the 800 MHz

spectrometer.[38,146] The recording parameters of assignment spectra acquired at 800 and 600 MHz are given in Table 3. For all spectra, heteronuclear decoupling schemes used were TPPM[149] with 10 kHz on ^{1}H and WALTZ-16[150] with 10 kHz on heteronuclei. In all spectra, MISSISSIPPI water suppression[151] was applied for 100 or 150 ms (latter time for CB spectra) with a strength of 13.75 kHz (corresponding to one quarter of the MAS frequency).

Spectra of perdeuterated Opa60 in different lipids (KLA, Rd2 and K235 LPS), as well as FROSTY-NMR spectra, were recorded with similar parameters as given for hCANH in Table 3.

Recording conditions for spectra of protonated Opa60 recorded at 950 MHz are shown in Table 4. MAS rate was 100 kHz and set temperature 265 K. TPPM and WALTZ-16 heteronuclear decoupling were used with 10 kHz. MISSISSIPPI water suppression was employed for 150 or 200 ms (latter time for hCOCAHA spectrum).

The conditions for TREDOR spectra are shown in Table 5. REDOR pulses were always applied on ^{13}C and cycled with the XY-8 scheme.[152] The spectral region of interest was selected with a selective REBURP[153] pulse. Bandwidths of this pulse were 40-70 ppm for N-Cα, 5-53 ppm for N-Cx and 154-254 ppm for H-CO TREDOR. The N-Cα spectrum for distance calibration using Gly51 was recorded with similar parameters as N-Cx TREDOR, and the selective pulse had a bandwidth from 35 to 75 ppm. Mixing times were 0.14, 1.4, 2.9, 4.3, 5.8, 7.2, 8.6 and 10.1 ms.

The parameters for recording of liquid-state ^{15}N-HSQC spectra of hCEACAM1-N without and with Opa60, as well as the parameters for solid-state hNH spectra (CP- and J-transfer) are given in Table 6.

Where necessary, spectra were corrected for linear field drift.[154] All spectra were acquired with STATES-TPPI for frequency discrimination.[155] Spectra were processed with Bruker TopSpin.3.5.7/4.0.8. The apodization function used for all spectra was QSINE with a sine bell shift of 2. Acquisition time in the direct dimension was appropriately cut to maximize signal-to-noise ratio, and zero filling was employed.[156]

Table 3: Recording parameters of assignment spectra acquired at 600 and 800 MHz. In all spectra, MAS frequency was 55 kHz and the set temperature 240 K.

Experiment	**hCANH**	**hcoCAcoNH**	**hCONH**	**hcaCBcaNH**	**hcaCBcacoNH**	**hCOcaNH**	**hNcacoNH**	**HNhhNH**
Number of scans	24	72	12	96	164	64	88	2
Recycle delay [s]	0.6	0.7	0.7	0.6	0.6	0.7	0.7	0.8
Total measurement time [h]	77	121	45	105	806	119	101	190
Hard pulse power [kHz]								
^{1}H	102	102	102	100	100	102	102	100
^{13}C	63	63	63	68	68	63	63	63
^{15}N	78	78	78	50	50	78	78	78
Carrier frequency [ppm]								
^{1}H	4.7	4.7	4.7	4.7	4.7	4.7	4.7	4.7
^{13}C	53.7	53.7	173.7	40	40	173.7	173.3	53.7
^{15}N	118.5	118.5	118.5	118.5	118.5	118.5	118.5	118.0
Spectral width [ppm]								
^{1}H	30	30	30	41.7	41.7	30	30	30.1 (direct), 12 (indirect)
^{13}C	30	30	20	80	80	20	-	-
^{15}N	32	32	32	35	35	32	36	32
Acquisition time [ms]								
^{1}H	21.3	21.3	21.3	20.5	20.5	21.3	21.3	21.2 (direct), 4.9 (indirect)
^{13}C	8.1	7.1	16.4	7.1	7.1	10.7	-	-
^{15}N	15.0	14.7	21.6	15.1	15.1	14.7	15.1	11.6
Transfer 1								
Type	^{1}H-^{13}C CP	^{1}H-^{13}C CP	^{1}H-^{13}C CP	^{1}H-^{13}C CP	^{1}H-^{13}C CP	^{1}H-^{13}C CP	^{1}H-^{15}N CP	^{1}H-^{15}N CP
Average power [kHz]	95 (^{1}H), 51 (^{13}C),	95 (^{1}H), 38 (^{13}C)	95 (^{1}H), 38 (^{13}C)	98 (^{1}H), 38 (^{13}C)	95 (^{1}H), 38 (^{13}C)	95 (^{1}H), 38 (^{13}C),	95 (^{1}H), 38 (^{15}N)	94 (^{1}H), 38 (^{15}N)
Time [ms]	5.5	5	5	4.5	4.5	5	0.8	0.7
Shape	Ramp80-100% (^{1}H)	Ramp80-100% (^{1}H)	Ramp80-100% (^{1}H)	Ramp80-100% (^{1}H)	Ramp80-100% (^{1}H)	Ramp80-100% (^{1}H)	Ramp80-100% (^{1}H)	Ramp80-100% (^{1}H)
Transfer 2								
Type	^{13}C-^{15}N CP	^{13}C-^{13}C INEPT	^{13}C-^{15}N CP	^{13}C-^{13}C INEPT	^{13}C-^{13}C INEPT	^{13}C-^{13}C INEPT	^{15}N-^{13}C CP	^{15}N-^{1}H CP
Average power [kHz]	15 (^{13}C), 39 (^{15}N)	-	15 (^{13}C), 39 (^{15}N)	-	-	-	39 (^{15}N), 15 (^{13}C)	38 (^{15}N), 88 (^{1}H)
Time [ms]	10	3.5	10	4.7	4.7	3.5 (first step), 2.5	10	0.5

						(second step)		
Shape	Ramp100 -80% (^{15}N)	-	Ramp100 -80% (^{15}N)	-	-	-	Ramp100-80% (^{15}N)	Ramp100 -80% (^{1}H)
Transfer 3								
Type	^{15}N-^{1}H CP	^{13}C-^{15}N CP	^{15}N-^{1}H CP	^{13}C-^{15}N CP	^{13}C-^{13}C INEPT	^{13}C-^{15}N CP	^{13}C-^{13}C INEPT	^{1}H-^{1}H RFDR
Average power [kHz]	35 (^{15}N), 90 (^{1}H)	15 (^{13}C), 39 (^{15}N)	38 (^{15}N), 90 (^{1}H)	79 (^{13}C), 25 (^{15}N)	-	15 (^{13}C), 39 (^{15}N)	-	100
Time [ms]	0.6	10	0.6	11.5	4.5 (first step), 3.8 (second step)	10	3.5 (first step), 2.8 (second step)	1.7
Shape	Ramp100 -80% (^{1}H)	Ramp100-80% (^{15}N)	Ramp100 -80% (^{1}H)	Ramp100-80% (^{15}N)	-	Ramp100-80% (^{15}N)	-	-
Transfer 4								
Type		^{15}N-^{1}H CP		^{15}N-^{1}H CP	^{13}C-^{15}N CP	^{15}N-^{1}H CP	^{13}C-^{15}N CP	
Average power [kHz]		35 (^{15}N), 90 (^{1}H)		45 (^{15}N), 105 (^{1}H)	31 (^{13}C), 25 (^{15}N)	38 (^{15}N), 90 (^{1}H)	66 (^{13}C), 39 (^{15}N)	
Time [ms]		0.6		0.5	10	0.6	10	
Shape		Ramp100-80% (^{1}H)		Ramp100-80% (^{1}H)	Ramp100-80% (^{15}N)	Ramp100-80% (^{1}H)	Ramp100-80% (^{15}N)	
Transfer 5								
Type					^{15}N-^{1}H CP		^{15}N-^{1}H CP	
Average power [kHz]					45 (^{15}N), 104 (^{1}H)		38 (^{15}N), 90 (^{1}H)	
Time [ms]					0.5		0.6	
Shape					Ramp100-80% (^{1}H)		Ramp100-80% (^{1}H)	

Table 4: Recording parameters of spectra acquired at 950 MHz. In all spectra, MAS frequency was 100 kHz and the set temperature 265 K.

Experiment	**hNCAHA**	**hCOCAHA**	**hCCH**	**hXhhXH**[157]
Number of scans	16	16	4	8
Recycle delay [s]	0.8	0.8	0.8	0.8
Total measurement time [h]	57	20	56	420
Hard pulse power [kHz]				
^{1}H	156	156	156	156
^{13}C	80	80	80	78
^{15N}	35	35	35	35
Carrier frequency [ppm]				
^{1}H	4.7	4.7	4.85	4.85
^{13}C	53.7	173.3	65	75
^{15}N	118.5	118.5	118.5	118.5
Spectral width [ppm]				
^{1}H	52.6	52.6	29.9	29.9

^{13}C	30	30 (Cα), 15 (CO)	130	268.2 (F2, medium dimension before transfer)
^{15}N	30	-	-	139.5 (F1, slowest dimension after transfer)
Acquisition time [ms]				
^{1}H	41.0	20.5	36.0	36.0
^{13}C	6.1	6.0 (Cα), 13.9 (CO)	5.1	4.8 (^{13}C, F2), 11.9 (^{15}N, F2)
^{15}N	14.2	-	-	4.3 (^{13}C, F1), 10.7 (^{15}N, F1)
Transfer 1				
Type	^{1}H-^{15}N CP	^{1}H-^{13}C CP	^{1}H-^{13}C CP	^{1}H-^{15}N/^{13}C CP
Average power [kHz]	129 (^{1}H), 29 (^{15}N)	113 (^{1}H), 21 (^{13}C)	125 (^{1}H), 30 (^{13}C)	127 (^{1}H), 30 (^{15}N) ,28 (^{13}C)
Time [ms]	0.5	2.5	1.2	1 (^{1}H/^{15}N), 0.8 (^{13}C)
Shape	Ramp80-100% (^{1}H)	Ramp100-85% (^{1}H)	Ramp80-100% (^{1}H)	Ramp80-100% (^{1}H)
Transfer 2				
Type	^{15}N-^{13}C CP	^{13}C-^{13}C INEPT	^{13}C-^{13}C RFDR	^{15}N/^{13}C-^{1}H CP
Average power [kHz]	38 (^{15}N), 62 (^{13}C)	-	80	30 (^{15}N) ,35 (^{13}C), 126 (^{1}H)
Time [ms]	9.5	3.5 (first step),2.5 (second step)	1.6	0.4 (^{1}H/^{15}N), 0.25 (^{13}C)
Shape	Ramp90-1000% (^{15}N)	-	-	Ramp100-85% (^{1}H)
Transfer 3				
Type	^{13}C-^{1}H CP	^{13}C-^{1}H CP	^{13}C-^{1}H CP	^{1}H-^{1}H RFDR
Average power [kHz]	30 (^{13}C), 120 (^{1}H)	29 (^{13}C), 119 (^{1}H)	32 (^{13}C), 123 (^{1}H)	156
Time [ms]	0.3	0.2	0.35	0.48
Shape	Ramp100-80% (^{1}H)	Ramp100-85% (^{1}H)	Ramp100-85% (^{1}H)	-
Transfer 4				
Type				^{1}H-^{15}N/^{13}C CP
Average power [kHz]				127 (^{1}H), 30 (^{15}N) ,28 (^{13}C)
Time [ms]				1 (^{1}H/^{15}N), 0.8 (^{13}C)
Shape				Ramp80-100% (^{1}H)
Transfer 5				
Type				^{15}N/^{13}C-^{1}H CP
Average power [kHz]				30 (^{15}N) ,35 (^{13}C), 126 (^{1}H)
Time [ms]				0.4 (^{1}H/^{15}N), 0.25 (^{13}C)
Shape				Ramp100-85% (^{1}H)

Table 5: Recording parameters of TREDOR spectra acquired at 600 MHz and 1.2 GHz.

Experiment	**N-Cx (hn(C/N)NH**	**H-CO (hN(H/C)H)**	**H-CO (Opa60)**
Field [MHz]	600	600	1,200
Number of scans	4 (per mixing time)	4 (per mixing time)	4 (per mixing time)
Recycle delay [s]	1	1.5	0.9
Total measurement time [h]	48 (per mixing time)	44 (per mixing time)	31 (per mixing time)
Set temperature [K]	240	240	265

MAS frequency [kHz]	55.555	55.555	100
Hard pulse power [kHz]			
^{1}H	100	100	147
^{13}C	100	100	114
^{15}N	83	83	78
Carrier frequency [ppm]			
^{1}H	4.5	4.5	4.72
^{13}C	40 (combined dimension)	203.7 (combined dimension)	203.7 (combined dimension)
^{15}N	90	118	120
Spectral width [ppm]			
^{1}H	41.7	41.7	40.4
^{13}C	130.7 (combined dimension)	184.4 (combined dimension)	331.3
^{15}N	30	30	30
Acquisition time [ms]			
^{1}H	20.5	20.5	21
^{13}C	8 (^{13}C), 19.9 (^{15}N)	7.2 (^{13}C and ^{1}H)	3 (^{13}C and ^{1}H)
^{15}N	16.5	16.5	6.3
Decoupling 1			
Scheme	TPPM[149] (^{1}H)	TPPM[149] (^{1}H)	TPPM[149] (^{1}H)
Power [kHz]	12	12	23
Decoupling 2			
Scheme	WALTZ-16[150] (heteronuclei)	WALTZ-16[150] (heteronuclei)	WALTZ-16[150] (heteronuclei)
Power [kHz]	10	10	10
Water suppression			
Scheme	MISSISSIPPI[151]	MISSISSIPPI[151]	MISSISSIPPI[151]
Power [kHz]	13.9	13.9	25
Time [ms]	100	100	80
Transfer 1			
Type	^{1}H-^{15}N CP	^{1}H-^{15}N CP	^{1}H-^{15}N CP
Average power [kHz]	101 (^{1}H), 45 (^{15}N)	96 (^{1}H), 41 (^{15}N)	178 (^{1}H), 66 (^{15}N)
Time [ms]	0.7	1.7	1.4
Shape	Ramp80-100% (^{1}H)	Ramp80-100% (^{1}H)	Ramp80-100% (^{1}H)
Transfer 2			
Type	^{15}N-^{13}C REDOR	^{15}N-^{1}H CP	^{15}N-^{1}H CP
Average power [kHz]	100	99 (^{1}H), 45 (^{15}N)	178 (^{1}H), 66 (^{15}N)
Time [ms]	4, 6, 10 (mixing times)	0.6	0.35
Shape	-	Ramp100-80% (^{1}H)	Ramp100-80% (^{1}H)
Transfer 3			
Type	^{15}N-^{1}H CP	^{1}H-^{13}C REDOR	^{1}H-^{13}C REDOR
Average power [kHz]	101 (^{1}H), 45 (^{15}N)	100	114
Time [ms]	0.5	0.6, 1.2 (mixing times)	0.64, 0.96 (mixing times)
Shape	Ramp100-80% (^{1}H)	-	-

Table 6: Recording parameters of solution NMR spectra of hCEACAM1-N and solid-state hNH spectra acquired at 800 MHz.

Experiment	**^{15}N-HSQC**	**hNH (CP-transfer)**	**hNH (J-transfer)**
Number of scans	44 (without Opa60), 64 (with Opa60)	16	32
Recycle delay [s]	2	0.8	0.8
Total measurement time [h]	17 (without Opa60), 25 (with Opa60)	3	7
Set temperature [K]	298	240	240
MAS frequency [kHz]	-	55	55
Hard pulse power [kHz]			
^{1}H	32	100	100
^{13}C	16	63	63
^{15}N	6	50	50
Carrier frequency [ppm]			
^{1}H	4.699	4.5	4.6
^{13}C	99.915	53.7	53.7
^{15}N	107.5	118	118.5
Spectral width [ppm]			
^{1}H	14.2	41.7	41.7
^{13}C	-	-	-
^{15}N	55	200	200
Acquisition time [ms]			
^{1}H	45.1	20.5	99.9
^{13}C	-	-	-
^{15}N	70.0	30.0	30.0
Decoupling 1			
Scheme	WALTZ-16	TPPM	TPPM
Power [kHz]	1.5	10	10
Decoupling 2			
Scheme	-	WALTZ-16	WALTZ-16
Power [kHz]	-	10	10
Water suppression			
Scheme	WATERGATE[158]	MISSISSIPPI	MISSISSIPPI
Power [kHz]	-	13.75	13.75
Time [ms]	0.132 (delay time)	100	100
Transfer 1			
Type	^{1}H-^{15}N INEPT	^{1}H-^{15}N CP	^{1}H-^{15}N INEPT
Average power [kHz]	-	100 (^{1}H), 44 (^{15}N)	-
Time [ms]	2.7	0.5	1.3
Shape	-	Ramp80-100% (^{1}H)	-
Transfer 2			
Type	^{15}N-^{1}H INEPT	^{15}N-^{1}H CP	^{15}N-^{1}H INEPT
Average power [kHz]	-	102 (^{1}H), 44 (^{15}N)	-
Time [ms]	2.7	0.5	1.3
Shape	-	Ramp100-80% (^{1}H)	-

3.2.6. Assignment, data analysis and structure calculation

3.2.6.1. Assignment of Opa60

Peaks were automatically picked using Sparky.[143] In spectra with positive signal intensity (hCANH, hcoCAcoNH, hCOcaNH, hCONH, hNcacoNH), contours were adjusted until peak picking resulted in ~10 negative peaks, which were subsequently deleted. In spectra with both negative and positive intensities (hcaCBcaNH, hcaCBcacoNH), contours were adjusted until the number of picked peaks roughly matched the expected number as determined by the size of the β-barrel (77 residues).[27] Peak lists were used as an input to the automated assignment software FLYA.[159] Assignment was conducted for HN, N, CA, CB and CO atoms, with chemical shift tolerances of 0.07 (^{1}H) or 0.4 (^{13}C, ^{15}N) ppm. 20 runs with 50 populations and 15,000 iterations were used. The result of the automated assignment is shown in Appendix 7.3.1.

After automated assignment, FLYA results were manually confirmed and extended with Sparky. The HNhhNH spectrum was used to find through-space connectivity to define the β-barrel fold of Opa60. A complete resonance list is given in Appendix . In Appendix 7.3.3, projections of spectra with assignment are shown, and in Appendix 7.3.4, a Cα-based backbone walk is shown.

3.2.6.2. Structure calculation of Opa60

The structure of Opa60 was determined with the software CYANA.[160,161] As input, the HNhhNH-derived restraints were entered as upper and lower distance limits.[162] TALOS-N[163] angle restraints were included (“strong” predictions only). A full list of restraints is given in Appendix 7.4.1. 100 structures were calculated with 10,000 annealing steps and the 20 lowest energy structures are included in the result. The output of the CYANA structure calculation is given in Appendix 7.4.2 . The structure was analyzed with UCSF Chimera 1.14.[164] The RMSD was calculated with Chimera for the region of Opa60 where HN and N backbone assignments were available (9-16, 56-62, 67-73, 115-125, 133-144, 192-201, 207-216, 225-237). Pictures were generated with Chimera.

3.2.6.3. Assignment, data analysis and structure calculation of SH3

Spectra of SH3 were processed with Bruker TopSpin 3.5.7./4.0.8 and analyzed with CcpNMR.[165,166] The assignment of SH3 has been previously published.[101,167] TREDOR data were fitted as described in section 3.2.7.2. The structure was calculated using CYANA.[160,161] Input data were the extracted TREDOR restraints, entered as upper and lower distance bounds with a 10% error imposed due to geometrical considerations,[126] as well as TALOS-N[163] "strong" angle predictions. Angle restrains which were violated by more than 50° (Ψ angle of Asn38 and Φ angle of Lys39) were removed for the final structure calculation. All restraints are given in Appendix 7.5.1. 100 structures were calculated with 10,000 annealing steps. The 20 lowest energy structures were included in the analysis and the CYANA output is given in Appendix 7.5.2. RMSD calculations were performed for residues 11-58 in Chimera 1.14.[164] Per-residue analysis and the comparison to the crystal structure (PDB: 2NUZ) were performed with a Python[168] script within Chimera (Appendix 7.5.3). Pictures were generated in Chimera.

3.2.7. TREDOR

3.2.7.1. TREDOR pulse sequence

The TREDOR pulse sequences were published[134] and are shown in Figure 3. Two versions of TREDOR have been developed, namely N-C (Figure 3A) and H-C (Figure 3B) TREDOR. In brief, N-C TREDOR starts out with a CP step from ^{1}H to ^{15}N, from where magnetization is transferred with a REDOR period to ^{13}C. REDOR is implemented with two 180° pulses per rotor period[122] and the pulses are phase cycled according to the XY-8 scheme.[152] A selective REBURP[153] pulse is placed in the middle of the REDOR periods.

The ^{15}N and ^{13}C chemical shifts are coevolved, where the evolution times are scaled relative to each other by the gyromagnetic ratio of the nuclei to enable correct displaying of shifts on one ppm scale:

$$t_{1,C} = t_{1,N} * \frac{\gamma_{^{15}N}}{\gamma_{^{13}C}} \tag{26}$$

A second REDOR period transfers the magnetization back to ^{15}N and a z-filter period follows. ^{15}N chemical shift is evolved. MISSISSIPPI water suppression[151] is split before and after this

evolution period. Magnetization is transferred back to ^{1}H for detection. Heteronuclear decoupling sequences used are TPPM[149] on ^{1}H and WALTZ-16[150] on ^{15}N and ^{13}C.

H-C TREDOR works in the same fashion. Magnetization is first transferred via CP to ^{15}N where the shift is evolved. After a block of water suppression, magnetization is transferred back to ^{1}H and via REDOR to and back from ^{13}C. ^{1}H and ^{13}C chemical shifts are coevolved. Before detection, a z-filter period is included. Experimental parameters are given in section 3.2.5.

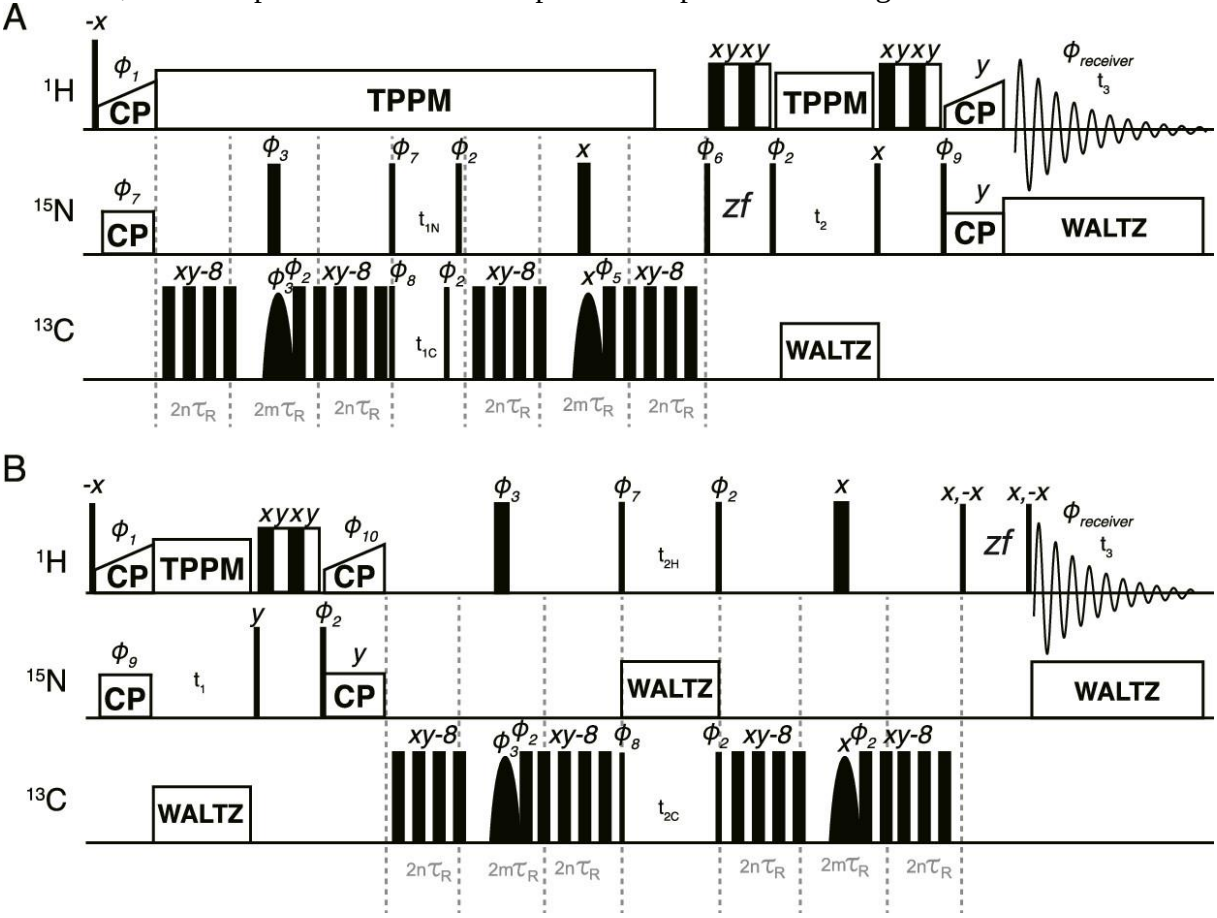

Figure 3: TREDOR pulse sequences. Narrow rectangles represent 90°, wide rectangles 180° pulses. Selective pulses are shown as rounded shapes. Phase cycles are Φ_1 = 11333311, Φ_2 = 00222200, Φ_3 = 01, Φ_5 = 0022, Φ_6 = 1133, Φ_7 = 0022, Φ_8 = 2200, Φ_9 = 0022, Φ_{10} = 2 and $\Phi_{receiver}$ = 02202002 with phases 0 = x, 1 = y, 2 = −x, 3 = −y. Unlabeled pulses have phase 0. CP: cross polarization; TPPM: two-pulse phase-modulated decoupling; WALTZ: wideband, alternating-phase, low-power technique for residual splitting decoupling; zf: z-filter period, τ_R: rotor period. Water suppression sequence is MISSISSIPPI. **A:** Pulse sequence for N-C TREDOR. **B:** Pulse sequence for H-C TREDOR.

Both N-C and H-C TREDOR can be analyzed in the same way. Here, the N-C version is explicitly introduced as in the publication.[134]

After initial CP from ^{1}H to ^{15}N, a REDOR period is employed to transfer magnetization to ^{13}C:

$$\widehat{N}_x \xrightarrow{REDOR} \widehat{N}_x c_{12} + 2\widehat{N}_y \hat{C}_z s_{12} \tag{27}$$

Terms s_{12} and c_{12} stand for:

$$s_{12} = \sin\left(\omega \frac{t_{mix}}{2}\right), c_{12} = \cos\left(\omega \frac{t_{mix}}{2}\right) \tag{28}$$

Here, ω is the dipolar coupling strength. Two 90° pulses follow to generate detectable ^{13}C magnetization alongside the detectable ^{15}N magnetization:

$$\widehat{N}_x c_{12} + 2\widehat{N}_y \hat{C}_z s_{12} \xrightarrow{90°_x(^{15}N), 90°_{-x}(^{13}C)} \widehat{N}_x c_{12} + 2\widehat{N}_z \hat{C}_y s_{12} \tag{29}$$

The chemical shift is coevolved followed by another set of two 90° pulses in preparation of the second REDOR period:

$$\begin{aligned} \widehat{N}_x c_{12} + 2\widehat{N}_z \hat{C}_y s_{12} &\xrightarrow{t_{1,^{15}N}, t_{1,^{13}C}} \widehat{N}_x c_{12} \cos\left(\Omega_{^{15}N} t_{1,^{15}N}\right) \\ &+ 2\widehat{N}_z \hat{C}_y s_{12} \cos\left(\Omega_{^{13}C} t_{1,^{13}C}\right) \xrightarrow{90°_x(^{15}N), 90°_x(^{13}C)} \widehat{N}_x c_{12} \cos\left(\Omega_{^{15}N} t_{1,^{15}N}\right) \\ &- 2\widehat{N}_y \hat{C}_z s_{12} \cos\left(\Omega_{^{13}C} t_{1,^{13}C}\right) \end{aligned} \tag{30}$$

Ω is the chemical shift of the respective nucleus. The second REDOR period converts the magnetization back into N_x magnetization:

$$\begin{aligned} &\widehat{N}_x c_{12} \cos\left(\Omega_{^{15}N} t_{1,^{15}N}\right) \\ &\quad - 2\widehat{N}_y \hat{C}_z s_{12} \cos\left(\Omega_{^{13}C} t_{1,^{13}C}\right) \xrightarrow{REDOR} \widehat{N}_x \left[c_{12}{}^2 \cos\left(\Omega_{^{15}N} t_{1,^{15}N}\right)\right. \\ &\quad \left. + s_{12}{}^2 \cos\left(\Omega_{^{13}C} t_{1,^{13}C}\right)\right] \end{aligned} \tag{31}$$

Subsequently the N_x magnetization is frequency labeled with the ^{15}N chemical shift to expand the spectrum into a third dimension. In the end, the pulse sequence ends with detection on ^{1}H.

Spin systems in reality, particularly in proteins, are bigger than the two-spin N-C system considered so far. For a three spin system N-C_2, the analysis follows the same principles, however more couplings have to be considered and lead to the emergence of multiple quantum terms. One of these generates detectable magnetization during the first evolution period:

$$-4\widehat{N}_x \hat{C}_{2y} \hat{C}_{3y} s_{12} c_{12} \cos\left(\Omega_{^{15}N} t_{1,^{15}N}\right) \cos\left(\Omega_{2,^{13}C} t_{1,^{13}C}\right) \cos\left(\Omega_{3,^{13}C} t_{1,^{13}C}\right) \tag{32}$$

This term produced artifacts in the spectra, however the exact placement of these can be influenced by the offset placement (see Appendix 7.5.4 for an example spectrum showing artifacts).

The TREDOR parameter ζ, which is fitted to extract the dipolar coupling and thus the distance between two nuclei, is formed as the ratio of the transferred (TEDOR) signal and the transferred and non-transferred (REDOR) signal. The TEDOR signal intensity V_{1i} between a ^{15}N spin 1 and a coupled ^{13}C spin I takes the form:

$$V_{1i}(t_{mix}) = V_1(0)e^{-\Gamma_1 t_{mix}} \langle sin^2(\omega_{1i}t_{mix}/2) \prod_{k=1\neq i}^{n_i} cos^2(\omega_{1k}t_{mix}/2)\rangle \quad (33)$$

Γ_1 is the coherence decay rate. The REDOR signal intensity V_1 is given as:

$$V_1(t_{mix}) = V_1(0)e^{-\Gamma_1 t_{mix}} \langle cos^2(\omega_{1i}t_{mix}/2) \prod_{k=1\neq i}^{n_i} cos^2(\omega_{1k}t_{mix}/2)\rangle \quad (34)$$

Forming the ratio ζ_{1i} yields:

$$\begin{aligned}\zeta_{1i}(t_{mix}) &= \frac{V_{1i}(t_{mix})}{V_1(t_{mix}) + V_{1i}(t_{mix})} \\ &= \frac{\langle sin^2(\omega_{1i}t_{mix}/2) \prod_{k=1\neq i}^{n_i} cos^2(\omega_{1k}t_{mix}/2)\rangle}{\langle cos^2(\omega_{1i}t_{mix}/2) \prod_{k=1\neq i}^{n_i} cos^2(\omega_{1k}t_{mix}/2)\rangle + \langle sin^2(\omega_{1i}t_{mix}/2) \prod_{k=1\neq i}^{n_i} cos^2(\omega_{1k}t_{mix}/2)\rangle} \\ &\approx \langle sin^2(\omega_{1i}t_{mix}/2)\rangle\end{aligned} \quad (35)$$

The dipolar coupling can be extracted by fitting ζ_{1i} with a Bessel function:[125]

$$\zeta_{1i}(t_{mix}) = \frac{1}{2}\left[1 - (J_0\left[\sqrt{2}D_{1i}t_{mix}\right])^2\right] \quad (36)$$

The TREDOR fitting procedure can in principle be easily extended to the simultaneous fitting of multiple curves, as occurs in a realistic sample where one nucleus experiences multiple couplings. In this work, however, the single curve fitting was used.

3.2.7.2. TREDOR fitting

TREDOR data were fitted with a MATLAB R2016b[169] script under Equation (36). The best fit was determined using χ^2 reduction. The fitting error was determined using 100 Monte Carlo runs. Data was plotted in R 4.0.0.[170]

3.2.7.3. TREDOR simulations

The TREDOR simulation was performed by Dr. Evgeny Nimerovsky. The simulation for the TREDOR Bessel function approximation was performed with in-house MATLAB[169] scripts. The theoretical foundation has been previously described.[125]

4. Results

4.1. Opa60

4.1.1. Structure of Opa60

For structure determination of the membrane protein Opa60 in native-like lipid bilayers, a perdeuterated, uniformly $^{13}C/^{15}N$-labeled sample in DMPC-bilayers was prepared. A set of backbone assignment spectra was recorded at 800 and 600 MHz spectrometers at 55 kHz MAS, namely hCANH/hcoCAcoNH, hCOcaNH/hCONH, hcaCBcaNH/hcaCBcacoNH and hNcacoNH. Proton linewidths were in the range of 130-200 Hz, nitrogen linewidths were 60-80 Hz and carbon linewidths were 90-150 Hz. After automated peak picking, an automated assignment was carried out using FLYA. The result is shown in Appendix 7.3.1. The automated assignment was manually confirmed and extended where possible. A total of 81 residues were assigned based on the availability of the backbone amide group assignment. A full resonance list is given in Appendix 7.3.2. An N-C-projection with assignments is shown in Figure 4. The number of peaks automatically picked in the projection at the contour level shown was 85, of which 66 could be assigned in the projection. Projections of further assignment spectra are shown in Appendix 7.3.3, and an exemplary Cα-based backbone walk is shown in Appendix 7.3.4.

Restraints for a structure calculation with CYANA were extracted from a 4D HNhhNH spectrum. Here, through-space contacts were identified as hydrogen bonds across neighboring β-strands of the barrel and entered as upper and lower distance restraints. Torsion angle restraints were generated with TALOS-N. A full list of restraints is given in Appendix 7.4.1. The 20 lowest energy structures (CYANA target function ranging from 0.85 to 11.30) were aligned using UCSF Chimera for residues classified as being in the β-sheet (9-16, 56-62, 67-73, 115-125, 133-144, 192-201, 207-216, 225-237), and the structure bundle revealing the β-barrel is shown in Figure 5A. Thus, 74 of 81 assigned residues were in a β-sheet confirmation and the sheet consisted of 78 residues of which four were not assigned (two Pro with no amide H available) but are integrated in the sheet. The backbone heavy-atom (Cα, N, C, O) RMSD of the β-sheet region is 2.3 Å. The CYANA output is given in Appendix 7.4.2. The β-barrel exhibited a shear. No assignments were available for the loop regions and this resulted in no structural definition of these. This is illustrated in Figure 5B, which shows the 20 lowest energy structures as in Panel A, but with all residues visible. A topology map of Opa60 with availability

of assignments and hydrogen bond restraints is shown in Figure 5C. The edges of the β-barrel (residues in squares) were defined as either a "strong" classification by TALOS-N or the availability of a hydrogen bond restraint.

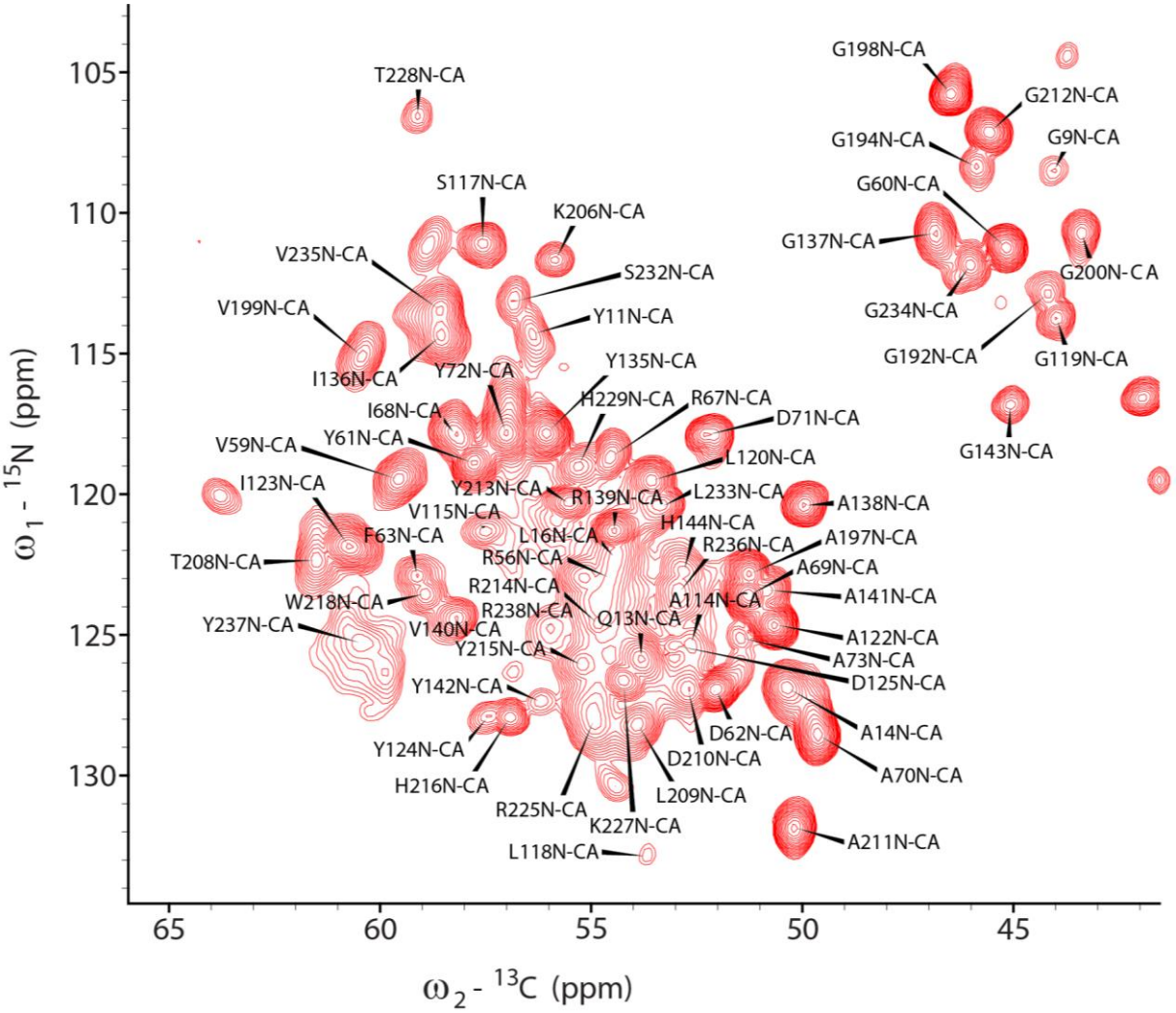

Figure 4: N-C-projection of hCANH-spectrum of perdeuterated Opa60 recorded at 800 MHz. Peak assignments of 66 residues from the manual assignment are given.

An example of a hydrogen bond restraint as observed in the HNhhNH spectrum is shown in Figure 6A for residues Ala69 and Ser121. The peak in the spectrum is shown alongside the resulting structure after structure calculation, where the hydrogen bond is indicated.

A fully protonated sample of Opa60 in deuterated DMPC was prepared to extend the assignments further to Hα which in principle also could result in additional restraints. Spectra were recorded at a 950 MHz spectrometer at 100 kHz MAS, namely hNCAHA, hCOCAHA, hCCH and hXhhXH (where X stands for N or C and thus, in principle four spectra were acquired simultaneously).[157] The spectra suffered from strong overlap due to broad lines, as well as low sensitivity for the hXhhXH spectrum. With the combination of the four spectra, a total of 65 Hα atoms were assigned. A total of five Hα-Hα distance restraints were found in the

hXhhXH spectrum (in the hChhCH subspectrum). These were not included in the structure calculation as these were a confirmation of the amide contacts. An example is shown in Figure 6B, highlighting the availability of Pro contacts as opposed to the HNhhNH-based structural restraints. All Hα assignments and the identified Hα contacts are given in Appendix 7.4.3.

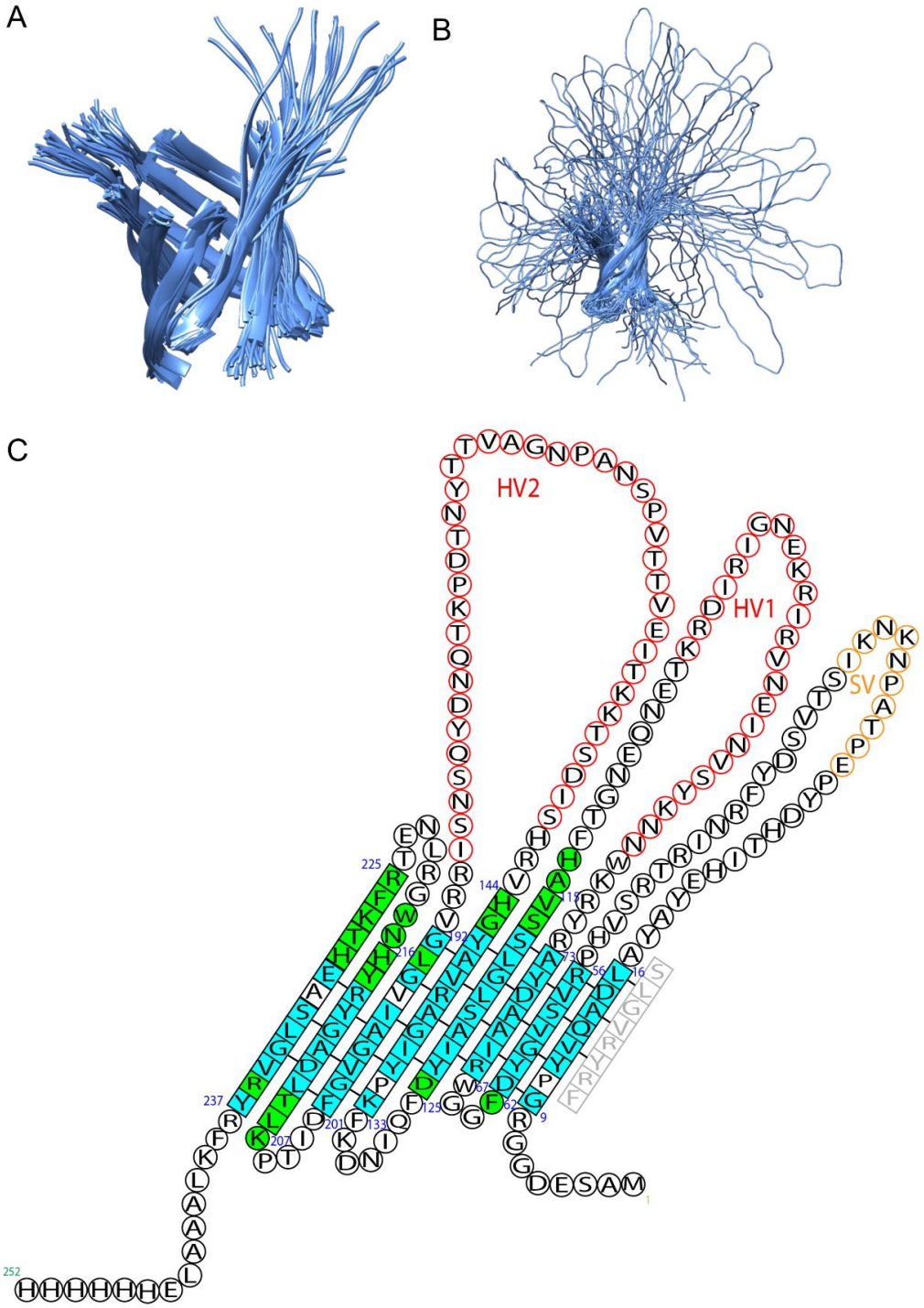

Figure 5: The structure of Opa60 in DMPC bilayers. **A:** Overlay of the 20 lowest energy structures from the CYANA structure calculation, aligned in the β-barrel region where amide assignments were available. Heavy-atom backbone RMSD is 2.3 Å. **B:** 20 lowest energy structures aligned as in **A**, but with the disordered loop regions shown, where no restraints where available. **C:** Topology map of Opa60 in DMPC. Green residues: amide assignment available, blue: amide assignment and hydrogen bond restraint available, square: residue in β-sheet conformation as determined by TALOS-N ("strong" predictions) or availability of hydrogen bond restraint. Regions HV1/HV2/SV are indicated.

To assess whether the resonances of the mobile loops can be recorded in spectra that employ J-mediated transfer, an INEPT-version of the hNH experiment was recorded and compared with the CP-based spectrum. No significant differences were observed (spectra shown in Appendix 7.3.5). The short coherence lifetime (^{1}H T_2 time of around 5 ms) prevented the recording of INEPT-based higher-dimensional spectra such as hCANH.

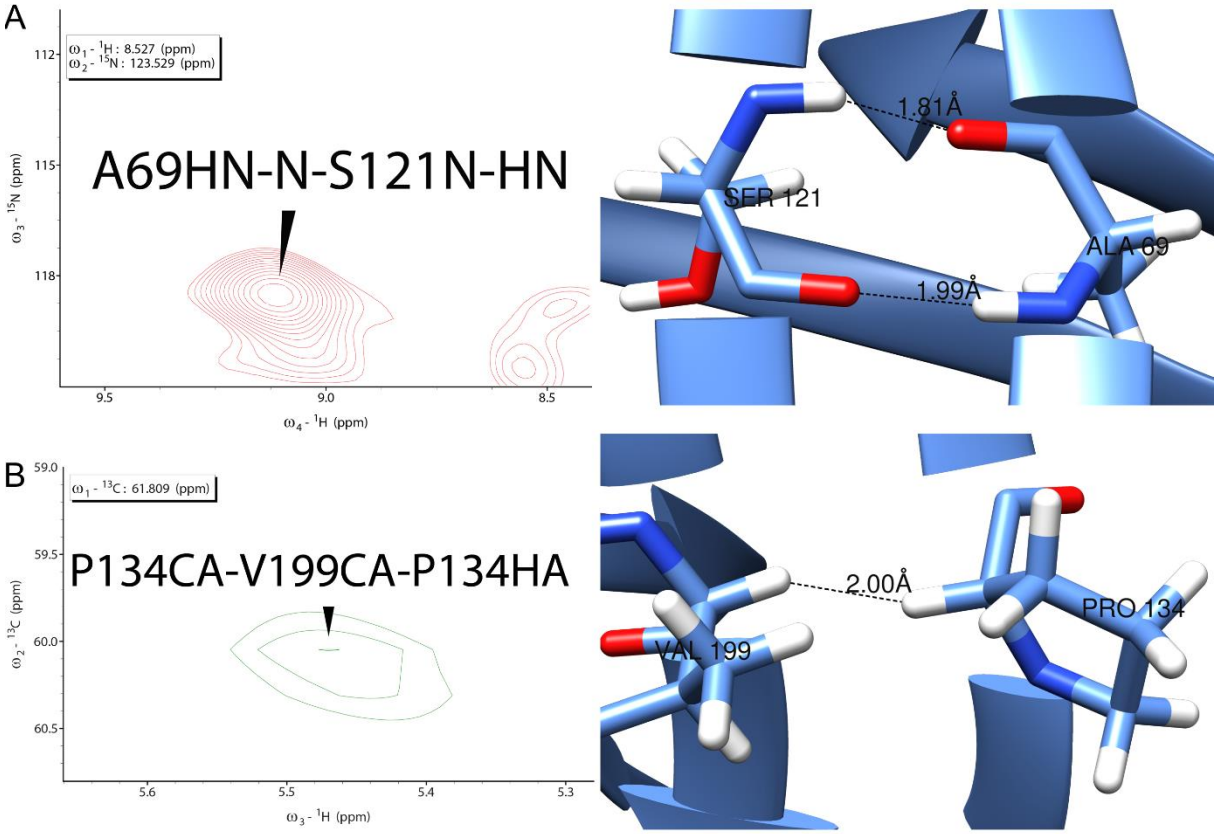

Figure 6: Structural restraints for Opa60 in DMPC bilayers. **A:** Hydrogen bond restraint between Ala69 and Ser121 as observed in the HNhhNH spectrum (left) observed on the deuterated Opa60 sample at 800 MHz. The restraint was used for structure calculation and is indicated on the final structure (right). **B:** Hα-Hα contact between Pro 134 and Val 199 observed on the fully protonated sample in deuterated DMPC at 950 MHz in the hXhhXH spectrum (left). The restraint was not included in the structure calculation but is shown on the final structure (right).

Opa60 samples with 20% glycerol were prepared to record spectra under FROSTY-NMR conditions[171–173] (Appendix 7.3.6), however at lower spinning and temperature, no clear difference was seen and only a decrease in spectral resolution was observed.

4.1.2. Interaction of Opa60 with hCEACAM1-N

The native function of Opa60 is the interaction with different variants of human host receptors of the hCEACAM-family. The interaction of Opa60 with the N-terminal domain of hCEACAM1 (hCEACAM1-N) was first assessed using solution NMR. Here, a ^{15}N-HSQC spectrum of purified ^{15}N-labeled hCEACAM1-N was recorded at 800 MHz. 0.15% (w/v) DPC

was added to the solution and the protein retained its folded state. Subsequently, an equimolar amount of unlabeled Opa60 was added and another ^{15}N-HSQC spectrum recorded. An overlay of the two spectra is shown in Figure 7. Particularly in the expansion, the emergence of a new set of peaks upon addition of Opa60 was observed.

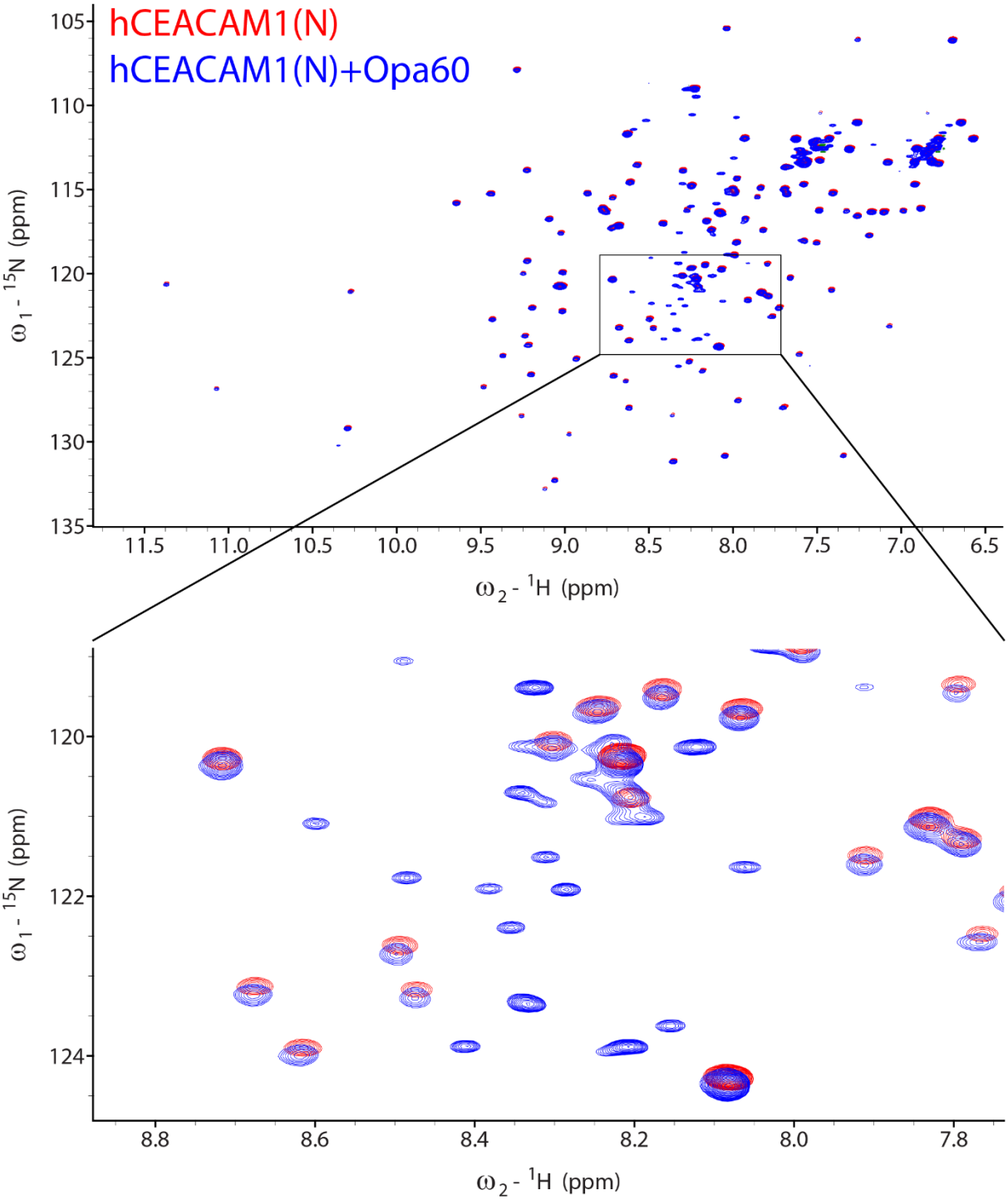

Figure 7: ^{15}N-HSQC spectra of ^{15}N-hCEACAM1-N alone (red) or with equimolar ratio of unlabeled Opa60 (blue) recorded at 800 MHz. The region in the square is shown in the bottom expansion and reveals the emergence of a new set of peaks in the blue spectrum. Spectra have been shifted relative to each other for visibility.

With this first indication of binding between Opa60 and hCEACAM1-N, a sample of Opa60 in lipid bilayers was prepared to facilitate the binding also in a more native environment. Specifically, the lipid composition was (in molar percentages) 63% DMPC, 16% DMPG, 16% cholesterol and 5% DMPE-PEG1000.[30] Lipid bilayers were obtained by dialysis and subsequently sonicated. A lipid control was prepared the same way. Protein and lipid control were incubated with hCEACAM1-N and subsequently centrifuged. Pellet and supernatant were

analyzed via SDS-PAGE for a binding of hCEACAM1-N to the proteins or the lipids alone. The resulting gel is shown in Figure 8.

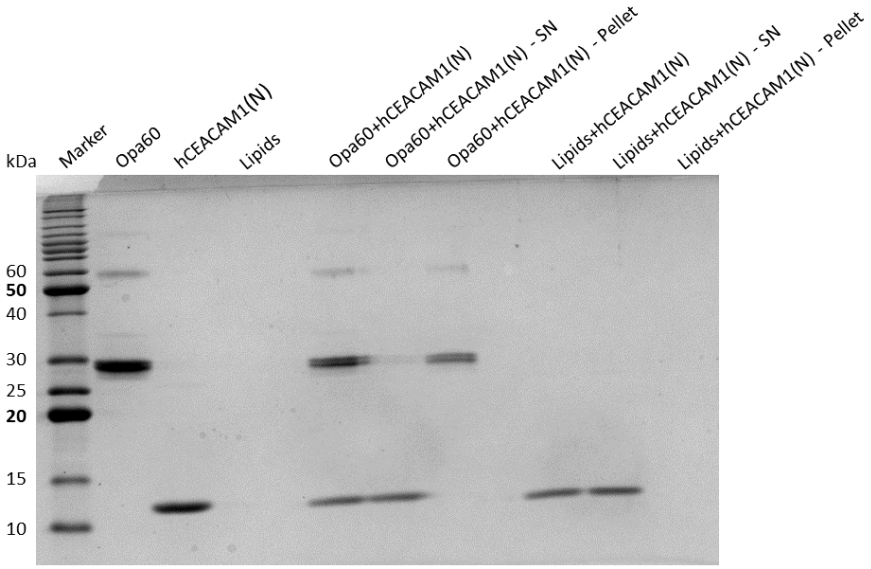

Figure 8: SDS-PAGE analysis of the interaction experiment between Opa60 in lipid bilayers consisting of DMPC, DMPG, cholesterol and DMPE-PEG1000. Opa60: Opa60 in lipids before sonication. Folded Opa60 can be seen as the strongest band in this lane. Both Opa60 and the lipid control were incubated with hCEACAM1-N and the pellet was obtained via centrifugation. In both cases, no hCEACAM1-N was observed in the pellet but in the supernatant.

After centrifugation, Opa60 was found in the pellet, whereas no hCEACAM1-N was found. In the lipid control, no hCEACAM1-N was in the pellet either. Additional bands on the gel were seen at higher molecular weight for Opa60. No binding could be concluded from this experiment.

4.1.3. Opa60 in different lipids

The functionality of membrane proteins such as Opa60 is heavily influenced by the surrounding lipids. In particular, bacterial outer membranes contain LPS and, in the case of *N. gonorrhoeae*, LOS. It is thus of interest to characterize Opa60 also in LPS/LOS. LOS is not commercially available, however, Kdo2-lipid A (KLA) is structurally close to the core region of LOS and was chosen. Additionally, two LPS species (Rd2 LPS from *E. coli* strain F583 and LPS from strain and K235) were tested. Samples of perdeuterated Opa60 in these different lipids were prepared such that the number of acyl chains in comparison to the DMPC-sample (LPR 0.25) was retained. hCANH spectra were recorded at 800 MHz and 55 kHz MAS. An overlay of the four N-C-projections is shown in Figure 9. No obvious differences in between the four samples was observed besides intensity differences. In particular, also the 3D versions revealed no major

chemical shift perturbations (CSPs). Residues showing minor CSPs in the projection are Leu118, and Ser232, both located within the β-barrel region.

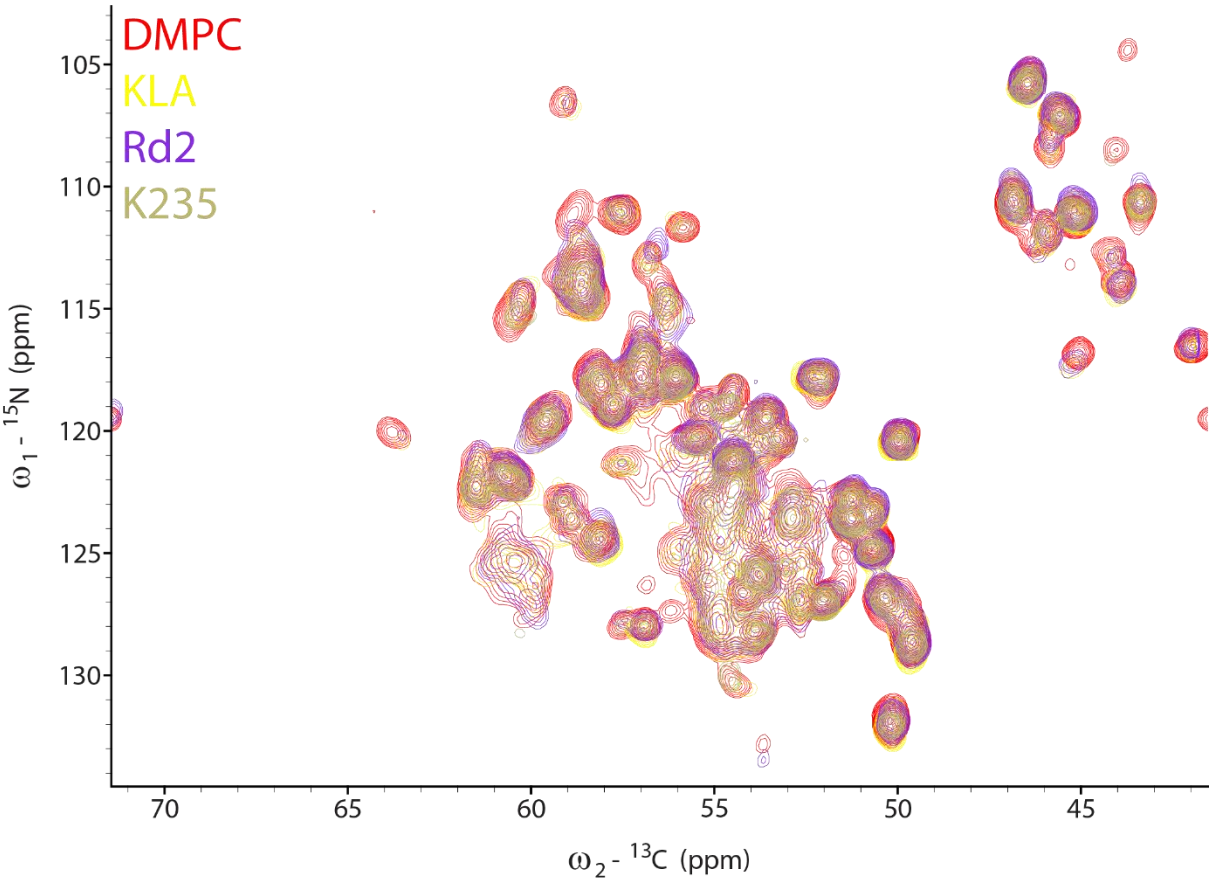

Figure 9: Overlay of N-C projections of four hCANH spectra recorded at 800 MHz of perdeuterated Opa60 in four different lipids, DMPC (red), Kdo2-lipid A (KLA, yellow) and LPS from *E. coli* strains Rd2 (purple) and K235 (green). Contours have been adjusted to the same level.

4.2. TREDOR

4.2.1. Characterization of TREDOR fitting

The results presented in this section have been published.[134] To characterize the TREDOR method for determination of internuclear distances and to calibrate the fitting procedure, a set of N-Cα TREDOR spectra with different mixing times (0.14, 1.4, 2.9, 4.3, 5.8, 7.2, 8.6, 10.1 ms) was recorded on perdeuterated SH3 at a 600 MHz spectrometer in order to determine the one-bond N-Cα distance for Gly51. A 2D plane of the spectrum with 5.8 ms mixing time is shown in Figure 10A. Figure 10B shows the behavior of signal intensities under different mixing times. The (REDOR, non-transferred) signal can be seen to decrease with increasing mixing time with an increase at first in Cα (TEDOR, transferred) peak intensity, whose intensity

then declines with longer mixing times. Intensities were extracted, the TREDOR parameter ζ calculated and fitted to the dipolar coupling. The fit is shown in Figure 10C. As is also shown in this panel, the theoretical one-bond distance between N and Cα is 1.45 Å, resulting in a dipolar coupling of 1,005 Hz.[174] This is compared to the fitted value of 810 Hz (or 798 Hz when numerically simulated with the given distance of 1.45 Å). Taking the ratio resulted in an overall scaling factor of 0.8, which was used in all subsequent distance determinations.

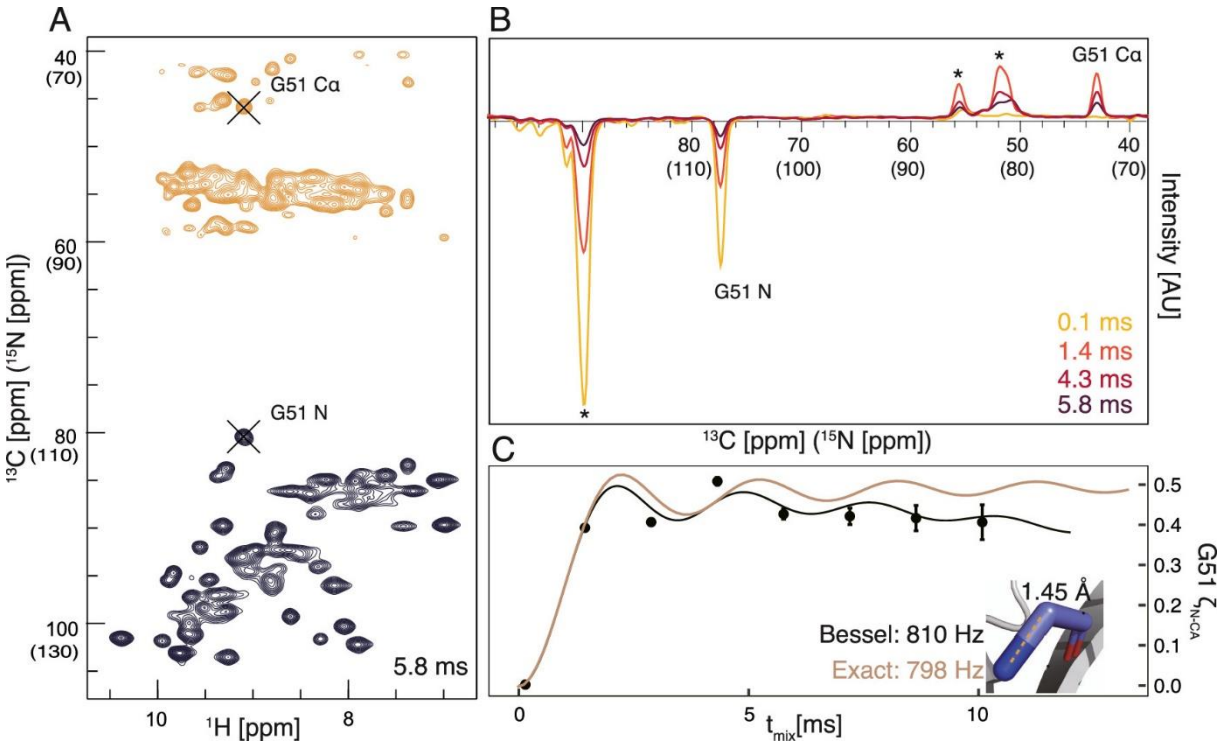

Figure 10: TREDOR fitting of one-bond N-Cα distance of Gly51 in the microcrystalline SH3 domain. **A:** 2D plane of TREDOR spectrum with 5.8 ms mixing time. Peaks of Gly51 N and Cα are labeled. Positive signals are yellow and negative signals are black. Chemical shifts on the shared vertical axis in parentheses correspond to ^{15}N. **B:** 1D traces showing the behavior of signal intensities for Gly51 N and Cα at different mixing times. Asterisks indicate overlapped signals from other residues (Arg18, Lys59, Ile30 and Glu45). **C:** Fitting of the N-Cα distance of Gly51 (shown on the crystal structure (PDB: 2NUZ) in the inset) with a Bessel function approximation (black) and an exact numerical simulation (brown) corresponding to a distance of 1.45 Å.

A set of three N-Cx (Cx standing for all sidechain carbon atoms) TREDOR spectra with different mixing times (4, 6 and 10 ms) were recorded on SH3 and the spectra were assigned. In the following, only structural relevant restraints were considered. These were defined as all distances which are three or more covalent bonds apart and thus define a torsion angle or spatial proximity of residues. Examples of the spectra are shown in Figure 11B and C for residues Trp42 (sidechain nitrogen Nε) and Val9 for all three mixing times. For Trp42, a long-range contact to Cβ of Ala55 can be seen. The fittings as well as extracted dipolar couplings are shown in Figure 11D and E. The TREDOR fitting procedure is shown to yield accurate distance information also when used with only two or even one of the mixing times. The correlation between the three-point fits with the two- or one-point fits is shown in Figure 11A. Using only

the 4 ms mixing time led to most outliers, followed by the 10 ms mixing time. Exemplary fittings are also shown in Figure 11D and E.

Relevant structural restraints could also be obtained with H-CO TREDOR with mixing times of 0.6 and 1.2 ms. For most residues, the intra- and sequential contacts were observed and in some cases also long-range contacts. Exemplary spectral extracts are shown in Figure 11F. Long-range contacts can be seen betweenTrp42 Hε and N38 CO as well as Gly51 HN and Val44 CO. Distances were extracted by fitting the dipolar oscillation curves. All fitting curves ca be found in the supporting information of the publication.[134] The structure determination of SH3 with these restraints is described in section 5.2.3.

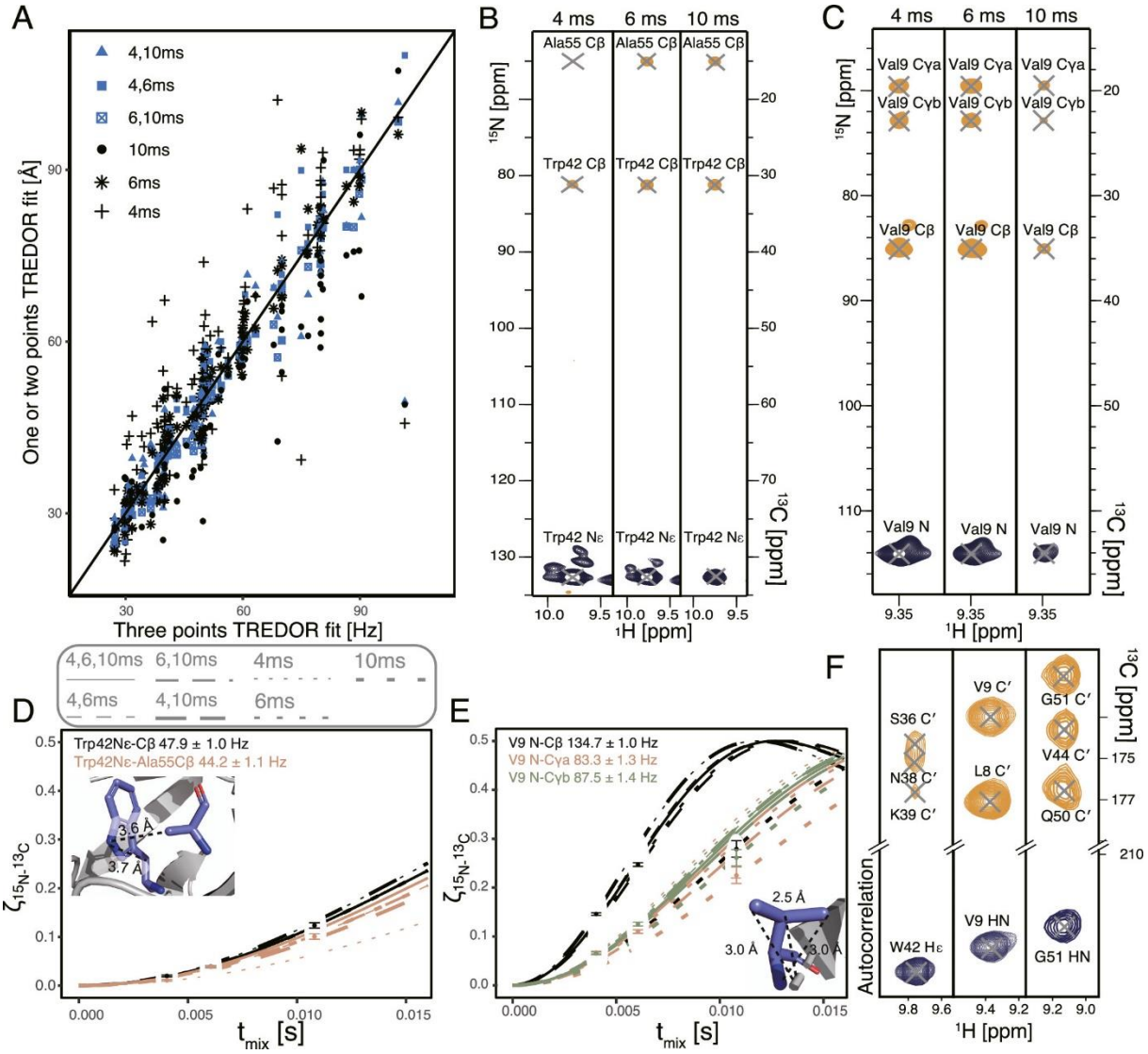

Figure 11: TREDOR fitting for distance determination in SH3. **A:** Correlation of distances determined using three mixing times of N-Cx TREDOR as compared with two (blue symbols) or one (black symbols) mixing times only. **B:** Strips of N-Cx spectra at three different mixing times for Nε of Trp42. Peak assignments are indicated. Positive signals are yellow and negative signals are black. **C:** Same as **B** for residue Val9. **D:** Fitting of distance for Trp42 Nε from panel **B**. Distances are shown on the crystal structure (PDB: 2NUZ) in the inset and fitted values are given. Fits with only two or one data points are shown additionally. **E:** Same as **D** for Val9. **F:** TREDOR H-CO strips from 3D experiment with 1.2 ms mixing time shown for three residues with assignment indicated. Positive signals are yellow and negative signals are black.

So far, only the internal consistency of the TREDOR method was investigated. In order to demonstrate the faithfulness of the structure calculated with TREDOR data, the measured distances were compared with distances extracted from the SH3 crystal structure (PDB: 2NUZ). To compare the TREDOR method with the older TEDOR method, distances were also determined using TEDOR and included in the comparison. The correlation plot is shown in Figure 12. For this comparison, long-range contacts as well as ambiguously assigned contacts were excluded. Overlapped residues in the TREDOR spectra are marked in gray. Here, peaks in the spectra showed strong overlap. Compared with TEDOR, TREDOR distances resembles the crystal distance more accurately. (R^2 of 0.82 versus 0.30).

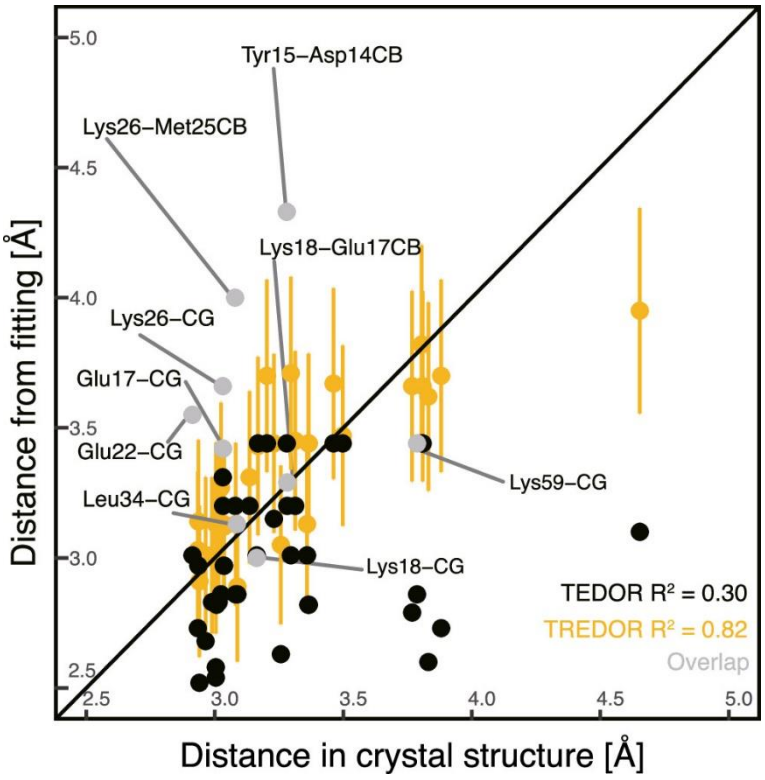

Figure 12: Correlation of TREDOR (yellow, gray) and TEDOR (black) distances with distances obtained directly from the crystal structure (PDB: 2NUZ). Error bars indicate 10% error. Gray symbols indicate overlapped peaks. No long-range or ambiguous contacts were included in this plot. R^2 values are indicated.

4.2.2. Coherence decay under TREDOR

The transverse coherence decay rate under TREDOR was determined in a per-residue fashion and compared with the decay rate in an hNH experiment. It was found that under TREDOR, the rate is higher. A plot comparing these site-specific rates is shown in Figure 13A, the individual signals are shown as an hNH spectrum in Figure 13B. The rates could be fitted with a single exponential. Examples are shown in Figure 13C-E for Ala55, Gly51 and Trp42 (Nε). The hNH data (yellow curves) show a longer T_2 time when compared to the corresponding non-transferred and transferred TREDOR signals (black and blue curves). The single exponential fits imply the predominance of one relaxation process in the overall decay rate. A list of all determined T_2 times is given in Appendix 7.5.5. $T_2\rho$ times were measured under different spin lock field and were generally longer than T_2 times.[134]

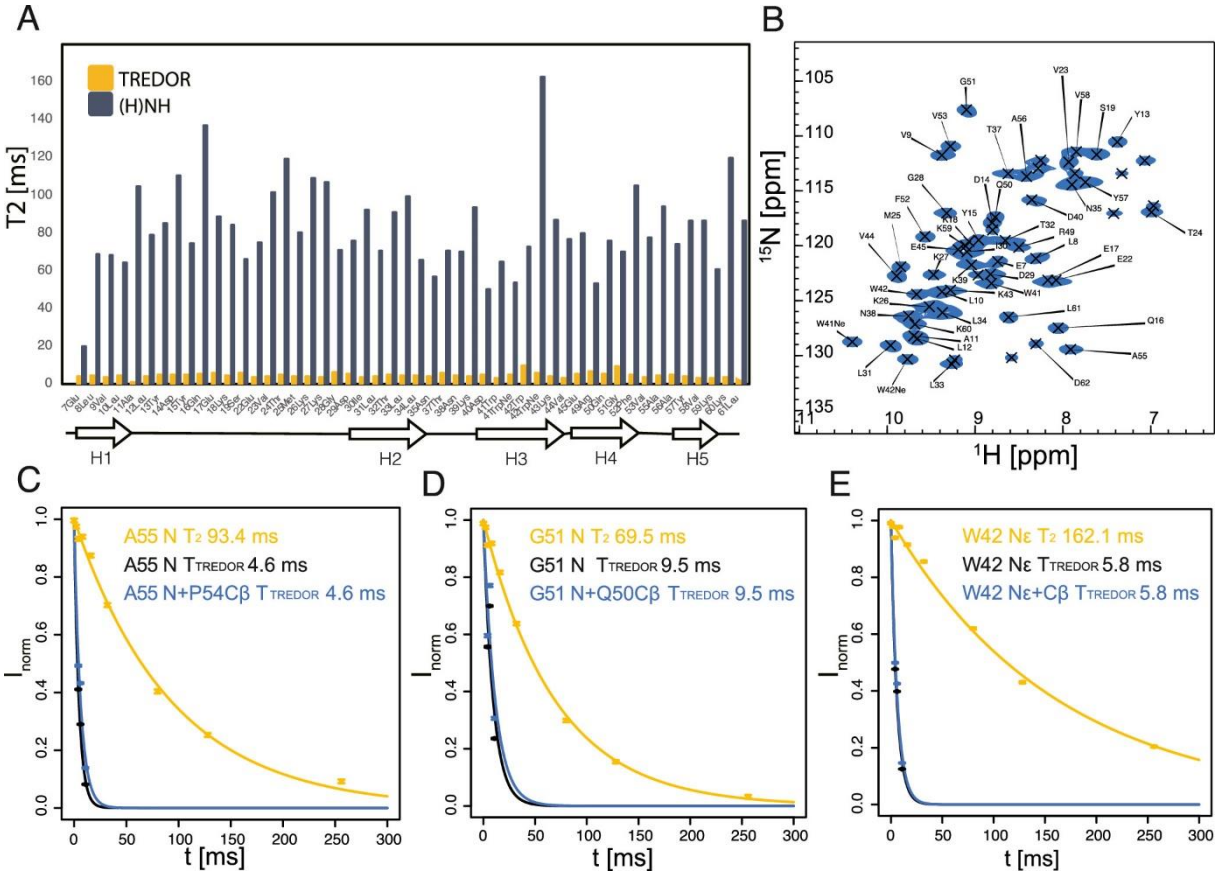

Figure 13: Transverse coherence decay rate under TREDOR and hNH In the protein SH3. **A:** Comparison of TREDOR T_2 times (yellow) and hNH T_2 times (dark blue). Data are shown for each residue and β-sheets are indicated below the graph. **B:** hNH of SH3 with assignments. **C-E:** Single exponential fits to the decay rates from hNH (yellow), non-transferred (black) and transferred (blue) TREDOR signals. T_2 times are indicated and are generally longer for hNH signals.

4.2.3. SH3 structure calculation with TREDOR

The distances obtained from fitting data from N-Cx and H-CO TREDOR as described in section 4.2.1 were used as an input for a CYANA structure calculation to determine the structure of SH3. Specifically, 17 medium -range contacts (contacts two to four residues apart, 5 N-Cx, 12 H-CO), 34 long-range contacts (contacts more than four residues apart, 18 N-Cx, 16 H-CO) and 109 intra- or interresidual (83 N-Cx, 26 H-CO) contacts defining torsion angles. A full list of restraints is given in Appendix 7.5.1. Additionally, TALOS-N angle restraints ("strong" predictions) were included in the structure calculation. These are also given in Appendix 7.5.1.

The resulting structural bundle of the 20 lowest energy structures is shown in Figure 14A. Shown are residues 11-58 which comprise the structured core of SH3. The backbone RMSD for these residues is 1.8 Å. The TREDOR structure (lowest energy) is compared to the crystal structure (PDB: 2NUZ) in Figure 14B. The RMSD between the structures, again comparing residues 11-58, is 2.1 Å. A residue-specific comparison and a mapping on secondary structure

elements of SH3 is shown in Figure 14C for both crystal conformers A and B. Moreover, this panel shows the usefulness of TREDOR backbone-to-sidechain (H-Cx found in the H-CO spectrum, last seven contacts in list in Appendix 7.5.1) contacts for structure definition. Plots are shown with and without these, and an improvement in RMSD with these contacts was observed. This trend was particularly pronounced for the loop regions of SH3.

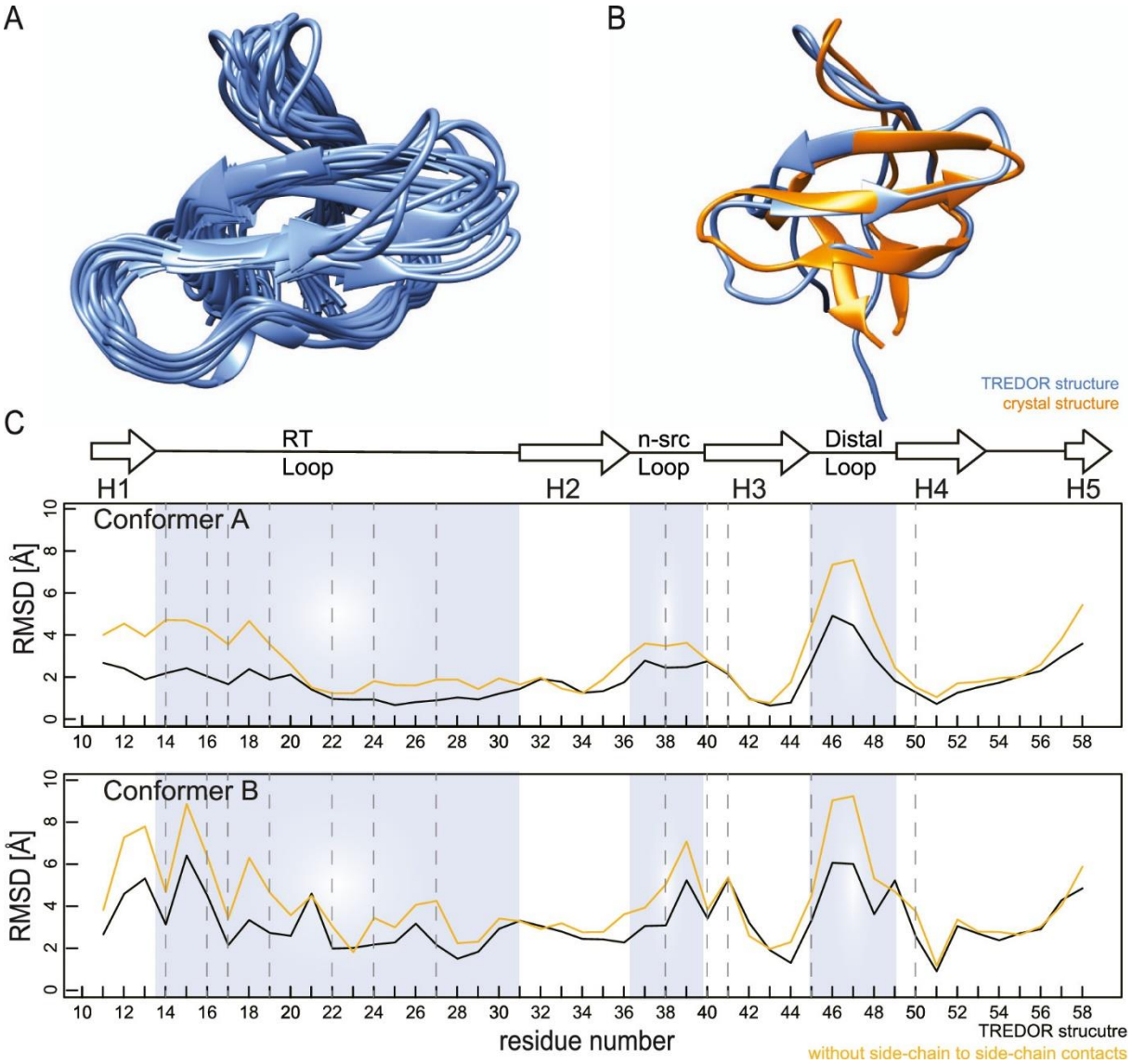

Figure 14: Structure of SH3 determined with TREDOR N-Cx and H-CO. **A:** Bundle of 20 lowest energy structures. Shown are residues 11-58. Backbone RMSD is 1.8 Å. **B:** Overlay of the lowest energy structure with the crystal structure (PDB: 2NUZ). Shown and aligned are residues 11-58. Backbone RMSD between the two structures is 2.1 Å. **C:** RMSD plotted per residue for the TREDOR structure against both conformers of the crystal structure (PDB: 2NUZ). Secondary structure elements of SH3 are indicated, arrows indicate β-strands. RMSD is plotted with and without the inclusion of backbone-to sidechain (H-Cx) contacts.

4.2.4. TREDOR applied to Opa60

TREDOR H-CO spectra of fully protonated Opa60 were acquired (mixing times 0.64 and 0.96 ms mixing time) on a 1.2 GHz spectrometer. Of interest was the acquirement of long-range

contacts for a membrane protein such as Opa60. The coherence decay is demonstrated in Figure 15A and B. Panel A shows 1D traces of SH3 TREDOR H-CO spectra (mixing times 0.58 and 1.15 ms) and panel B shows traces of spectra of Opa60 with mixing times 0, 0.64 and 0.96 ms. These revealed a similar decay rate as for SH3 with a T_2' rate of around 2.5 ms. Time constants for the decay were 0.85 ms for SH3 and 0.75 ms for Opa60. The spectra revealed sequential or intraresidual contacts and one long-range contact Gly212 N to Ser232 CO. Figure 15C shows this long-range contact and demonstrates the absence of another for Gly198 N to Tyr135 CO.

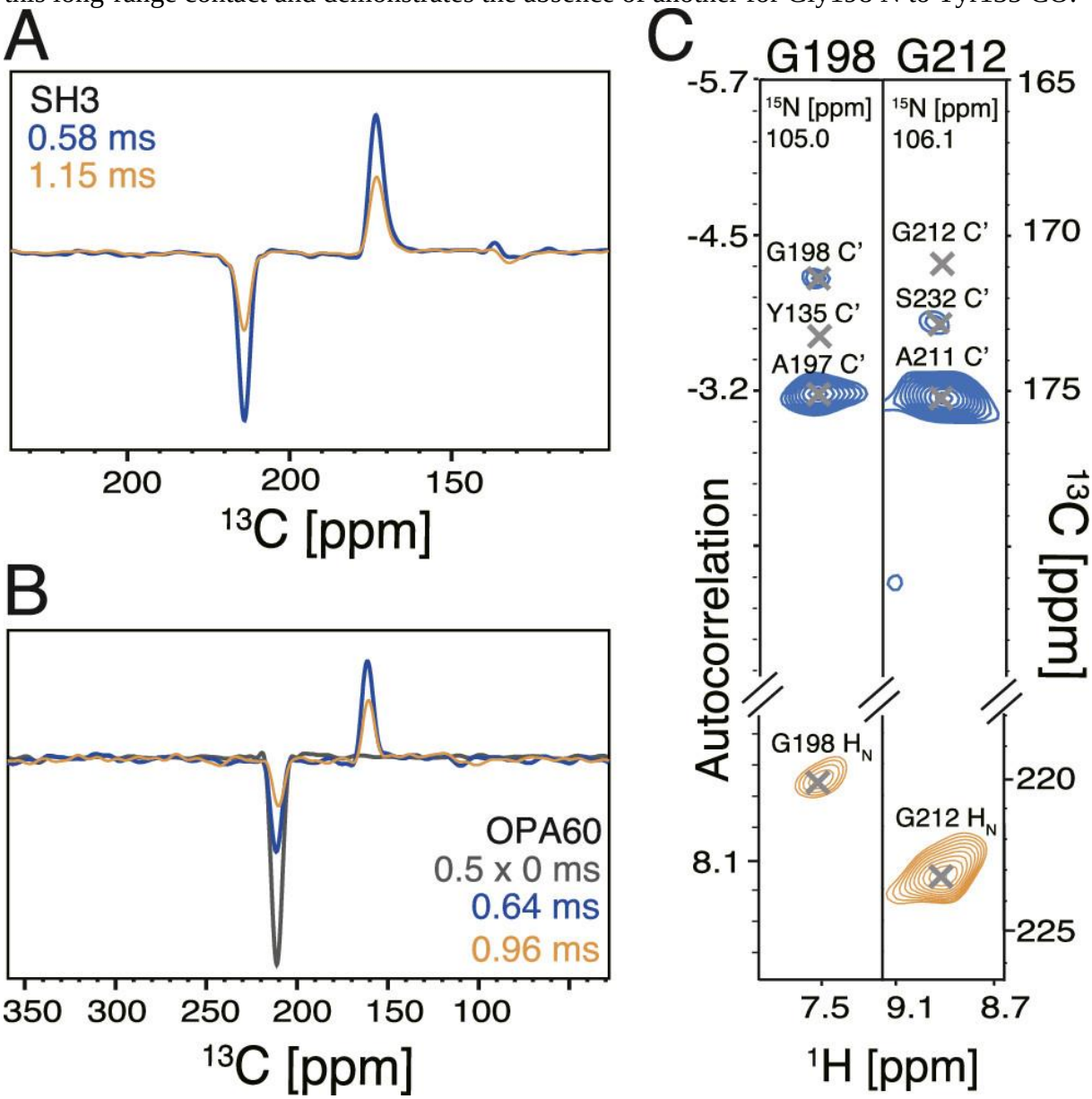

Figure 15: H-CO TREDOR applied to Opa60. **A:** 1D traces demonstrating the coherence decay for SH3. **B:** 1D traces demonstrating the coherence decay for Opa60. **C:** Strips of spectra for Gly198, showing the absence of the long-range contact to Tyr135 while showing the sequential and intra-residue contact, and for Gly212, where the long-range contact to Ser232 can be seen.

5. Discussion

5.1. Opa60

5.1.1. Structure of Opa60

The backbone structure of Opa60 in DMPC lipid bilayers determined herein on a perdeuterated sample using proton-detected solid-state NMR spectroscopy is the fourth example of a β-barrel structure determined by solid-state NMR. Data was recorded at 800 and 600 MHz and 55 kHz MAS. This structure is shown in Figure 5A for the β-barrel embedded in the membrane bilayer and in Panel B, which includes the soluble loops. The β-barrel with the characteristic shear can be clearly identified, as was apparent from the contacts found in the HNhhNH spectrum indicating a typical antiparallel β-sheet structure. The classification whether or not a residue adopts a β-sheet conformation was based on either a "strong" TALOS-N classification or the availability of a hydrogen bond constraint. 91% of assigned residues were thus predicted to be in a β-sheet confirmation, and the backbone RMSD in this region of 2.3 Å indicates a well-converged structure. This is consistent with CP-based spectra highlighting regions of low mobility and furthermore indicates that the loop regions retain their mobility also in the solid-state and are not readily amenable to assignment in CP-based spectra. About 10 residues are left unassigned owing to strong peak overlap or no backbone connections. It seems more likely though that assignment of these would results in further extending the β-sheet, filling in the two missing non-Pro-residues within the assigned sheet (Ala231 and Val195) or completing the short loops connecting the individual sheets (64-66, 126-132, 202/204, 219-224). Based on the chemical shift, at least 3 residues are clearly Thr. Signal overlap or the unavailability of connectivity in a backbone-walk fashion were the reasons for not assigning these peaks. The most promising avenue for reaching a conclusive assignment seems to be residue-specific labeling or reverse labeling. The scrambling when supplying amino acid precursors has been described both for ^{15}N and ^{13}C,[100] and from these insights amino acids for forward labeling can be chosen. Promising candidates are Ala, Ile, Leu, Val and Thr. This approach could yield new assignments, however this is not guaranteed and the samples would require laborious protein expressions for minimal additional insight. Another avenue is to identify residues via contacts, as was done using the HNhhNH spectrum. Orthogonal restraints could come from Hα-mediated contacts as shown on a fully protonated sample at 950 MHz and 100 kHz MAS (see below). The incorporation of Hα atoms into an otherwise deuterated background has been described and termed αPET.[99] Scrambling has also been observed here, but the relative ease

of preparation would present a viable option. Selective introduction while retaining an otherwise deuterated background resulted in increased resolution and thus a suitable approach to assignment. A very simple approach would also be the incubation of refolded or reconstituted Opa60 in deuterated buffer to assess which residues undergo H/D-exchange. This would help in defining the β-barrel region. This has been described earlier for α-helical proteins for determining conformations by water accessibility of residues.[85,175,176]

Spectra of fully protonated Opa60 were recorded on a 950 MHz spectrometer at 100 kHz MAS with the goal of obtaining Hα assignments and subsequently Hα mediated through-space contacts. In total, 65 Hα atoms were assigned, however only five through-space Hα-Hα contacts were found due to sensitivity reasons. These were a confirmation of the structure determined via amide-based contacts and not included in the structure calculation. This shows in principle the feasibility of using fully protonated proteins for structural studies, however this comes with long recording times (18 days for hXhhXH) and scarcity of identified contacts. As mentioned above, the attainment of Hα contacts while avoiding the preparation of an expensive fully deuterated sample could be achieved using the αPET method. In the future, the 950 MHz data could be used to also assign sidechain resonances, starting from the hCCH spectrum.

When compared to the published structure of Opa60 in DPC micelles,[27] the structure in lipid bilayers adopts an extended β-sheet structure. This is particularly visible for strands 4, 5 and 8 and with more assignments it is likely to be confirmed for other strands as well. DMPC has a C_{14} chain, as opposed to DPC with only C_{12}. It is thus likely that this increased hydrophobic length leads to an extension of the β-barrel region. The neisserial native membrane consists of a variety of lipids with chain lengths ranging from C_{14} to C_{18} with the presence of unsaturated species as well as LOS.[29] It is likely that the lipid composition has an influence on the structure of Opa60. To date, no neisserial membrane extract or LOS are commercially available for reconstituting Opa60. For this thesis, DMPC was chosen as it yielded spectra indicative of a properly folded protein. A simple alternative potentially closer to the neisserial native membrane[177] include the *E. coli* total lipid extract which has been used before for structure determination of a β-barrel TM protein.[104] Another approach resulting in a native *E. coli* membrane environment is the usage of outer membrane vesicles (OMVs) from a depletion strain, encompassing deletions of the four major outer membrane proteins and thus making the overexpression of a target protein into these membrane vesicles possible.[64] The amenability to solid-state NMR studies of TM proteins has been shown. However, sensitivity might be of concern and careful optimization of expression conditions would be necessary, especially

regarding the correct delivery of the TM protein to the OMVs with a signal sequence.[178] The interaction of positively charged residues (Arg, Lys) with LOS has been proposed based on their position in the protein.[27] However, a titration of the detergent micelle in this study[27] with LPS revealed no specific interactions.

The assignment strategy for the backbone of the detergent sample resulted in the assignment of 27% of loop resonances and 92% of β-barrel resonances.[27,28] The β-barrel was assigned by cleaving the loops with trypsin, which in principle should be analogous to an H/D-exchange experiment. The loop resonances were assigned by lowering the temperature (and using synthetic peptides) and only retaining the signals from the most flexible loop residues for solution NMR investigation. These feature 18 residues in HV2 (49 total), three in HV1 (24 total) and two in SV (10 total). For solid-state NMR, both raising and lowering the temperature could in principle aid in making loop resonances visible. At lower temperatures, increased rigidity could lead to signals in CP-based spectra and at higher temperatures, the increased flexibility could lead to signals in J-based spectra. However, the latter approach did not yield any differences in J-based hNH spectra (Appendix 7.3.5) and coherence lifetimes were too short to record the J-based hCANH spectra. On the other hand, spectra recorded at lower temperatures and lower spinning to decrease frictional heating also showed no differences or were sensitivity-limited (Appendix 7.3.6). These samples were prepared with 20% glycerol, alike an approach termed as FROSTY-NMR in the literature.[171–173] The technique has been used originally in solution samples for structural investigations of large macromolecular complexes with long correlation times. The combination of glycerol (to increase viscosity) and low temperatures (to increase correlation times) made the recording of MAS-NMR spectra possible for large complexes, but did not improve Opa60 spectra.

Taken together, the results suggest that the loops remain flexible under recording conditions (temperature around 16°C) and that the flexibility exhibits behavior not amenable for the approaches described. Besides the choice of different lipids and lipid-to-protein ratios, the preparation method also influences the sample quality. In this thesis, a dialysis method with cyclodextrin for detergent removal has been chosen. The amount of cyclodextrin, the speed of detergent removal as well as the reconstitution temperature are all parameters which could undergo a more through optimization. This could result in decreased linewidth. Moreover, the orientation of Opa60 in the lipid bilayers could be random. By preparing liposomes, the orientation could be made uniform.

The sample quality can also be discussed in a recent study on the comparison of the spectra of different membrane proteins between different field strengths.[179] The sensitivity and resolution improvement on a newly available 1.2 GHz spectrometer was compared with 950 MHz. For fully protonated Opa60, a decreased improvement when compared to the field ratio in nitrogen linewidth measured in ppm was observed when increasing the field, indicating inhomogeneous contributions to the linewidth. These could result from an inhomogeneous sample preparation. However, the newly charged 1.2 GHz magnet also exhibited non-linear field drift, of which only the linear component could be corrected using a script.[154] For three other proteins (M2, hVDAC1 and CitA), linewidth decrease equal or better than expected was observed. Proton linewidths were generally as expected for a fully protonated protein (150-300 Hz) and scaled accordingly with the field.

This study puts Opa60 in the context of other TM proteins and highlights the importance of sample preparation and the need for a higher field. Moreover, the need for faster spinning was already explained in the introduction (section 2.2.3) and will lead to increased resolution. This will pave the way for the investigation of TM proteins. The need for preparing TM proteins in native-like lipid bilayers or even native membranes was investigated in earlier studies. One study compared the protein OmpX in DPC-micelles with phospholipid-nanodiscs and found an increased length (~2 residues) of the β-barrel in the lipid nanodiscs,[180] much like this thesis suggests for Opa60. Moreover, increased loop dynamics were observed. In the study where the structure of Opa60 was determined in DPC-micelles, a nanodisc preparation also revealed the disappearance of peaks in the spectra when compared to the micellar sample.[27] The β-barrel protein PagP has been investigated in different detergents[181–183] and it has been concluded that loop flexibility is altered depending on the choice of detergent and that this has functional relevance.[59] Clearly, more studies of TM proteins, in particular β-barrel proteins, are needed. The structure of Opa60 is a valuable addition and future studies will bring up new details. The first step towards that will be the preparation of samples facilitating more assignments as detailed above.

5.1.2. Interaction of Opa60 with hCEACAM1-N

The function of Opa60 *in vivo* is the interaction with human CEACAM proteins 1, 3 5 and 6. For this thesis, hCEACAM1-N, with a known structure, was chosen.[35] Only one study made use of a reconstituted Opa60 protein in liposomes made of a mixture of DMPC, DMPG,

cholesterol and DMPE-PEG1000,[30] the latter potentially resembling LOS species present in the neisserial outer membrane. In this thesis, the interaction between Opa60 and hCEACAM1-N was only indicated indirectly in solution NMR in DPC. ^{15}N-HSQC spectra of hCEACAM1-N revealed the appearance of new peaks upon addition of Opa60, which could be indicative of two conformations of the protein in the slow exchange regime.[184] It can be hypothesized that these represent bound and unbound forms. No NMR assignment of hCEACAM1-N is available yet to confirm this hypothesis. This would be the next step and spectral quality suggested the feasibility of this approach. However, residues on hCEACAM1-N implicated in the binding have already been thoroughly investigated.[17,34] Tyr34 and Ile91 (numbering from publication)[30] on the non-glycosylated face of hCEACAM1-N are crucial for any Opa-CEACAM interaction and other residues in spatial proximity are important for specificity towards distinct Opa variants. On the other hand, the interacting residues are not known for Opa60 and are the main reason for investigating this binding. Moreover, a solution NMR assignment of Opa60 is available.[27,28] A solution NMR study of labeled Opa60 bound to hCEACAM1-N has yet to be performed. Firstly, recording conditions will have to be optimized, in particular regarding sample temperature. Temperature for structure determination was varied to specifically observe barrel or loop resonances, with the latter observed at lower temperatures.[27,28] In the solid-state sample of Opa60, the interaction with hCEACAM1-N was assessed using a pulldown assay. The prepared lipid bilayers were prepared like the NMR samples but afterwards sonicated as described to homogenize liposome size. No interaction was observed in this assay. The reason for this remains unclear and a reproduction of conditions which were described in the publication[30] is pending to narrow down what exactly is necessary for a successful interaction. The sonication procedure was reported to result in liposomes with mostly outward-facing Opa proteins which were amenable to an interaction. Refolding of the urea-solubilized protein was not conducted by dilution into the detergent DPC but rather in a borate buffer containing 4 M urea and the short chain lipid diC_{10}PC. However, without further systematic experiments it is not possible to draw conclusions on the influence of buffer, pH or refolding pathway yet. The absence of any interaction at all also raises the question whether the recombinantly produced proteins have the correct sequence.

Protein-protein interactions in solid-state NMR have been described yet are still underrepresented as topics. Protocols for individual proteins and their multimeric assemblies have been published.[185] Techniques for studying protein-protein interactions have been summarized[186] and include CSPs and solvent-paramagnetic relaxation enhancement (PRE) for

delineating the binding surfaces as well as usage of the Nuclear Overhauser Effect (NOE) and Residual Dipolar Couplings (RDCs) for structural information.

Opa60, and the Opa proteins in general, are only one example of proteins from pathogens exploiting the hCEACAM-proteins as an entry pathway into human hosts. The protein HopQ from *Helicobacter pylori* binds to the same non-glycosylated surface of the hCEACAM-proteins via van-der-Waals interactions and hydrogen bonds.[187] HopQ binds to hCEACAM via four loops, which are shorter than Opa60's HV loops (10-25 residues versus 43 (HV1) or 49 (HV2) residues (Figure 5)). Two loops of HopQ are unfolded in the non-bound state and undergo folding upon binding. The protein UspA1 from *Moraxella catarrhalis* employs a trimeric coiled-coil domain to bind to hCEACAM,[188] and the Dr-adhesins of *E. coli* exploit the same surface of the hCEACAM proteins.[189] P1 from *Haemophilus influenzae* employs the hCEACAM proteins as receptors, but no structural information is available to date.[190] Intriguingly, the HV2 region of a meningococcal Opa variant shares the sequence motif GxI/V/LxQ with some but not all P1 variants of *H. influenzae*.[19] It was hypothesized that due to this, the sequence motif is not necessary for receptor binding. Moreover, it is found in only about 50% of *N. gonorrhoeae* strains.

This puts Opa60 into a larger context of proteins and pathogens that all have evolved to exploit the human CEACAM proteins for cell adhesion and entry. All of these proteins need to disrupt the native CEACAM-CEACAM interactions, and in particular, HopQ has been shown to disrupt the *trans* dimerization of hCEACAMs.[191] CEACAM-CEACAM interactions were shown to be in the low micromolar range and thus, all pathogens need a means of outcompeting this high affinity interaction. For Opa60, it has been shown in reconstituted systems that the interaction is in the low nanomolar range and this would enable efficient binding.[30] HopQ selectively recognizes monomers of CEACAM and thus would be able to shift the equilibrium,[187,191] and for the Dr-adhesins, it has been hypothesized that efficient receptor engagement is achieved by a high local concentration of adhesins present on the bacterial surface.[188]

5.1.3. Opa60 in different lipids

Opa60 was studied in different lipid species, resembling the outer membrane of *N. gonorrhoeae*. Rd2 LPS from *E. coli* strain F583 represents a heterogenous LPS species, as opposed to Rd2 LPS from strain F583.[147] Kdo2-lipid A (KLA) contains only the core region

of LPS/LOS, and is thus closer to the structure of the shorter LOS species found in the native outer membrane. Judging based on hCANH spectra of Opa60 in these lipids, no structural rearrangement took place in these lipids. The origin of two CSPs apparent in the projection in Figure 9 on residues Leu118 and Ser232 remain unclear, since both residues are buried in the β-barrel and are not prone to interaction with LPS. In the solution study, no interaction with LPS was found by titration, however hypothesized because of the presence of negatively charged residues outside the membrane.[27] Taken together with the fact that the only reconstituted study employed DMPE-PEG1000, which might result in a steric restraint of Opa60 loops, it seems plausible that the membrane composition plays a role in enabling interaction with hCEACAM. However, no binding could be reproduced in this thesis.

5.1.4. Conclusion

In this thesis, the structure of the β-barrel of Opa60 has been determined in DMPC lipid bilayers with proton-detected MAS solid-state NMR. In comparison with the structure in detergents, the β-barrel takes an extended shape. Future assignments will likely confirm this, and can be extended to also include sidechain resonances available from a fully protonated sample. The loops retained their dynamic behavior and were not spectroscopically observed. A possible interaction with hCEACAM1-N was only seen in solution NMR with Opa60 in detergent, but not in a reconstituted system. A systematic approach to this interaction is needed, and will put Opa60 in line with other pathogen proteins binding to the same surface on the human CEACAM receptors. The investigation of Opa60 in two different LPS variants and KLA did not show any obvious structural changes as observed in NMR spectra. The interaction with LOS, as might be expected from the omnipresence of these in the neisserial outer membrane, could not be easily observed.

Opa60 is part of the large family of TM proteins and a valuable addition to the few existing β-barrel proteins solved by solid-state NMR. Solid-state NMR holds a huge potential in the structure determination of (both α-helical and β-barrel) TM proteins, as evidenced by the recent structural studies on the disease-relevant SARS-CoV2 Envelope protein and Influenza A's M2 protein.

5.2. TREDOR

5.2.1. Characterization of TREDOR fitting

TREDOR was introduced as a new method for accurate distance determination for solid samples.[134] The pulse sequence is based on the 3D zf-TEDOR[126] and frequency-selective REDOR (FSR)[128] experiments. The major difference is that in TREDOR, the chemical shifts of the non-transferred (the REDOR signal) and the transferred (the TEDOR signal) are co-acquired. This allowed the formulation of the TREDOR parameter ζ as the ratio of transferred and total signal. The evolution time ratio needs to be chosen according to the gyromagnetic ratios of the corresponding nuclei and is 2.48 for the co-evolution of ^{13}C and ^{15}N. Other major differences to zf-TEDOR are the removal of the first z-filter to render TREDOR compatible with co-evolution of shifts and the first transfer being a CP-transfer to ^{15}N rather than ^{13}C, allowing the removal of the z-filter, which in zf-TEDOR was used to remove homonuclear J couplings between nitrogen atoms. These are negligible in protein samples. Lastly, TREDOR is designed as a proton detected sequence to improve sensitivity. Moreover, this allows the encoding of the proton chemical shift as an additional spectral dimension.

The formulation of the TREDOR parameter ζ as given in Equation (35) accomplishes the removal of two fit parameters when compared with conventional TEDOR. These are the coherence decay rate Γ and the TEDOR amplitude scaling factor V. This leaves the dipolar coupling as the sole fitting parameter in the analytical Bessel Equation (36). The fitting procedure thus became much more stable. When compared to TEDOR, TREDOR generated reliable fittings for short mixing times even with only one or two points. This underpins the advantage of TREDOR over TEDOR, where in the latter the fitting is not possible only in the buildup regime of the dipolar oscillation curve and requires the tracking of a full oscillation with more data points. This can also be seen when comparing the fitting accuracy in between TREDOR and TEDOR with the distances obtained from the SH3 crystal structure (Figure 12). Here, the R^2 correlation coefficient was 0.82 for TREDOR and only 0.30 for TEDOR data.

The emergence of a detectable three-spin term was described and the term is given in Equation (32). This term led to artifacts in the spectrum, however the exact place could be influenced by appropriate offset placement. The buildup of these terms was simulated and shown to be negligible for short mixing times. A spectrum with visible artifacts and a comparison of different ^{13}C offsets is shown in Appendix 7.5.4.

The TREDOR fitting procedure was calibrated with the one-bond distance N-Cα of Gly51 in the microcrystalline model protein SH3. The fitting procedure resulted in a dipolar coupling of 810 Hz, as compared to the expected value 1,005 Hz for a 1.45 Å distance. This corresponds to a TREDOR scaling factor of 0.8. Scaling can be a result of radiofrequency field inhomogeneity[132,192] or finite pulse effects,[193] the latter of which was shown to be 0.93 under the experimental conditions described. The remaining factor of approximately 0.86 could further be explained by the presence of molecular motions[194–196] which result in a downscaling of the actual dipolar coupling strength, reflected in the order parameter of the protein backbone.[197–200]

5.2.2. Coherence decay under TREDOR

Intriguingly, TREDOR also yielded accurate distance restraints when only using two or even one mixing time point instead of 3 for N-Cx TREDOR. Mixing times were 4, 6 and 10 ms. All two-point fits performed well, and for one-point fits, the 6 ms point generated the most accurate fits. This yielded the question whether there is an ideal mixing time for a TREDOR experiment from which accurate distances could be derived. The ideal mixing time needs to account for two factors, namely the coherence decay rate as well as the buildup of the signal. These are opposing factors and led to the derivation of the formula:

$$\frac{S}{N_{1i}(t_{mix})} = e^{-\Gamma_i t_{mix}} \frac{V_{1i}(t_{mix})}{V_1(t_{mix}) + V_{1i}(t_{mix})} \frac{1}{\sqrt{\frac{V_1(t_{mix})^2 + V_{1i}(t_{mix})^2}{(V_1(t_{mix}) + V_{1i}(t_{mix}))^2}\sigma^2}} \quad (37)$$

The choice of mixing time thus becomes an optimization problem and is best determined empirically or with simulations. Simulations performed in the scope of the publication placed the ideal mixing time at 8 ms with a backbone-nitrogen transverse coherence decay rate of 10 ms (as found for the TM protein M2)[201] and a coupling strength of 132 Hz typical of an N-Cβ coupling. The experimental result that the 6 ms data point resulted in the most accurate fittings can be explained by the fact that in practice, large couplings with a fast buildup will only be captured accurately when the point lies in the buildup phase of the curve and not close to the maximum. The effect of passive couplings has been shown in simulations to be small and large passive couplings will result in smaller measured active couplings.

The coherence decay rate of individual signals under TREDOR was determined and compared to the rate in an hNH experiment. Surprisingly, the rate under TREDOR is much higher than in

the reference experiment. Most likely, additional relaxation was caused by the emergence of multiple quantum terms created during the REDOR periods. Here, rf field inhomogeneity is a major contributor, however the exact description depends on many factors including external and internal spin interactions, which were not further investigated. The used XY-8 phase cycling alleviated these effects.[152] Of high relevance is the fact that a single exponential decay rate resulted in good fits for all residues. This implies that one relaxation process is dominant over all other processes, and this assumption also forms the basis for formulating Equation (37). $T_2\rho$ effects alone were not sufficient to explain the overall relaxation rate as $T_2\rho$ times measured under realistic spinlock field strengths as present during REDOR periods was longer than T_2 times.[134]

5.2.3. SH3 structure calculation with TREDOR

The SH3 structure determined with TREDOR data alone (and TALOS-N derived torsion angle restraints from the assignment) already converged well with an backbone RMSD of 1.8 Å. This clearly validates TREDOR as a method for the attainment of valuable structural restraints in a simple and fast manner. The determined structure also holds up well when compared to the reference crystal structure with a backbone RMSD of 2.1 Å. TREDOR contacts found in the H-CO spectrum between backbone amide protons and sidechain carbon atoms increased the accuracy of the structure further, especially in the loop regions of SH3 (Figure 14C). TREDOR thus not only provided data on the overall fold, but also data on local geometries via torsion angle confinement.

5.2.4. TREDOR applied to Opa60

H-CO TREDOR was applied to the TM protein Opa60 as a challenging target. Fully protonated Opa60, spinning at 100 kHz MAS in a 1.2 GHz magnet, showed a proton T_2 time of only 2.5 ms and thus resembles many other TM proteins. However, the decay of signals under TREDOR was comparable to that of SH3 residues and thus, TREDOR could be applied successfully. A drawback of TREDOR when dealing with comparatively large TM proteins is the overlap of signals, which was also observed for Opa60 and posed difficulties in finding isolated signals amenable to assignment. Only for one residue, Gly212, a long-range contact to Ser232 was

found as expected in the β-barrel fold of Opa60. Potentially, TREDOR can be extended to further dimensions to resolve these issue in larger proteins.

5.2.5. Conclusion

TREDOR has the potential to not only play a major role in protein structure determination, but also in the application of small molecules and material science samples. The combination of REDOR and TEDOR signals leaves TREDOR with only one fit parameter, the dipolar coupling and thus the internuclear distance. It is more accurate than previously described procedures and can in principle be applied with only one mixing time which can be determined. This was demonstrated with the structure determination of SH3. The application of TREDOR to challenging systems such as the TM protein Opa60 will also profit from the development of higher field magnets and faster spinning probes.

6. References

[1] J. M. Berg, J. L. Tymoczko, L. Stryer, *Biochemistry*, New York: WH Freeman, **2002**.

[2] L. Tiefenauer, S. Demarche, *Materials* **2012**, *5*, 2205–2242.

[3] J. P. Overington, B. Al-Lazikani, A. L. Hopkins, *Nat. Rev. Drug Discov.* **2006**, *5*, 10.

[4] B. K. Ho, P. M. G. Curmi, *J. Mol. Biol.* **2002**, *317*, 291–308.

[5] T. O. C. Kwan, D. Axford, I. Moraes, *Biochem. Soc. Trans.* **2020**, *48*, 2505–2524.

[6] Y. Cheng, *Curr. Opin. Struct. Biol.* **2018**, *52*, 58–63.

[7] X. Yao, X. Fan, N. Yan, *Proc. Natl. Acad. Sci. U. S. A.* **2020**, *117*, 18497–18503.

[8] T. Schubeis, T. Le Marchand, L. B. Andreas, G. Pintacuda, *J. Magn. Reson.* **2018**, *287*, 140–152.

[9] V. S. Mandala, J. K. Williams, M. Hong, *Annu. Rev. Biophys.* **2018**, *47*, 201–222.

[10] M. S. Almén, K. J. V. Nordström, R. Fredriksson, H. B. Schiöth, *BMC Biol.* **2009**, *7*, 50.

[11] K. S. Bhat, C. P. Gibbs, O. Barrera, S. G. Morrison, F. Jähnig, A. Stem, E. -M Kupsch, T. F. Meyer, J. Swanson, *Mol. Microbiol.* **1992**, *6*, 1073–1076.

[12] M. M. Hobbs, A. Seiler, M. Achtman, J. G. Cannon, *Mol. Microbiol.* **1994**, *12*, 171–180.

[13] B. Malorny, G. Morelli, B. Kusecek, J. Kolberg, M. Achtman, *J. Bacteriol.* **1998**, *180*, 1323–1330.

[14] B. D. Robertson, T. F. Meyer, *Trends Genet.* **1992**, *8*, 422–427.

[15] C. R. Hauck, T. F. Meyer, *Curr. Opin. Microbiol.* **2003**, *6*, 43–49.

[16] M. P. Bos, D. Kao, D. M. Hogan, C. C. R. Grant, R. J. Belland, *Infect. Immun.* **2002**, *70*, 1715–1723.

[17] M. Virji, D. Evans, A. Hadfield, F. Grunert, A. M. Telxeira, S. M. Watt, *Mol. Microbiol.* **1999**, *34*, 538–551.

[18] C. C. R. Grant, M. P. Bos, R. J. Belland, *Mol. Microbiol.* **1999**, *32*, 233–242.

[19] M. I. De Jonge, H. J. Hamstra, L. Van Alphen, J. Dankert, P. Van Der Ley, *Mol.*

Microbiol. **2003**, *50*, 1005–1015.

[20] J. P. M. Van Putten, S. M. Paul, *EMBO J.* **1995**, *14*, 2144–2154.

[21] T. Chen, R. J. BeUand, J. Wilson, J. Swanson, *J. Exp. Med.* **1995**, *182*, 511–517.

[22] S. D. Gray-Owen, C. Dehio, A. Haude, F. Grunert, T. F. Meyer, *EMBO J.* **1997**, *16*, 3435–3445.

[23] M. Virji, K. Makepeace, D. J. P. Ferguson, S. M. Watt, *Mol. Microbiol.* **1996**, *22*, 941–950.

[24] T. Chen, E. C. Gotschlich, *Proc. Natl. Acad. Sci. U. S. A.* **1996**, *93*, 14851–14856.

[25] T. Chen, F. Grunert, A. Medina-Marino, E. C. Gotschlich, *J. Exp. Med.* **1997**, *185*, 1557–1564.

[26] M. P. Bos, F. Grunert, R. J. Belland, *Infect. Immun.* **1997**, *65*, 2353–2361.

[27] D. A. Fox, P. Larsson, R. H. Lo, B. M. Kroncke, P. M. Kasson, L. Columbus, *J. Am. Chem. Soc.* **2014**, *136*, 9938–9946.

[28] D. A. Fox, L. Columbus, *Protein Sci.* **2013**, *22*, 1133–1140.

[29] M. M. Rahman, V. S. K. Kolli, C. M. Kahler, G. Shih, D. S. Stephens, R. W. Carlson, *Microbiology* **2000**, *146*, 1901–1911.

[30] J. N. Martin, L. M. Ball, T. L. Solomon, A. H. Dewald, A. K. Criss, L. Columbus, *Biochemistry* **2016**, *55*, 4286–4294.

[31] L. M. Werner, A. Palmer, A. Smirnov, M. Belcher Dufrisne, L. Columbus, A. K. Criss, *Cytom. Part A* **2020**, *97*, 1081–1089.

[32] M. Sadarangani, A. J. Pollard, S. D. Gray-Owen, *FEMS Microbiol. Rev.* **2011**, *35*, 498–514.

[33] S. Hammarström, *Semin. Cancer Biol.* **1999**, *9*, 67–81.

[34] A. Popp, C. Dehio, F. Grunert, T. F. Meyer, S. D. Gray-Owen, *Cell. Microbiol.* **1999**, *1*, 169–181.

[35] A. Fedarovich, J. Tomberg, R. A. Nicholas, C. Davies, *Acta Crystallogr. Sect. D Biol.*

Crystallogr. **2006**, *62*, 971–979.

[36] J. Keeler, *Understanding NMR Spectroscopy*, John Wiley & Sons, **2011**.

[37] M. H. Levitt, *Spin Dynamics: Basics of Nuclear Magnetic Resonance*, John Wiley & Sons, **2013**.

[38] J. Cavanagh, W. J. Fairbrother, A. G. Palmer III, N. J. Skelton, *Protein NMR Spectroscopy: Principles and Practice*, Elsevier, **1995**.

[39] P. J. Hore, *Nuclear Magnetic Resonance*, Oxford University Press, USA, **2015**.

[40] P. J. Hore, J. A. Jones, S. Wimperis, *NMR: The Toolkit: How Pulse Sequences Work*, Oxford University Press, USA, **2015**.

[41] M. J. Duer, *Introduction to Solid-State NMR Spectroscopy*, Blackwell Oxford, **2004**.

[42] D. D. Laws, H.-M. L. Bitter, A. Jerschow, *Angew. Chem. Int. Ed. Engl.* **2002**, *41*, 3096–3129.

[43] C. Leroy, D. L. Bryce, *Prog. Nucl. Magn. Reson. Spectrosc.* **2018**, *109*, 160–199.

[44] B. Reif, S. E. Ashbrook, L. Emsley, M. Hong, *Nat. Rev. Methods Prim.* **2021**, *1*, DOI 10.1038/s43586-020-00002-1.

[45] E. R. Andrew, A. Bradbury, R. G. Eades, **1958**, *162*, 4650.

[46] I. J. Lowe, *Phys. Rev. Lett.* **1959**, *2*, 285–287.

[47] J. Struppe, C. M. Quinn, M. Lu, M. Wang, G. Hou, X. Lu, J. Kraus, L. B. Andreas, J. Stanek, D. Lalli, A. Lesage, G. Pintacuda, W. Maas, A. M. Gronenborn, T. Polenova, *Solid State Nucl. Magn. Reson.* **2017**, *87*, 117–125.

[48] A. Böckmann, M. Ernst, B. H. Meier, *J. Magn. Reson.* **2015**, *253*, 71–79.

[49] M. Schledorn, A. A. Malär, A. Torosyan, S. Penzel, D. Klose, A. Oss, M. L. Org, S. Wang, L. Lecoq, R. Cadalbert, A. Samoson, A. Böckmann, B. H. Meier, *ChemBioChem* **2020**, *21*, 2540–2548.

[50] M. Leskes, P. K. Madhu, S. Vega, *Prog. Nucl. Magn. Reson. Spectrosc.* **2010**, *57*, 345–380.

[51] S. Penzel, A. A. Smith, V. Agarwal, A. Hunkeler, M. L. Org, A. Samoson, A. Böckmann, M. Ernst, B. H. Meier, *J. Biomol. NMR* **2015**, *63*, 165–186.

[52] O. C. Andronesi, S. Becker, K. Seidel, H. Heise, H. S. Young, M. Baldus, *J. Am. Chem. Soc.* **2005**, *127*, 12965–12974.

[53] F. Azadi-Chegeni, M. E. Ward, G. Perin, D. Simionato, T. Morosinotto, M. Baldus, A. Pandit, *Biophys. J.* **2021**, *120*, 270–283.

[54] G. Metz, X. Wu, S. O. Smith, *J. Magn. Reson. Ser. A* **1994**, *110*, 219–227.

[55] P. Schanda, M. Ernst, *Prog. Nucl. Magn. Reson. Spectrosc.* **2016**, *96*, 1–46.

[56] I. Matlahov, P. C. A. van der Wel, *Methods* **2018**, *148*, 123–135.

[57] A. Krushelnitsky, D. Reichert, K. Saalwächter, *Acc. Chem. Res.* **2013**, *46*, 2028–2036.

[58] J. R. Lewandowski, *Acc. Chem. Res.* **2013**, *46*, 2018–2027.

[59] C. Chipot, F. Dehez, J. R. Schnell, N. Zitzmann, E. Pebay-Peyroula, L. J. Catoire, B. Miroux, E. R. S. Kunji, G. Veglia, T. A. Cross, P. Schanda, *Chem. Rev.* **2018**, *118*, 3559–3607.

[60] H. X. Zhou, T. A. Cross, *Annu. Rev. Biophys.* **2013**, *42*, 361–392.

[61] R. Fu, X. Wang, C. Li, A. N. Santiago-Miranda, G. J. Pielak, F. Tian, *J. Am. Chem. Soc.* **2011**, *133*, 12370–12373.

[62] S. A. Shahid, M. Nagaraj, N. Chauhan, T. W. Franks, B. Bardiaux, M. Habeck, M. Orwick-Rydmark, D. Linke, B. J. Van Rossum, *Angew. Chemie - Int. Ed.* **2015**, *54*, 12602–12606.

[63] L. A. Baker, M. Daniëls, E. A. W. Van Der Cruijsen, G. E. Folkers, M. Baldus, *J. Biomol. NMR* **2015**, *62*, 199–208.

[64] J. Thoma, B. M. Burmann, *Biochemistry* **2020**, *59*, 1656–1660.

[65] M. Renault, R. Tommassen-Van Boxtel, M. P. Bos, J. A. Post, J. Tommassen, M. Baldus, *Proc. Natl. Acad. Sci. U. S. A.* **2012**, *109*, 4863–4868.

[66] P. Selenko, *Int. J. Mol. Sci.* **2019**, *20*, DOI 10.3390/ijms20061278.

[67] D. Lacabanne, M. L. Fogeron, T. Wiegand, R. Cadalbert, B. H. Meier, A. Böckmann, *Prog. Nucl. Magn. Reson. Spectrosc.* **2019**, *110*, 20–33.

[68] E. E. Najbauer, K. T. Movellan, T. Schubeis, T. Schwarzer, K. Castiglione, K. Giller, G. Pintacuda, S. Becker, L. B. Andreas, *ChemPhysChem* **2019**, *20*, 302–310.

[69] P. Fricke, V. Chevelkov, M. Zinke, K. Giller, S. Becker, A. Lange, *Nat. Protoc.* **2017**, *12*, 764–782.

[70] V. A. Higman, *Prog. Nucl. Magn. Reson. Spectrosc.* **2018**, *106–107*, 37–65.

[71] E. Barbet-Massin, A. J. Pell, J. S. Retel, L. B. Andreas, K. Jaudzems, W. T. Franks, A. J. Nieuwkoop, M. Hiller, V. Higman, P. Guerry, A. Bertarello, M. J. Knight, M. Felletti, T. Le Marchand, S. Kotelovica, I. Akopjana, K. Tars, M. Stoppini, V. Bellotti, M. Bolognesi, S. Ricagno, J. J. Chou, R. G. Griffin, H. Oschkinat, A. Lesage, L. Emsley, T. Herrmann, G. Pintacuda, *J. Am. Chem. Soc.* **2014**, *136*, 12489–12497.

[72] M. J. Knight, A. L. Webber, A. J. Pell, P. Guerry, E. Barbet-Massin, I. Bertini, I. C. Felli, L. Gonnelli, R. Pierattelli, L. Emsley, A. Lesage, T. Herrmann, G. Pintacuda, *Angew. Chemie - Int. Ed.* **2011**, *50*, 11697–11701.

[73] E. Barbet-Massin, A. J. Pell, K. Jaudzems, W. T. Franks, J. S. Retel, S. Kotelovica, I. Akopjana, K. Tars, L. Emsley, H. Oschkinat, A. Lesage, G. Pintacuda, *J. Biomol. NMR* **2013**, *56*, 379–386.

[74] L. B. Andreas, J. Stanek, T. Le Marchand, A. Bertarello, D. Cala-De Paepe, D. Lalli, M. Krejčíková, C. Doyen, C. Öster, B. Knott, S. Wegner, F. Engelke, I. C. Felli, R. Pierattelli, N. E. Dixon, L. Emsley, T. Herrmann, G. Pintacuda, *J. Biomol. NMR* **2015**, *62*, 253–261.

[75] L. B. Andreas, T. Le Marchand, K. Jaudzems, G. Pintacuda, *J. Magn. Reson.* **2015**, *253*, 36–49.

[76] J. Stanek, L. B. Andreas, K. Jaudzems, D. Cala, D. Lalli, A. Bertarello, T. Schubeis, I. Akopjana, S. Kotelovica, K. Tars, A. Pica, S. Leone, D. Picone, Z. Q. Xu, N. E. Dixon, D. Martinez, M. Berbon, N. El Mammeri, A. Noubhani, S. Saupe, B. Habenstein, A. Loquet, G. Pintacuda, *Angew. Chemie - Int. Ed.* **2016**, *55*, 15504–15509.

[77] L. B. Andreas, K. Jaudzems, J. Stanek, D. Lalli, A. Bertarelloa, T. Le Marchand, D. C.

De Paepe, S. Kotelovica, I. Akopjana, B. Knott, S. Wegner, F. Engelke, A. Lesage, L. Emsley, K. Tars, T. Herrmann, G. Pintacuda, *Proc. Natl. Acad. Sci. U. S. A.* **2016**, *113*, 9187–9192.

[78] D. H. Zhou, G. Shah, M. Cormos, C. Mullen, D. Sandoz, C. M. Rienstra, *J. Am. Chem. Soc.* **2007**, *129*, 11791–11801.

[79] A. Marchetti, S. Jehle, M. Felletti, M. J. Knight, Y. Wang, Z. Q. Xu, A. Y. Park, G. Otting, A. Lesage, L. Emsley, N. E. Dixon, G. Pintacuda, *Angew. Chemie - Int. Ed.* **2012**, *51*, 10756–10759.

[80] S. K. Vasa, P. Rovó, K. Giller, S. Becker, R. Linser, *Phys. Chem. Chem. Phys.* **2016**, *18*, 8359–8363.

[81] D. M. Lemaster, *Q. Rev. Biophys.* **1990**, *23*, 133–174.

[82] B. Reif, C. P. Jaroniec, C. M. Rienstra, M. Hohwy, R. G. Griffin, *J. Magn. Reson.* **2001**, *151*, 320–327.

[83] B. Reif, R. G. Griffin, *J. Magn. Reson.* **2003**, *160*, 78–83.

[84] J. Medeiros-Silva, D. Mance, M. Daniëls, S. Jekhmane, K. Houben, M. Baldus, M. Weingarth, *Angew. Chemie - Int. Ed.* **2016**, *55*, 13606–13610.

[85] M. E. Ward, L. Shi, E. Lake, S. Krishnamurthy, H. Hutchins, L. S. Brown, V. Ladizhansky, *J. Am. Chem. Soc.* **2011**, *133*, 17434–17443.

[86] Ü. Akbey, S. Lange, W. Trent Franks, R. Linser, K. Rehbein, A. Diehl, B. J. Van Rossum, B. Reif, H. Oschkinat, *J. Biomol. NMR* **2010**, *46*, 67–73.

[87] D. H. Zhou, D. T. Graesser, W. T. Franks, C. M. Rienstra, *J. Magn. Reson.* **2006**, *178*, 297–307.

[88] S. Asami, P. Schmieder, B. Reif, *J. Am. Chem. Soc.* **2010**, *132*, 15133–15135.

[89] S. Asami, K. Szekely, P. Schanda, B. H. Meier, B. Reif, *J. Biomol. NMR* **2012**, *54*, 155–168.

[90] D. Mance, T. Sinnige, M. Kaplan, S. Narasimhan, M. Daniëls, K. Houben, M. Baldus, M. Weingarth, *Angew. Chemie - Int. Ed.* **2015**, *54*, 15799–15803.

[91] K. H. Gardner, M. K. Rosen, L. E. Kay, *Biochemistry* **1997**, *36*, 1389–1401.

[92] N. K. Goto, K. H. Gardner, G. A. Mueller, R. C. Willis, L. E. Kay, *J. Biomol. NMR* **1999**, *13*, 369–374.

[93] P. Gans, O. Hamelin, R. Sounier, I. Ayala, M. A. Durá, C. D. Amero, M. Noirclerc-Savoye, B. Franzetti, M. J. Plevin, J. Boisbouvier, *Angew. Chemie - Int. Ed.* **2010**, *49*, 1958–1962.

[94] V. Kurauskas, E. Crublet, P. Macek, R. Kerfah, D. F. Gauto, J. Boisbouvier, P. Schanda, *Chem. Commun.* **2016**, *52*, 9558–9561.

[95] R. Linser, B. Bardiaux, V. Higman, U. Fink, B. Reif, *J. Am. Chem. Soc.* **2011**, *133*, 5905–5912.

[96] M. Huber, S. Hiller, P. Schanda, M. Ernst, A. Böckmann, R. Verel, B. H. Meier, *ChemPhysChem* **2011**, *12*, 915–918.

[97] M. Kainosho, T. Torizawa, Y. Iwashita, T. Terauchi, A. Mei Ono, P. Güntert, *Nature* **2006**, *440*, 52–57.

[98] T. Sinnige, M. Daniëls, M. Baldus, M. Weingarth, *J. Am. Chem. Soc.* **2014**, *136*, 4452–4455.

[99] K. T. Movellan, E. E. Najbauer, S. Pratihar, M. Salvi, K. Giller, S. Becker, L. B. Andreas, *J. Biomol. NMR* **2019**, *73*, 81–91.

[100] D. Lacabanne, B. H. Meier, A. Böckmann, *J. Biomol. NMR* **2018**, *71*, 141–150.

[101] J. R. Lewandowski, J. N. Dumez, Ü. Akbey, S. Lange, L. Emsley, H. Oschkinat, *J. Phys. Chem. Lett.* **2011**, *2*, 2205–2211.

[102] T. Schubeis, T. Le Marchand, C. Daday, W. Kopec, K. T. Movellan, J. Stanek, T. S. Schwarzer, K. Castiglione, B. L. de Groot, G. Pintacuda, L. B. Andreas, *Proc. Natl. Acad. Sci. U. S. A.* **2020**, *117*, 21014–21021.

[103] T. Schubeis, T. S. Schwarzer, T. Le Marchand, J. Stanek, K. T. Movellan, K. Castiglione, G. Pintacuda, L. B. Andreas, *Biomol. NMR Assign.* **2020**, *14*, 295–300.

[104] J. S. Retel, A. J. Nieuwkoop, M. Hiller, V. A. Higman, E. Barbet-Massin, J. Stanek, L. B. Andreas, W. T. Franks, B. J. Van Rossum, K. R. Vinothkumar, L. Handel, G. G. De

Palma, B. Bardiaux, G. Pintacuda, L. Emsley, W. Kühlbrandt, H. Oschkinat, *Nat. Commun.* **2017**, *8*, DOI 10.1038/s41467-017-02228-2.

[105] S. A. Shahid, B. Bardiaux, W. T. Franks, L. Krabben, M. Habeck, B. J. Van Rossum, D. Linke, *Nat. Methods* **2012**, *9*, 1212–1217.

[106] S. H. Park, B. B. Das, F. Casagrande, Y. Tian, H. J. Nothnagel, M. Chu, H. Kiefer, K. Maier, A. A. De Angelis, F. M. Marassi, S. J. Opella, *Nature* **2012**, *491*, 779–783.

[107] S. J. Opella, *Annu. Rev. Anal. Chem.* **2013**, *6*, 305–328.

[108] S. Wang, R. A. Munro, L. Shi, I. Kawamura, T. Okitsu, A. Wada, S. Y. Kim, K. H. Jung, L. S. Brown, V. Ladizhansky, *Nat. Methods* **2013**, *10*, 1007–1012.

[109] S. Milikisiyants, S. Wang, R. A. Munro, M. Donohue, M. E. Ward, D. Bolton, L. S. Brown, T. I. Smirnova, V. Ladizhansky, A. I. Smirnov, *J. Mol. Biol.* **2017**, *429*, 1903–1920.

[110] G. Jeschke, *Annu. Rev. Phys. Chem.* **2012**, *63*, 419–446.

[111] V. S. Mandala, M. J. McKay, A. A. Shcherbakov, A. J. Dregni, A. Kolocouris, M. Hong, *Nat. Struct. Mol. Biol.* **2020**, *27*, 1202–1208.

[112] M. Sharma, M. Yi, H. Dong, H. Qin, E. Peterson, D. D. Busath, H. X. Zhou, T. A. Cross, *Science* **2010**, *330*, 509–512.

[113] S. D. Cady, K. Schmidt-Rohr, J. Wang, C. S. Soto, W. F. Degrado, M. Hong, *Nature* **2010**, *463*, 689–692.

[114] L. B. Andreas, M. Reese, M. T. Eddy, V. Gelev, Q. Z. Ni, E. A. Miller, L. Emsley, G. Pintacuda, J. J. Chou, R. G. Griffin, *J. Am. Chem. Soc.* **2015**, *137*, 14877–14886.

[115] K. T. Movellan, M. Wegstroth, K. Overkamp, A. Leonov, S. Becker, L. B. Andreas, *J. Am. Chem. Soc.* **2020**, *142*, 2704–2708.

[116] A. E. Bennett, J. H. Ok, R. G. Griffin, S. Vega, *J. Chem. Phys.* **1992**, *96*, 8624–8627.

[117] K. Takegoshi, S. Nakamura, T. Terao, *Chem. Phys. Lett.* **2001**, *344*, 631–637.

[118] R. Verel, M. Ernst, B. H. Meier, *J. Magn. Reson.* **2001**, *150*, 81–99.

[119] K. Grohe, E. Nimerovsky, H. Singh, S. K. Vasa, B. Söldner, B. Vögeli, C. M. Rienstra,

R. Linser, *Chem. Commun.* **2019**, *55*, 7899–7902.

[120] B. Vögeli, J. Orts, D. Strotz, P. Güntert, R. Riek, *Chimia (Aarau).* **2012**, *66*, 787–790.

[121] B. Vögeli, S. Olsson, P. Güntert, R. Riek, *Biophys. J.* **2016**, *110*, 113–126.

[122] T. Gullion, J. Schaefer, *J. Magn. Reson.* **1989**, *81*, 196–200.

[123] A. W. Hing, S. Vega, J. Schaefer, *J. Magn. Reson.* **1992**, *96*, 205–209.

[124] J. Schaefer, *Encycl. Magn. Reson.* **2007**, DOI 10.1002/9780470034590.emrstm0448.

[125] K. T. Mueller, T. P. Jarvie, D. J. Aurentz, B. W. RobertS, *Chem. Phys. Lett.* **1995**, *242*, 535–542.

[126] C. P. Jaroniec, C. Filip, R. G. Griffin, *J. Am. Chem. Soc.* **2002**, *124*, 10728–10742.

[127] A. W. Hing, S. Vega, J. Schaefer, *J. Magn. Reson. - Ser. A* **1993**, *103*, 151–162.

[128] C. P. Jaroniec, B. A. Tounge, J. Herzfeld, R. G. Griffin, *J. Am. Chem. Soc.* **2001**, *123*, 3507–3519.

[129] A. Lends, F. Ravotti, G. Zandomeneghi, A. Böckmann, M. Ernst, B. H. Meier, *J. Biomol. NMR* **2018**, *72*, 69–78.

[130] E. Daviso, M. T. Eddy, L. B. Andreas, R. G. Griffin, J. Herzfeld, *J. Biomol. NMR* **2013**, *55*, 257–265.

[131] L. B. Andreas, M. T. Eddy, J. J. Chou, R. G. Griffin, *J. Am. Chem. Soc.* **2012**, *134*, 7215–7218.

[132] N. Sinha, K. Schmidt-Rohr, M. Hong, *J. Magn. Reson.* **2004**, *168*, 358–365.

[133] L. B. Andreas, A. B. Barnes, B. Corzilius, J. J. Chou, E. A. Miller, M. Caporini, M. Rosay, R. G. Griffin, *Biochemistry* **2013**, *52*, 2774–2782.

[134] X. C. Zhang, M. C. Forster, E. Nimerovsky, K. T. Movellan, L. B. Andreas, *J. Phys. Chem. A* **2021**, *125*, 754–769.

[135] E. H. Anderson, *Proc. Natl. Acad. Sci. U. S. A.* **1946**, *32*, 120–128.

[136] P. Stothard, *Biotechniques* **2000**, *28*, 1102–1104.

[137] M. I. De Jonge, M. P. Bos, H. J. Hamstra, W. Jiskoot, P. Van Ulsen, J. Tommassen, L. Van Alphen, P. Van Der Ley, *Eur. J. Biochem.* **2002**, *269*, 5215–5223.

[138] J. M. Walker, *The Proteomics Protocols Handbook*, Springer, **2005**.

[139] V. Chevelkov, K. Faelber, A. Schrey, K. Rehbein, A. Diehl, B. Reif, *J. Am. Chem. Soc.* **2007**, *129*, 10195–10200.

[140] J. Pauli, B. Van Rossum, H. Förster, H. J. M. De Groot, H. Oschkinat, *J. Magn. Reson.* **2000**, *143*, 411–416.

[141] U. K. Laemmli, *Nature* **1970**, *227*, 680–685.

[142] M. Biology, *Methods in Molecular Biology, Vol. 1: Proteins*, **1985**.

[143] W. Lee, M. Tonelli, J. L. Markley, *Bioinformatics* **2015**, *31*, 1325–1327.

[144] V. Jirasko, N. A. Lakomek, S. Penzel, M. L. Fogeron, R. Bartenschlager, B. H. Meier, A. Böckmann, *ChemBioChem* **2020**, *21*, 1453–1460.

[145] W. J. DeGrip, *Ratio* **1998**, *674*, 667–674.

[146] A. Böckmann, C. Gardiennet, R. Verel, A. Hunkeler, A. Loquet, G. Pintacuda, L. Emsley, B. H. Meier, A. Lesage, *J. Biomol. NMR* **2009**, *45*, 319–327.

[147] I. Kucharska, B. Liang, N. Ursini, L. K. Tamm, *Biochemistry* **2016**, *55*, 5061–5072.

[148] C. R. Morcombe, K. W. Zilm, *J. Magn. Reson.* **2003**, *162*, 479–486.

[149] A. E. Bennett, C. M. Rienstra, M. Auger, K. V. Lakshmi, R. G. Griffin, *J. Chem. Phys.* **1995**, *103*, 6951–6958.

[150] A. J. Shaka, J. Keeler, T. Frenkiel, R. Freeman, *J. Magn. Reson.* **1983**, *52*, 335–338.

[151] D. H. Zhou, C. M. Rienstra, *J. Magn. Reson.* **2008**, *192*, 167–172.

[152] T. Gullion, D. B. Baker, M. S. Conradi, *J. Magn. Reson.* **1990**, *89*, 479–484.

[153] Y. Li, B. J. Wylie, C. M. Rienstra, *J. Magn. Reson.* **2006**, *179*, 206–216.

[154] E. E. Najbauer, L. B. Andreas, *J. Magn. Reson.* **2019**, *305*, 1–4.

[155] D. J. States, R. A. Haberkorn, D. J. Ruben, *J. Magn. Reson.* **1982**, *48*, 286–292.

[156] J. C. Lindon, A. G. Ferrige, *Prog. Nucl. Magn. Reson. Spectrosc.* **1980**, *14*, 27–66.

[157] R. Linser, B. Bardiaux, L. B. Andreas, S. G. Hyberts, V. K. Morris, G. Pintacuda, M. Sunde, A. H. Kwan, G. Wagner, *J. Am. Chem. Soc.* **2014**, *136*, 11002–11010.

[158] M. Liu, X. A. Mao, C. Ye, H. Huang, J. K. Nicholson, J. C. Lindon, *J. Magn. Reson.* **1998**, *132*, 125–129.

[159] E. Schmidt, P. Güntert, *J. Am. Chem. Soc.* **2012**, *134*, 12817–12829.

[160] P. Güntert, C. Mumenthaler, K. Wüthrich, *J. Mol. Biol.* **1997**, *273*, 283–298.

[161] P. Güntert, L. Buchner, *J. Biomol. NMR* **2015**, *62*, 453–471.

[162] L. Pauling, R. B. Corey, *Proc Natl Acad Sci U S A.* **1951**, *37*, 729–740.

[163] Y. Shen, A. Bax, *J. Biomol. NMR* **2013**, *56*, 227–241.

[164] E. F. Pettersen, T. D. Goddard, C. C. Huang, G. S. Couch, D. M. Greenblatt, E. C. Meng, T. E. Ferrin, *J. Comput. Chem.* **2004**, *25*, 1605–1612.

[165] S. P. Skinner, R. H. Fogh, W. Boucher, T. J. Ragan, L. G. Mureddu, G. W. Vuister, *J. Biomol. NMR* **2016**, *66*, 111–124.

[166] W. F. Vranken, W. Boucher, T. J. Stevens, R. H. Fogh, A. Pajon, M. Llinas, E. L. Ulrich, J. L. Markley, J. Ionides, E. D. Laue, *Proteins Struct. Funct. Genet.* **2005**, *59*, 687–696.

[167] J. Pauli, M. Baldus, B. Van Rossum, H. De Groot, H. Oschkinat, *ChemBioChem* **2001**, *2*, 272–281.

[168] G. Van Rossum, F. L. Drake, *Python 3 Reference Manual*, CreateSpace, Scotts Valley, CA, **2009**.

[169] V. MATLAB, *The MathWorks Inc., Natick, Massachusetts* **2016**.

[170] R. C. Team, others, **2013**.

[171] A. Mainz, S. Jehle, B. J. Van Rossum, H. Oschkinat, B. Reif, *J. Am. Chem. Soc.* **2009**, *131*, 15968–15969.

[172] R. Sarkar, A. Mainz, B. Busi, E. Barbet-Massin, M. Kranz, T. Hofmann, B. Reif, *Solid State Nucl. Magn. Reson.* **2016**, *76–77*, 7–14.

[173] J. P. Demers, P. Fricke, C. Shi, V. Chevelkov, A. Lange, *Prog. Nucl. Magn. Reson. Spectrosc.* **2018**, *109*, 51–78.

[174] R. A. Engh, R. Huber, *Acta Crystallogr. Sect. A* **1991**, *47*, 392–400.

[175] S. Wang, L. Shi, I. Kawamura, L. S. Brown, V. Ladizhansky, *Biophys. J.* **2011**, *101*, L23–L25.

[176] Y. Chen, Z. Zhang, X. Tang, J. Li, C. Glaubitz, J. Yang, *Angew. Chemie - Int. Ed.* **2014**, *53*, 5624–5628.

[177] C. Sohlenkamp, O. Geiger, *FEMS Microbiol. Rev.* **2015**, *40*, 133–159.

[178] H. Thie, T. Schirrmann, M. Paschke, S. Dübel, M. Hust, *N. Biotechnol.* **2008**, *25*, 49–54.

[179] E. Nimerovsky, K. Tekwani Movellan, X. C. Zhang, M. C. Forster, E. Najbauer, K. Xue, R. Dervişoğlu, K. Giller, C. Griesinger, S. Becker, L. B. Andreas, *Biomolecules* **2021**, *11*, DOI 10.3390/biom11050752.

[180] F. Hagn, M. Etzkorn, T. Raschle, G. Wagner, *J. Am. Chem. Soc.* **2013**, *135*, 1919–1925.

[181] P. M. Hwang, W. Y. Choy, E. I. Lo, L. Chen, J. D. Forman-Kay, C. R. H. Raetz, G. G. Privé, R. E. Bishop, L. E. Kay, *Proc. Natl. Acad. Sci. U. S. A.* **2002**, *99*, 13560–13565.

[182] V. E. Ahn, E. I. Lo, C. K. Engel, L. Chen, P. M. Hwang, L. E. Kay, R. E. Bishop, G. G. Privé, *EMBO J.* **2004**, *23*, 2931–2941.

[183] J. A. Cuesta-Seijo, C. Neale, M. A. Khan, J. Moktar, C. D. Tran, R. E. Bishop, R. Pomès, G. G. Privé, *Structure* **2010**, *18*, 1210–1219.

[184] I. R. Kleckner, M. P. Foster, *Biochim. Biophys. Acta - Proteins Proteomics* **2011**, *1814*, 942–968.

[185] S. Sun, Y. Han, S. Paramasivam, S. Yan, A. E. Siglin, J. C. Williams, I.-J. L. Byeon, J. Ahn, A. M. Gronenborn, T. Polenova, in *Methods Mol. Biol.*, **2012**, pp. 303–331.

[186] J. A. Purslow, B. Khatiwada, M. J. Bayro, V. Venditti, *Front. Mol. Biosci.* **2020**, *7*, 1–8.

[187] D. A. Bonsor, Q. Zhao, B. Schmidinger, E. Weiss, J. Wang, D. Deredge, R. Beadenkopf, B. Dow, W. Fischer, D. Beckett, P. L. Wintrode, R. Haas, E. J. Sundberg, *EMBO J.* **2018**, *37*, DOI 10.15252/embj.201798664.

[188] R. Conners, D. J. Hill, E. Borodina, C. Agnew, S. J. Daniell, N. M. Burton, R. B. Sessions, A. R. Clarke, L. E. Catto, D. Lammie, T. Wess, R. L. Brady, M. Virji, *EMBO J.* **2008**, *27*, 1779–1789.

[189] N. Korotkova, Y. Yang, I. Le Trong, E. Cota, B. Demeler, J. Marchant, W. E. Thomas, R. E. Stenkamp, S. L. Moseley, S. Matthews, *Mol. Microbiol.* **2008**, *67*, 420–434.

[190] A. K. Tchoupa, S. Lichtenegger, J. Reidl, C. R. Hauck, *Mol. Microbiol.* **2015**, *98*, 440–455.

[191] K. Moonens, Y. Hamway, M. Neddermann, M. Reschke, N. Tegtmeyer, T. Kruse, R. Kammerer, R. Mejías-Luque, B. B. Singer, S. Backert, M. Gerhard, H. Remaut, *EMBO J.* **2018**, *37*, DOI 10.15252/embj.201798665.

[192] K. Nishimura, R. Fu, T. A. Cross, *J. Magn. Reson.* **2001**, *152*, 227–233.

[193] C. P. Jaroniec, B. A. Tounge, C. M. Rienstra, J. Herzfeld, R. G. Griffin, *J. Magn. Reson.* **2000**, *146*, 132–139.

[194] J. R. Garbow, T. Gullion, in *Carbon-13 NMR Spectrosc. Biol. Syst.* (Ed.: N. Beckmann), Academic Press, San Diego, **1995**, pp. 65–115.

[195] D. A. Torchia, A. Szabo, *J. Magn. Reson.* **1982**, *49*, 107–121.

[196] E. R. Henry, A. Szabo, *J. Chem. Phys.* **1985**, *82*, 4753–4761.

[197] S. Asami, B. Reif, *J. Phys. Chem. B* **2017**, *121*, 8719–8730.

[198] J. D. Haller, P. Schanda, *J. Biomol. NMR* **2013**, *57*, 263–280.

[199] P. Schanda, M. Huber, J. Boisbouvier, B. H. Meier, M. Ernst, *Angew. Chemie - Int. Ed.* **2011**, *50*, 11005–11009.

[200] P. Schanda, B. H. Meier, M. Ernst, *J. Magn. Reson.* **2011**, *210*, 246–259.

[201] F. Hu, K. Schmidt-Rohr, M. Hong, *J. Am. Chem. Soc.* **2012**, *134*, 3703–3713.

7. Appendix

7.1. Plasmid insert DNA sequences

7.1.1. Opa60

CCATGGCTAGCGAAGACGGTGGTCGTGGCCCGTATGTTCAAGCGGACCTGGCGTA
TGCGTATGAGCACATTACCCACGATTACCCGGAGCCGACCGCGCCGAACAAGAA
CAAAATCAGCACCGTTAGCGACTACTTCCGTAACATTCGTACCCGTAGCGTGCAC
CCGCGTGTGAGCGTTGGTTATGACTTTGGTGGCTGGCGTATCGCGGCGGATTACG
CGCGTTATCGTAAGTGGAACAACAACAAATACAGCGTTAACATCGAGAACGTGC
GTATTCGTAAGGAAAACGGCATCCGTATTGACCGTAAAACCGAGAACCAGGAAA
ACGGTACCTTTCATGCGGTTAGCAGCCTGGGCCTGAGCGCGATCTACGACTTCCA
AATCAACGATAAGTTCAAGCCGTACATCGGTGCGCGTGTTGCGTATGGCCACGTG
CGTCACAGCATCGATAGCACCAAGAAAACCATTGAGGTGACCACCGTTCCGAGC
AACGCGCCGAACGGTGCGGTGACCACCTACAACACCGACCCGAAGACCCAGAAC
GATTATCAAAGCAACAGCATTCGTCGTGTGGGTCTGGGCGTTATCGCGGGTGTGG
GCTTTGACATTACCCCGAAACTGACCCTGGATGCGGGTTACCGTTATCACAACTG
GGGCCGTCTGGAGAATACCCGTTTTAAGACCCATGAGGCGAGCCTGGGCGTTCGC
TACCGTTTTAAGCTT

7.1.2. hCEACAM1-N

GGATCCGGCGGTGCGCAACTGACCACCGAGAGCATGCCGTTTAATGTGGCGGAG
GGTAAAGAGGTTCTGCTGCTGGTGCATAATCTGCCGCAGCAACTGTTCGGTTACA
GCTGGTATAAGGGCGAGCGTGTGGACGGCAACCGTCAGATCGTTGGTTATGCGAT
TGGTACCCAGCAAGCGACCCCGGGTCCGGCGAACAGCGGCCGTGAAACCATCTA
CCCGAACGCGAGCCTGCTGATTCAGAACGTGACCCAAAACGATACCGGCTTTTAT
ACCCTGCAAGTTATCAAGAGCGACCTGGTTAATGAAGAGGCGACCGGCCAATTCC
ATGTTTACTGAGCGGCCGC

7.2. Purification of Opa60, hCEACAM1-N and SH3

7.2.1. Purification of Opa60

The purification of Opa60 is documented in this section with SDS-PAGE gels. The expression is shown in Figure 16, the subsequent inclusion body preparation in Figure 17, the Co^{2+}-affinity chromatography step in Figure 18, the refolding of Opa60 in Figure 19 and the final gel filtration step in Figure 20.

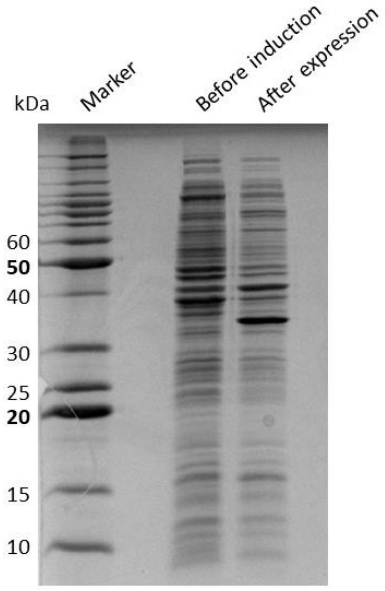

Figure 16: SDS-PAGE analysis of the expression of Opa60.

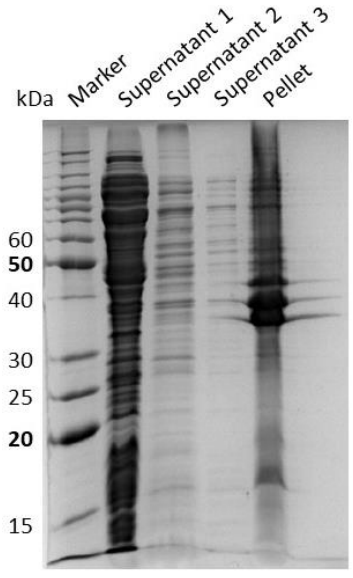

Figure 17: SDS-PAGE analysis of inclusion body preparation of Opa60.

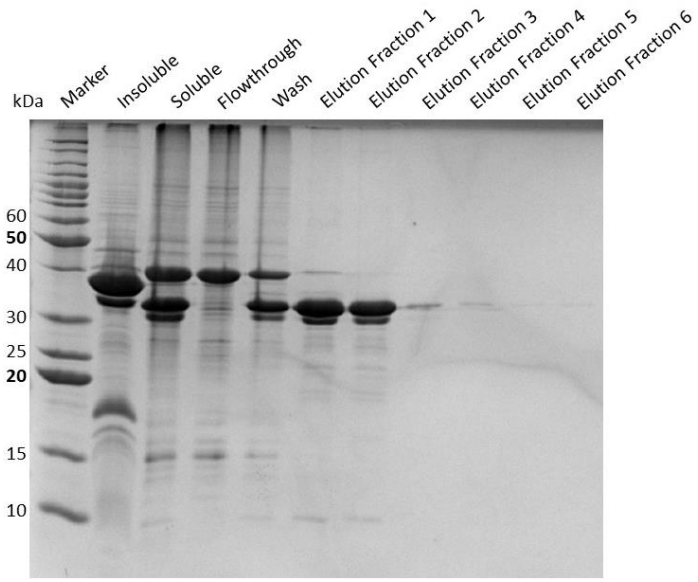

Figure 18: SDS-PAGE analysis of Co^{2+}-affinity chromatography of Opa60.

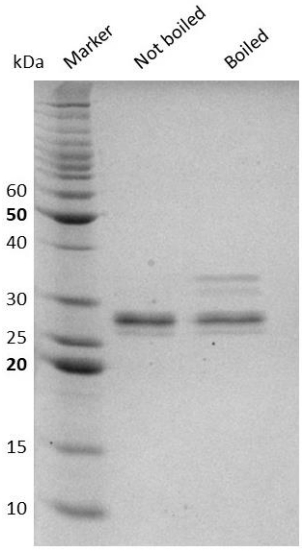

Figure 19: SDS-PAGE analysis of Opa60 refolding assessed by comparison of boiled and non-boiled samples.

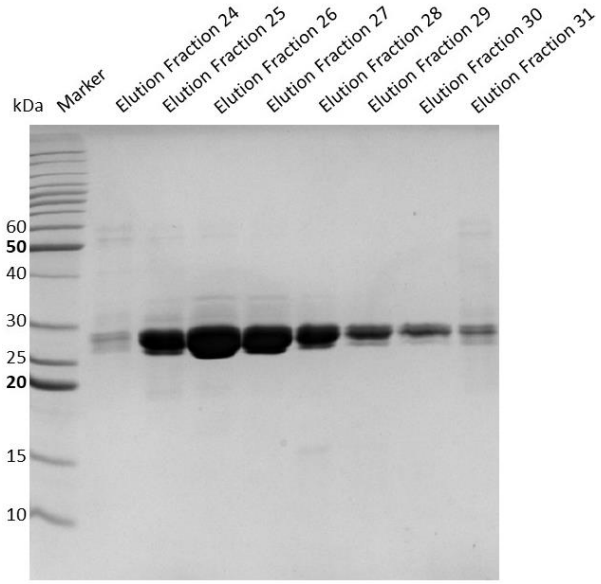

Figure 20: SDS-PAGE analysis of gel filtration purification of Opa60.

7.2.2. Purification of hCEACAM1-N

The purification process of hCEACAM1-N is documented in this section with SDS-PAGE gels. Figure 21 shows the gel of the expression of the protein, the subsequent centrifugation steps as well as the elution of the GST-affinity column. The thrombin digestion is documented in Figure 22 and the final gel filtration in Figure 23.

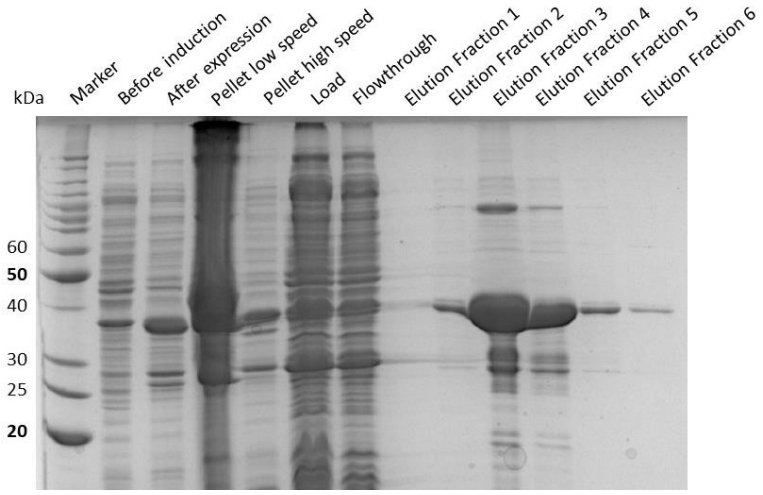

Figure 21: SDS-PAGE analysis of hCEACAM1-N expression as a GST-fusion protein. Gel contains samples before and after induction, the pellets from centrifugation steps to remove insoluble material as well as the supernatant (Load) which was loaded onto a GST-affinity column. Flowthrough and elutions (2 ml each) are indicated.

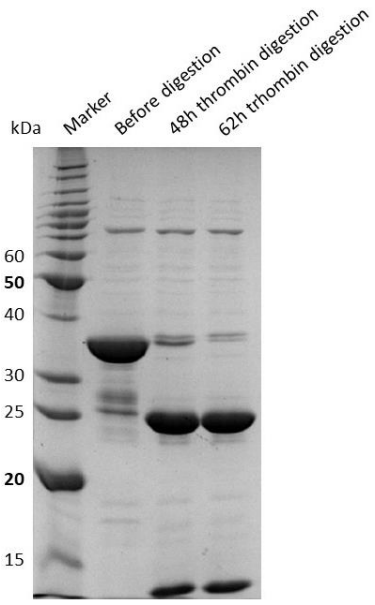

Figure 22: SDS-PAGE analysis of thrombin digestion of GST-hCEACAM1-N fusion protein.

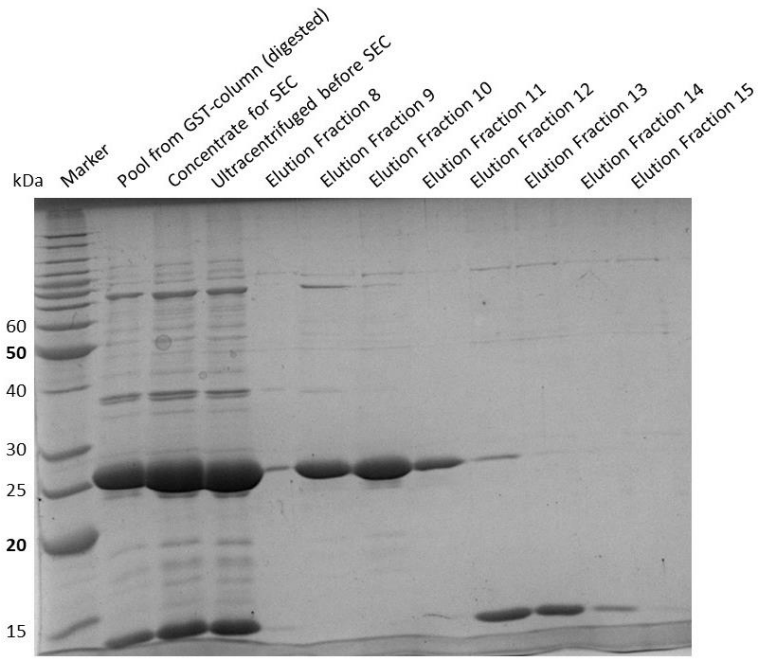

Figure 23: SDS-PAGE analysis of gel filtration purification of hCEACAM1-N after thrombin digestion of the fusion protein.

7.2.3. Purification of SH3

The purification of SH3 is documented in this section with SDS-PAGE gels. The expression and lysate purification by centrifugation is shown in Figure 24, the ion exchange chromatography purification in Figure 25 and the final gel filtration purification in Figure 26.

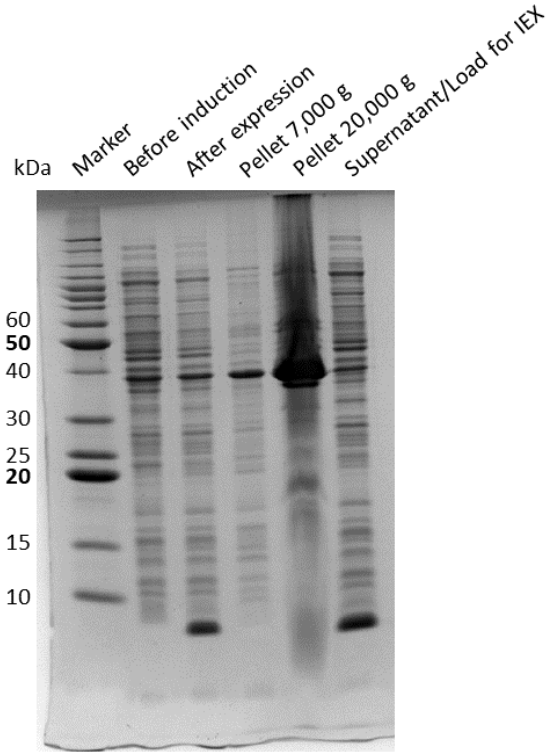

Figure 24: SDS-PAGE analysis of SH3 expression and purification by centrifugation. IEX: ion exchange chromatography.

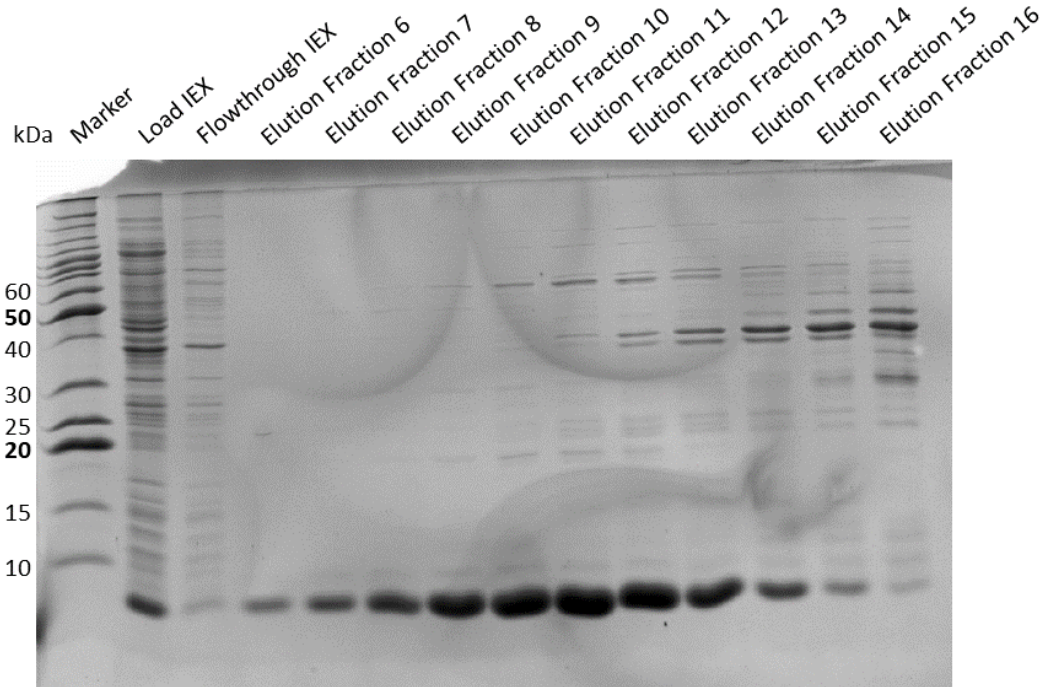

Figure 25: SDS-PAGE analysis of SH3 ion exchange chromatography purification. IEX: ion exchange chromatography.

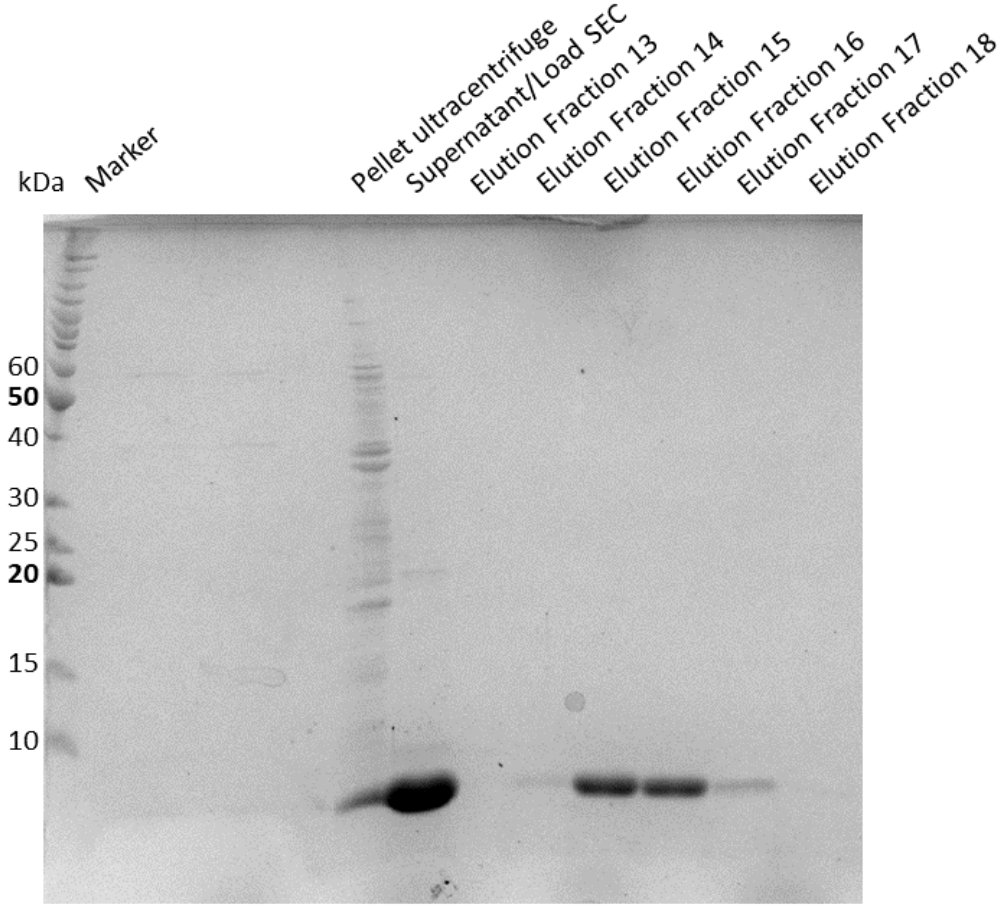

Figure 26: SDS-PAGE analysis of SH3 gel filtration purification. Sample was cleaned by ultracentrifugation before loading onto column.

7.3. Assignment of Opa60

7.3.1. Automated assignment with FLYA

The result of the FLYA automated assignment is shown if Figure 27 as the graphical output from the software.

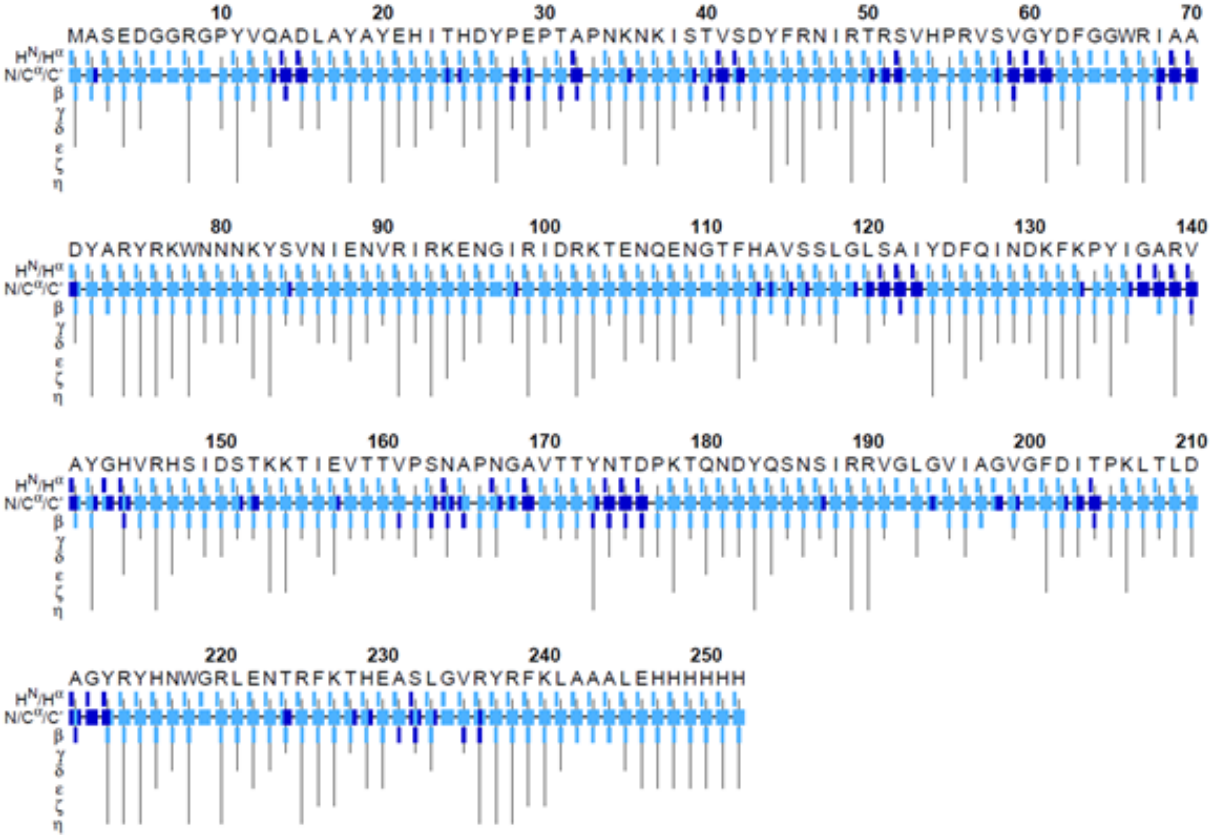

Figure 27: Output of the FLYA automated resonance assignment. Dark blue residues represent confident assignments based on the convergence of individual FLYA runs to the same assignment.

7.3.2. Resonance list of Opa60

A list of all Opa60 assignments from the perdeuterated sample is given in Table 7.

Table 7: Chemical shift assignments of Opa60.

Residue	Atom	Nucleus	Shift	Standard deviation	Assignments
G9	CA	13C	44.082	0.059	3
G9	HN	1H	8.297	0.030	6
G9	N	15N	108.843	0.228	7
P10	CA	13C	61.741	0.000	1
P10	CB	13C	32.310	0.000	1
Y11	C	13C	173.148	0.000	1

Y11	CA	13C	56.390	0.013	3
Y11	CB	13C	40.867	0.000	1
Y11	HN	1H	8.582	0.059	8
Y11	N	15N	114.401	0.175	9
V12	C	13C	173.577	0.000	1
V12	CA	13C	58.603	0.000	1
V12	CB	13C	34.875	0.000	1
V12	HN	1H	8.867	0.019	2
V12	N	15N	114.009	0.150	3
Q13	C	13C	173.491	0.053	2
Q13	CA	13C	53.856	0.057	5
Q13	CB	13C	31.959	0.051	2
Q13	HN	1H	9.147	0.046	10
Q13	N	15N	125.958	0.099	12
A14	C	13C	173.825	0.000	2
A14	CA	13C	50.386	0.033	6
A14	CB	13C	21.052	0.002	2
A14	HA	1H	5.195	0.000	1
A14	HN	1H	8.571	0.042	13
A14	N	15N	126.797	0.076	15
D15	C	13C	175.437	0.006	2
D15	CA	13C	52.376	0.149	4
D15	CB	13C	45.928	0.132	2
D15	HN	1H	8.954	0.038	13
D15	N	15N	117.950	0.095	15
L16	CA	13C	54.409	0.006	3
L16	CB	13C	42.448	0.000	1
L16	HN	1H	9.114	0.048	10
L16	N	15N	122.246	0.085	11
P55	CA	13C	60.813	0.000	1
R56	CA	13C	54.518	0.182	4
R56	CB	13C	34.224	0.062	2
R56	HA	1H	5.111	0.000	1
R56	HN	1H	9.083	0.034	6
R56	N	15N	123.172	0.215	8
V57	C	13C	173.814	0.000	1
V57	CA	13C	59.971	0.029	3

V57	CB	13C	34.070	0.000	1
V57	HN	1H	8.941	0.094	4
V57	N	15N	126.825	0.290	4
S58	C	13C	172.703	0.000	1
S58	CA	13C	56.922	0.007	2
S58	CB	13C	65.929	0.080	2
S58	HN	1H	9.197	0.044	7
S58	N	15N	116.946	0.115	8
V59	C	13C	173.561	0.021	2
V59	CA	13C	59.633	0.068	5
V59	CB	13C	34.059	0.042	2
V59	HN	1H	8.783	0.035	11
V59	N	15N	119.670	0.114	13
G60	C	13C	170.450	0.011	2
G60	CA	13C	45.157	0.045	5
G60	HN	1H	8.058	0.036	10
G60	N	15N	111.257	0.036	12
Y61	C	13C	172.363	0.000	2
Y61	CA	13C	57.806	0.044	5
Y61	CB	13C	42.642	0.008	2
Y61	HN	1H	9.000	0.041	10
Y61	N	15N	118.955	0.090	12
D62	C	13C	174.815	0.010	2
D62	CA	13C	51.971	0.106	5
D62	CB	13C	41.953	0.021	2
D62	HN	1H	7.979	0.051	13
D62	N	15N	126.978	0.049	15
F63	CA	13C	59.124	0.000	2
F63	CB	13C	38.562	0.000	1
F63	HN	1H	8.893	0.012	9
F63	N	15N	122.930	0.045	10
R67	C	13C	175.234	0.025	2
R67	CA	13C	54.579	0.044	5
R67	CB	13C	35.243	0.035	2
R67	HN	1H	9.860	0.054	8
R67	N	15N	118.751	0.104	10
I68	C	13C	174.619	0.009	2

I68	CA	13C	58.279	0.077	5
I68	CB	13C	40.609	0.038	2
I68	HN	1H	8.363	0.032	11
I68	N	15N	117.792	0.146	13
A69	C	13C	176.659	0.032	2
A69	CA	13C	51.281	0.079	6
A69	CB	13C	22.322	0.034	2
A69	HA	1H	5.184	0.000	1
A69	HN	1H	8.530	0.032	13
A69	N	15N	123.599	0.024	15
A70	C	13C	175.601	0.006	2
A70	CA	13C	49.653	0.066	6
A70	CB	13C	20.876	0.012	2
A70	HA	1H	5.943	0.000	1
A70	HN	1H	9.495	0.035	11
A70	N	15N	128.635	0.115	14
D71	C	13C	173.457	0.012	2
D71	CA	13C	52.150	0.081	5
D71	CB	13C	45.880	0.147	2
D71	HN	1H	9.338	0.034	11
D71	N	15N	117.853	0.097	14
Y72	C	13C	173.279	0.000	1
Y72	CA	13C	57.110	0.107	5
Y72	CB	13C	43.010	0.000	1
Y72	HN	1H	9.146	0.033	9
Y72	N	15N	117.815	0.052	10
A73	C	13C	174.304	0.000	1
A73	CA	13C	51.484	0.017	3
A73	CB	13C	23.045	0.000	1
A73	HN	1H	6.940	0.039	12
A73	N	15N	125.055	0.066	13
H113	CA	13C	54.480	0.086	4
H113	CB	13C	33.134	0.000	1
H113	HA	1H	5.475	0.000	1
H113	HN	1H	9.069	0.006	2
H113	N	15N	121.600	0.000	2
A114	CA	13C	52.547	0.092	4

A114	CB	13C	18.449	0.031	2
A114	HN	1H	8.986	0.063	4
A114	N	15N	125.251	0.160	7
V115	CA	13C	57.494	0.083	5
V115	CB	13C	32.392	0.028	2
V115	HN	1H	9.136	0.028	7
V115	N	15N	121.233	0.181	8
S116	C	13C	172.645	0.000	1
S116	CA	13C	57.498	0.072	2
S116	CB	13C	65.719	0.016	2
S116	HN	1H	8.112	0.010	5
S116	N	15N	111.081	0.111	6
S117	C	13C	172.700	0.000	1
S117	CA	13C	57.624	0.096	4
S117	CB	13C	64.833	0.472	2
S117	HN	1H	8.184	0.051	9
S117	N	15N	111.018	0.120	10
L118	C	13C	174.895	0.031	2
L118	CA	13C	53.664	0.009	3
L118	CB	13C	44.589	0.004	2
L118	HN	1H	8.406	0.058	10
L118	N	15N	133.016	0.130	11
G119	C	13C	171.434	0.001	2
G119	CA	13C	43.958	0.015	5
G119	HN	1H	9.292	0.030	10
G119	N	15N	113.843	0.114	12
L120	C	13C	174.803	0.002	2
L120	CA	13C	53.617	0.083	5
L120	CB	13C	45.632	0.112	2
L120	HN	1H	9.107	0.028	12
L120	N	15N	119.478	0.072	14
S121	C	13C	172.674	0.022	2
S121	CA	13C	57.026	0.026	4
S121	CB	13C	65.369	0.040	2
S121	HN	1H	9.085	0.018	11
S121	N	15N	117.888	0.084	12
A122	C	13C	175.626	0.009	2

A122	CA	13C	50.683	0.072	5
A122	CB	13C	20.720	0.000	2
A122	HN	1H	8.612	0.036	13
A122	N	15N	124.718	0.051	15
I123	C	13C	173.459	0.021	2
I123	CA	13C	60.739	0.057	5
I123	CB	13C	42.399	0.001	2
I123	HN	1H	9.425	0.042	13
I123	N	15N	121.934	0.107	14
Y124	C	13C	173.292	0.009	2
Y124	CA	13C	57.479	0.106	4
Y124	CB	13C	40.900	0.000	2
Y124	HN	1H	9.471	0.030	12
Y124	N	15N	127.863	0.057	13
D125	C	13C	174.556	0.000	1
D125	CA	13C	53.076	0.084	4
D125	CB	13C	42.659	0.000	1
D125	HA	1H	5.109	0.000	1
D125	HN	1H	7.617	0.035	9
D125	N	15N	125.443	0.088	11
K133	C	13C	174.030	0.000	1
K133	CA	13C	54.358	0.004	2
K133	HN	1H	8.684	0.040	5
K133	N	15N	122.617	0.116	5
P134	C	13C	173.144	0.000	1
P134	CA	13C	62.209	0.038	2
P134	CB	13C	31.557	0.000	1
Y135	C	13C	173.541	0.020	2
Y135	CA	13C	56.110	0.054	5
Y135	CB	13C	41.542	0.083	2
Y135	HN	1H	8.843	0.034	10
Y135	N	15N	117.921	0.085	12
I136	C	13C	173.500	0.051	2
I136	CA	13C	58.519	0.053	5
I136	CB	13C	42.388	0.015	2
I136	HN	1H	8.695	0.020	11
I136	N	15N	114.435	0.125	13

G137	C	13C	171.070	0.026	2
G137	CA	13C	46.863	0.041	5
G137	HN	1H	9.415	0.047	12
G137	N	15N	110.727	0.089	14
A138	C	13C	174.654	0.006	2
A138	CA	13C	49.960	0.024	6
A138	CB	13C	22.321	0.023	2
A138	HA	1H	5.245	0.000	1
A138	HN	1H	8.733	0.029	10
A138	N	15N	120.465	0.098	13
R139	C	13C	173.805	0.003	2
R139	CA	13C	54.494	0.033	5
R139	CB	13C	33.039	0.015	2
R139	HN	1H	8.247	0.035	11
R139	N	15N	121.314	0.043	13
V140	C	13C	173.125	0.038	2
V140	CA	13C	58.209	0.059	6
V140	CB	13C	33.894	0.001	2
V140	HA	1H	5.352	0.000	1
V140	HN	1H	9.082	0.034	13
V140	N	15N	124.509	0.068	15
A141	C	13C	176.291	0.021	2
A141	CA	13C	50.864	0.030	5
A141	CB	13C	22.675	0.004	2
A141	HN	1H	8.774	0.029	13
A141	N	15N	123.361	0.105	15
Y142	C	13C	174.288	0.002	2
Y142	CA	13C	56.195	0.036	4
Y142	CB	13C	39.288	0.044	2
Y142	HN	1H	9.753	0.037	10
Y142	N	15N	127.489	0.121	11
G143	C	13C	170.683	0.055	2
G143	CA	13C	45.047	0.026	5
G143	HN	1H	8.763	0.033	6
G143	N	15N	116.722	0.092	7
H144	CA	13C	52.808	0.000	2
H144	CB	13C	32.019	0.000	1

H144	HN	1H	8.647	0.014	5
H144	N	15N	122.793	0.074	6
V191	CA	13C	61.855	0.000	1
V191	CB	13C	31.570	0.000	1
G192	C	13C	171.772	0.004	2
G192	CA	13C	44.152	0.048	5
G192	HN	1H	8.552	0.035	7
G192	N	15N	112.776	0.101	8
L193	C	13C	174.985	0.000	1
L193	CA	13C	53.488	0.052	4
L193	CB	13C	46.766	0.009	2
L193	HA	1H	5.423	0.000	1
L193	HN	1H	7.729	0.036	8
L193	N	15N	120.169	0.152	9
G194	C	13C	171.896	0.000	1
G194	CA	13C	45.853	0.020	3
G194	HN	1H	9.119	0.036	8
G194	N	15N	108.236	0.154	9
V195	C	13C	173.559	0.000	1
V195	CA	13C	59.234	0.034	2
V195	CB	13C	35.836	0.000	1
V195	N	15N	114.093	0.000	1
I196	C	13C	173.611	0.013	2
I196	CA	13C	58.125	0.072	4
I196	CB	13C	40.414	0.012	2
I196	HN	1H	8.525	0.036	13
I196	N	15N	118.243	0.122	14
A197	C	13C	175.036	0.003	2
A197	CA	13C	51.241	0.044	5
A197	CB	13C	22.624	0.043	2
A197	HN	1H	9.230	0.039	11
A197	N	15N	122.905	0.123	13
G198	C	13C	171.471	0.011	2
G198	CA	13C	46.487	0.021	5
G198	HN	1H	7.478	0.038	12
G198	N	15N	105.821	0.034	14
V199	C	13C	172.993	0.008	2

V199	CA	13C	60.415	0.041	5
V199	CB	13C	35.034	0.048	2
V199	HN	1H	9.327	0.035	12
V199	N	15N	115.060	0.070	13
G200	C	13C	172.531	0.001	2
G200	CA	13C	43.381	0.021	5
G200	HN	1H	7.738	0.043	11
G200	N	15N	110.742	0.048	13
F201	C	13C	174.543	0.000	1
F201	HN	1H	9.388	0.030	7
F201	N	15N	122.828	0.089	7
P205	C	13C	176.979	0.000	1
P205	CA	13C	64.683	0.000	1
P205	CB	13C	31.540	0.000	1
K206	C	13C	174.599	0.044	2
K206	CA	13C	55.876	0.053	4
K206	CB	13C	33.993	0.096	2
K206	HN	1H	7.760	0.024	7
K206	N	15N	111.700	0.110	8
L207	C	13C	175.468	0.010	2
L207	CA	13C	53.851	0.077	4
L207	CB	13C	45.252	0.187	2
L207	HN	1H	7.489	0.023	7
L207	N	15N	121.001	0.103	7
T208	C	13C	173.629	0.042	2
T208	CA	13C	61.499	0.013	5
T208	CB	13C	72.390	0.009	2
T208	HN	1H	9.055	0.013	8
T208	N	15N	122.378	0.116	9
L209	C	13C	174.293	0.031	2
L209	CA	13C	53.948	0.085	6
L209	CB	13C	43.224	0.006	2
L209	HA	1H	4.947	0.000	1
L209	HN	1H	9.312	0.032	10
L209	N	15N	128.161	0.070	12
D210	C	13C	175.335	0.019	2
D210	CA	13C	52.702	0.051	5

D210	CB	13C	44.872	0.010	2
D210	HN	1H	9.072	0.037	11
D210	N	15N	126.969	0.171	14
A211	C	13C	175.161	0.010	2
A211	CA	13C	50.177	0.041	5
A211	CB	13C	20.316	0.001	2
A211	HN	1H	8.987	0.047	13
A211	N	15N	131.947	0.087	15
G212	C	13C	171.082	0.025	2
G212	CA	13C	45.610	0.045	5
G212	HN	1H	8.911	0.046	12
G212	N	15N	107.154	0.057	14
Y213	C	13C	174.610	0.018	2
Y213	CA	13C	55.477	0.044	5
Y213	CB	13C	42.714	0.033	2
Y213	HN	1H	9.612	0.035	12
Y213	N	15N	120.337	0.066	14
R214	C	13C	173.111	0.005	2
R214	CA	13C	54.877	0.094	5
R214	CB	13C	34.117	0.044	2
R214	HN	1H	8.350	0.030	11
R214	N	15N	124.595	0.076	13
Y215	C	13C	174.906	0.000	1
Y215	CA	13C	55.194	0.066	5
Y215	CB	13C	39.910	0.001	2
Y215	HN	1H	8.800	0.022	8
Y215	N	15N	126.196	0.125	10
H216	C	13C	172.731	0.031	2
H216	CA	13C	56.945	0.057	5
H216	CB	13C	35.034	0.018	2
H216	HN	1H	8.529	0.038	11
H216	N	15N	128.013	0.097	13
N217	C	13C	175.129	0.022	2
N217	CA	13C	51.517	0.049	2
N217	CB	13C	37.748	0.000	1
N217	HN	1H	7.672	0.035	7
N217	N	15N	126.514	0.027	8

W218	CA	13C	58.927	0.000	2
W218	CB	13C	27.040	0.000	1
W218	HN	1H	9.261	0.027	6
W218	N	15N	123.568	0.086	7
T224	CA	13C	61.486	0.006	2
T224	CB	13C	71.399	0.000	1
T224	N	15N	126.425	0.000	1
R225	C	13C	174.301	0.000	1
R225	CA	13C	54.963	0.064	4
R225	CB	13C	35.214	0.000	1
R225	HN	1H	9.310	0.017	8
R225	N	15N	128.000	0.170	9
F226	CA	13C	56.801	0.083	2
F226	CB	13C	42.191	0.123	2
F226	HN	1H	9.355	0.001	2
F226	N	15N	122.700	0.000	2
K227	C	13C	175.555	0.030	2
K227	CA	13C	54.204	0.025	4
K227	CB	13C	36.249	0.018	2
K227	HN	1H	8.483	0.029	7
K227	N	15N	126.614	0.052	8
T228	C	13C	173.339	0.035	2
T228	CA	13C	59.074	0.028	5
T228	CB	13C	72.074	0.010	2
T228	HN	1H	8.910	0.025	7
T228	N	15N	106.453	0.159	8
H229	C	13C	176.031	0.042	2
H229	CA	13C	55.328	0.029	4
H229	CB	13C	34.962	0.000	1
H229	HN	1H	8.499	0.017	6
H229	N	15N	119.135	0.123	8
E230	C	13C	175.430	0.000	1
E230	CA	13C	53.944	0.187	3
E230	CB	13C	31.708	0.000	1
E230	HA	1H	5.455	0.000	1
E230	HN	1H	9.537	0.043	11
E230	N	15N	120.654	0.062	11

A231	C	13C	175.828	0.000	1
A231	CA	13C	49.576	0.007	2
A231	CB	13C	22.279	0.000	1
A231	N	15N	123.233	0.193	2
S232	C	13C	172.096	0.019	2
S232	CA	13C	56.792	0.049	5
S232	CB	13C	66.303	0.009	2
S232	HN	1H	9.588	0.042	13
S232	N	15N	112.814	0.175	15
L233	C	13C	175.302	0.017	2
L233	CA	13C	53.307	0.045	5
L233	CB	13C	45.858	0.010	2
L233	HN	1H	8.217	0.033	11
L233	N	15N	120.384	0.046	12
G234	C	13C	172.579	0.019	2
G234	CA	13C	46.015	0.037	5
G234	HN	1H	9.193	0.051	11
G234	N	15N	111.840	0.048	13
V235	C	13C	173.558	0.000	1
V235	CA	13C	58.531	0.091	5
V235	CB	13C	34.820	0.017	2
V235	HN	1H	8.548	0.033	11
V235	N	15N	113.416	0.116	13
R236	C	13C	174.262	0.049	2
R236	CA	13C	52.824	0.098	5
R236	CB	13C	32.434	0.152	2
R236	HN	1H	9.341	0.019	9
R236	N	15N	123.504	0.042	11
Y237	CA	13C	60.439	0.000	2
Y237	CB	13C	41.401	0.000	1
Y237	HN	1H	9.421	0.044	9
Y237	N	15N	125.307	0.115	11
R238	CA	13C	55.960	0.003	2
R238	HN	1H	9.439	0.013	2
R238	N	15N	124.783	0.020	3

7.3.3. Projections of assignment spectra

In this section, projections of the assignment spectra are shown with assignments. The N-C projections of the hCONH spectrum is shown in Figure 28, of the hcaCBcaNH spectrum in Figure 29, of the hNcacoNH spectrum in Figure 30 and of the HNhhNH spectrum in Figure 31. Assignments where possible are given.

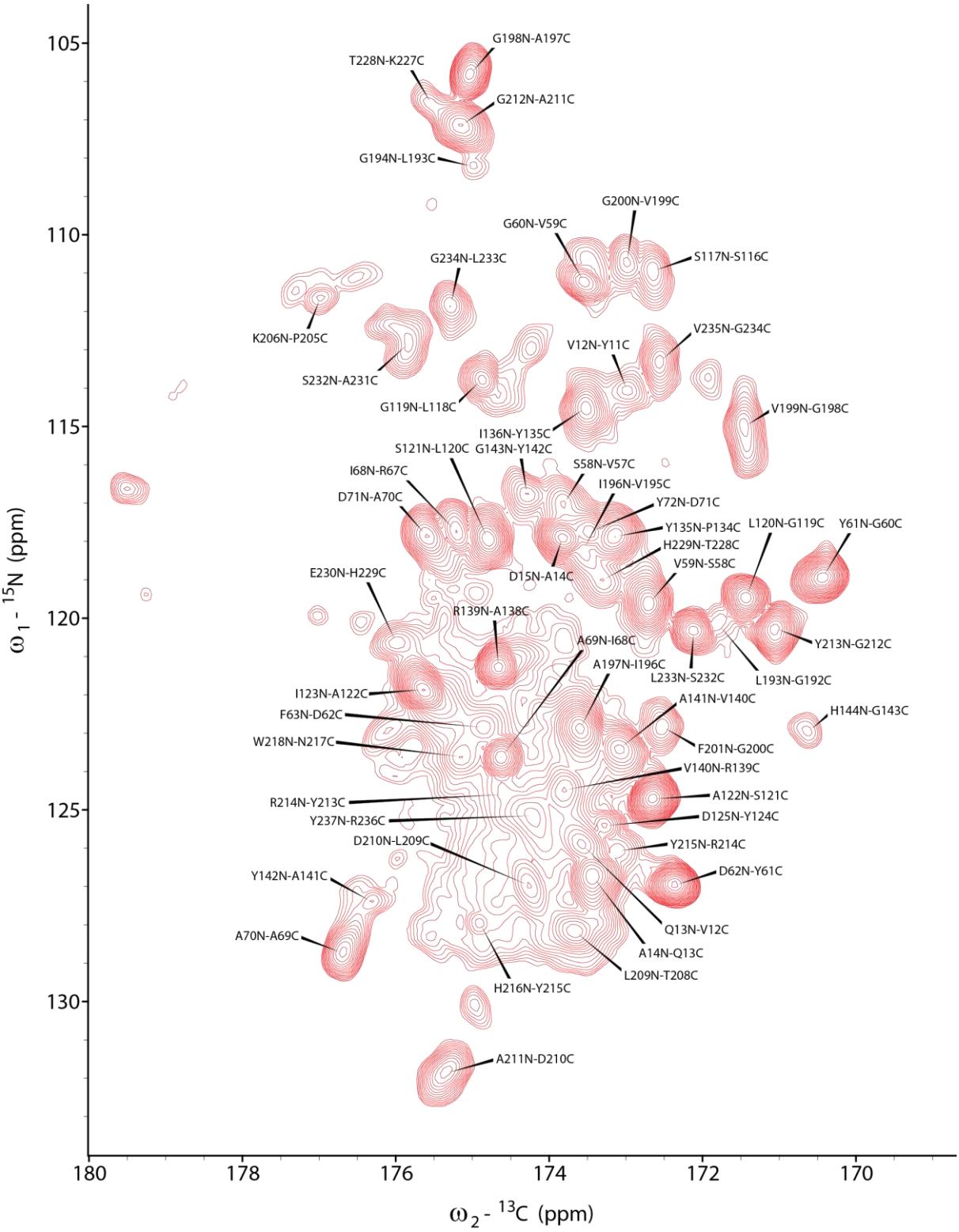

Figure 28: N-C projection of hCONH spectrum of perdeuterated Opa60 recorded at 800 MHz. Assignments are indicated.

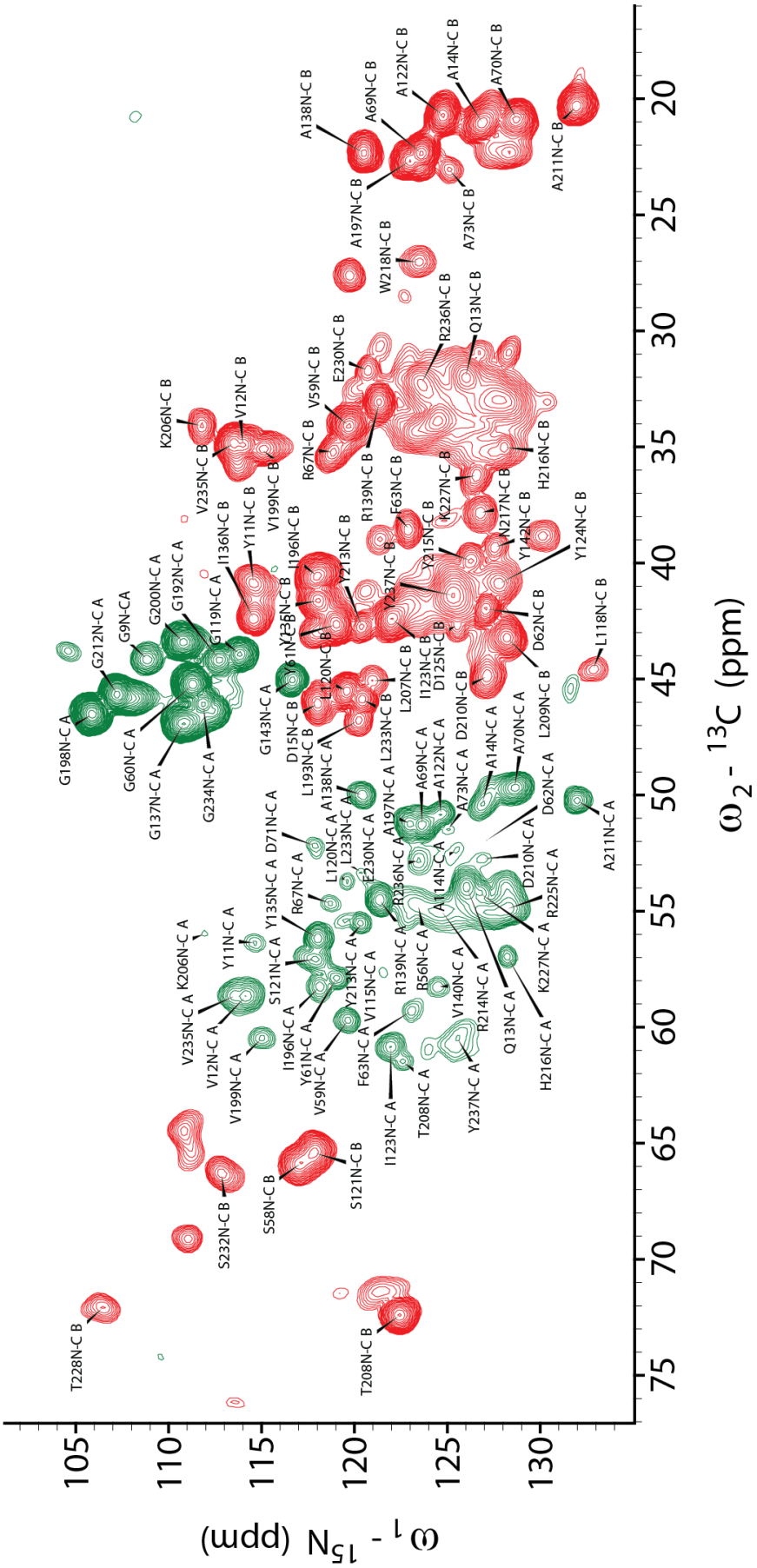

Figure 29: N-C projection of hcaCBcaNH spectrum of perdeuterated Opa60 recorded at 600 MHz. Assignments are indicated.

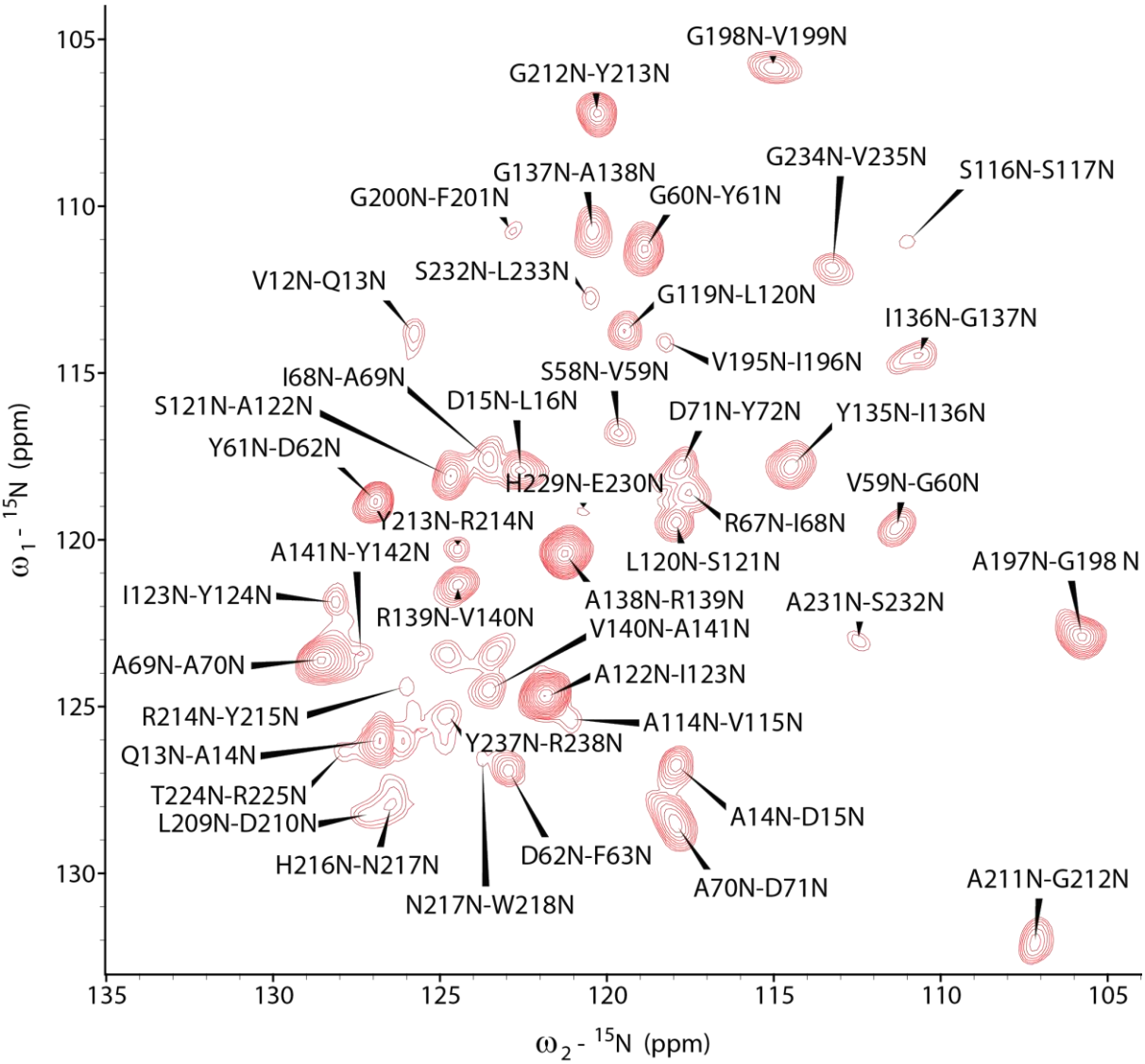

Figure 30: N-C projection of hNcacoNH spectrum of perdeuterated Opa60 recorded at 800 MHz. Assignments are indicated.

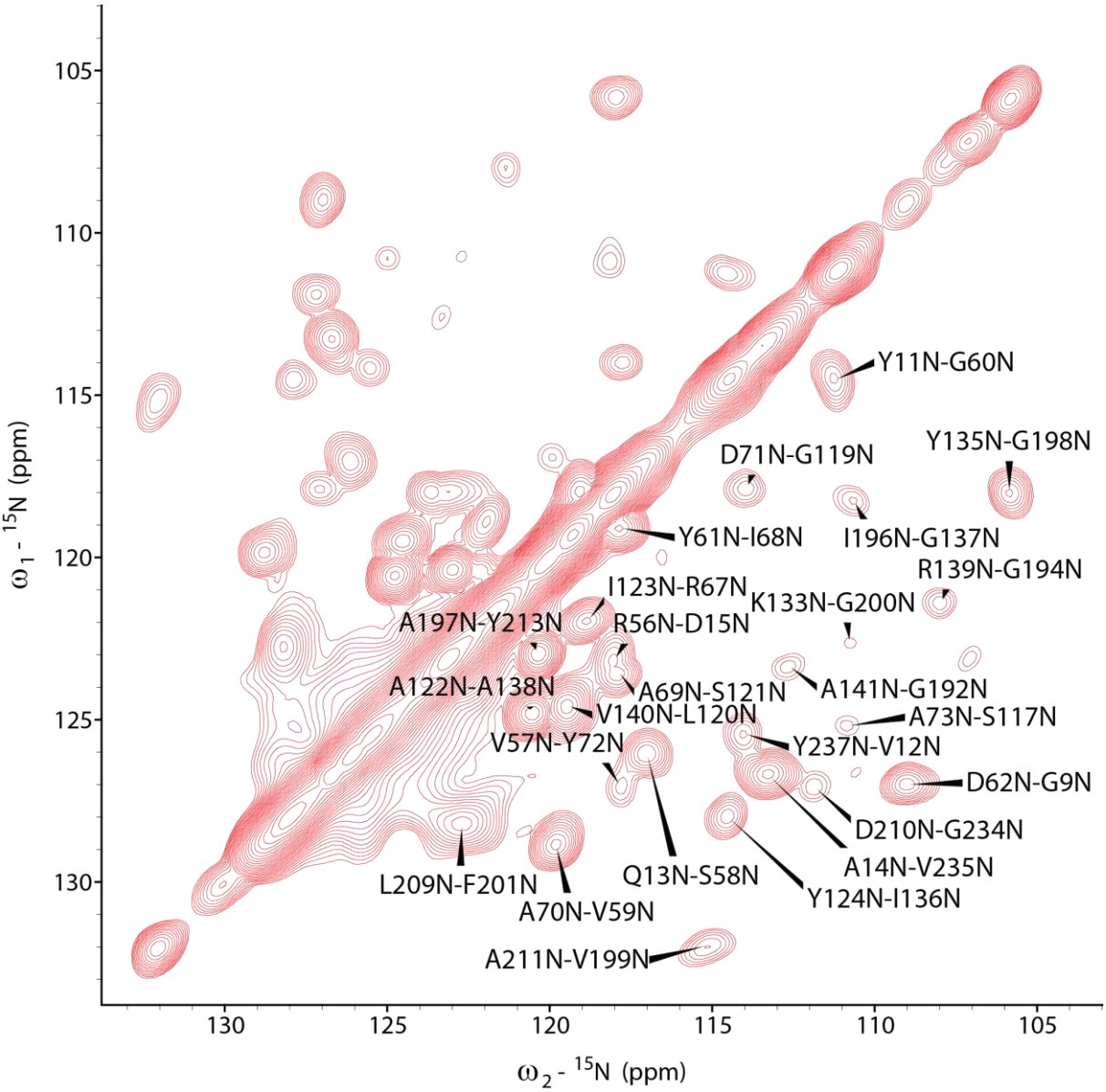

Figure 31: N-N projection of HNhhNH spectrum of perdeuterated Opa60 recorded at 800 MHz. Assignments are indicated on one side of the diagonal.

7.3.4. Cα-based backbone walk

An exemplary Cα-based backbone walk from resiude Asp125 to His113 is shown in Figure 32.

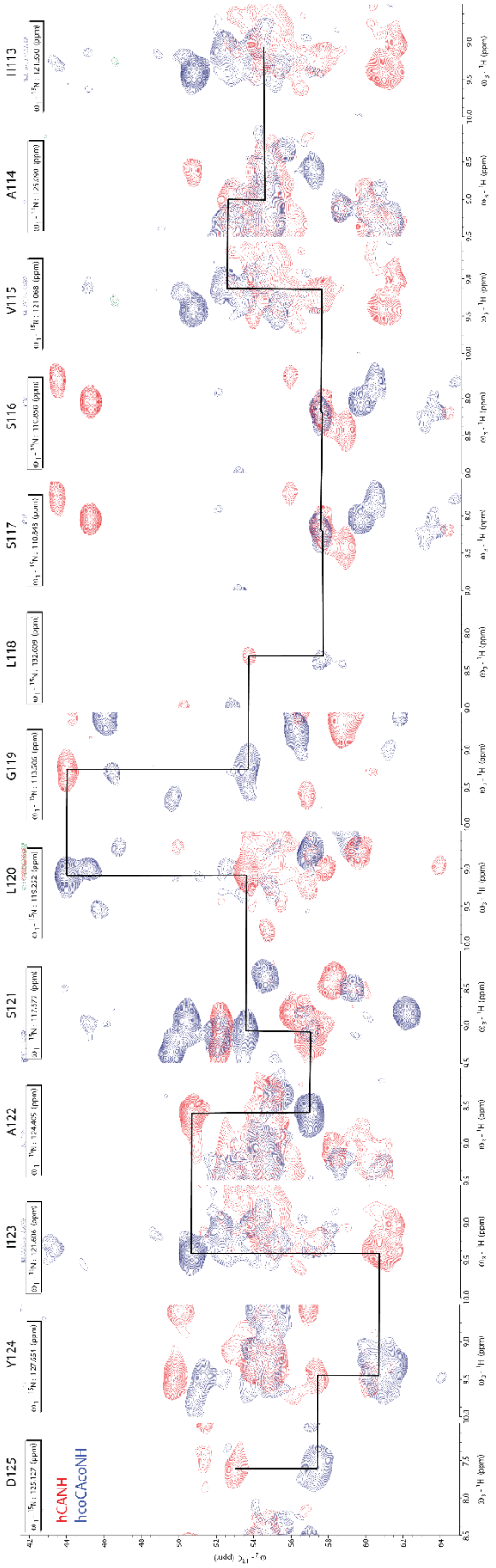

Figure 32: Cα-based backbone walk for residues Asp125 to His113.

7.3.5. hNH and INEPT-based hNH

An hNH spectrum as well as the overlay of CP- and J-based hNH spectra is shown in Figure 33. No major differences can be seen between the two transfer methods.

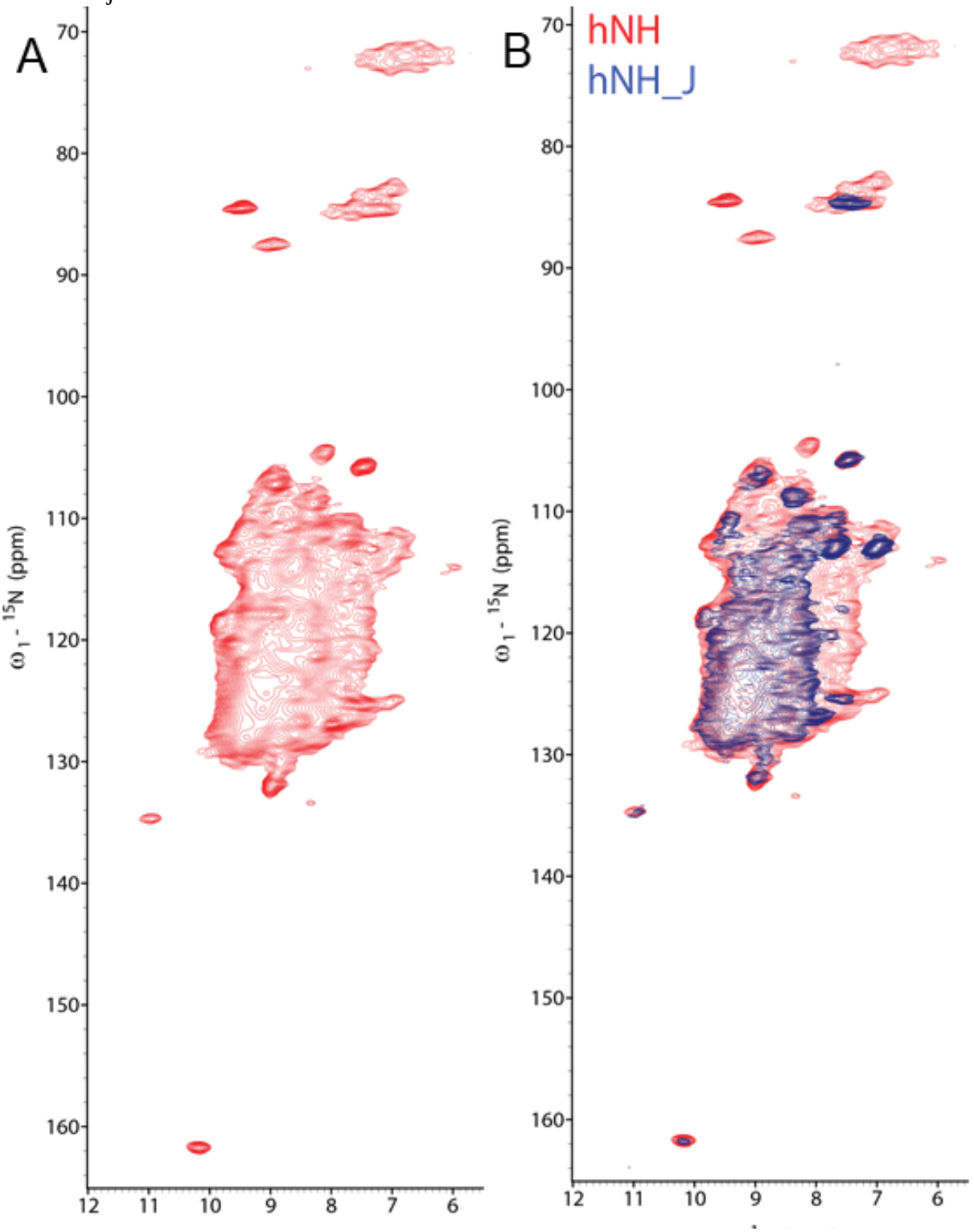

Figure 33: hNH spectra of perdeuterated Opa60 at 800 MHz. **A:** hNH spectrum. **B:** Overlay of CP-based hNH spectrum (red) with J-based hNH spectrum (blue).

7.3.6. FROSTY-spectra

An overlay of two hNH spectra of perdeuterated Opa60 is shown in Figure 34. At lower spinning and lower set temperature, a decrease in spectral resolution is observed yet no major difference can be found.

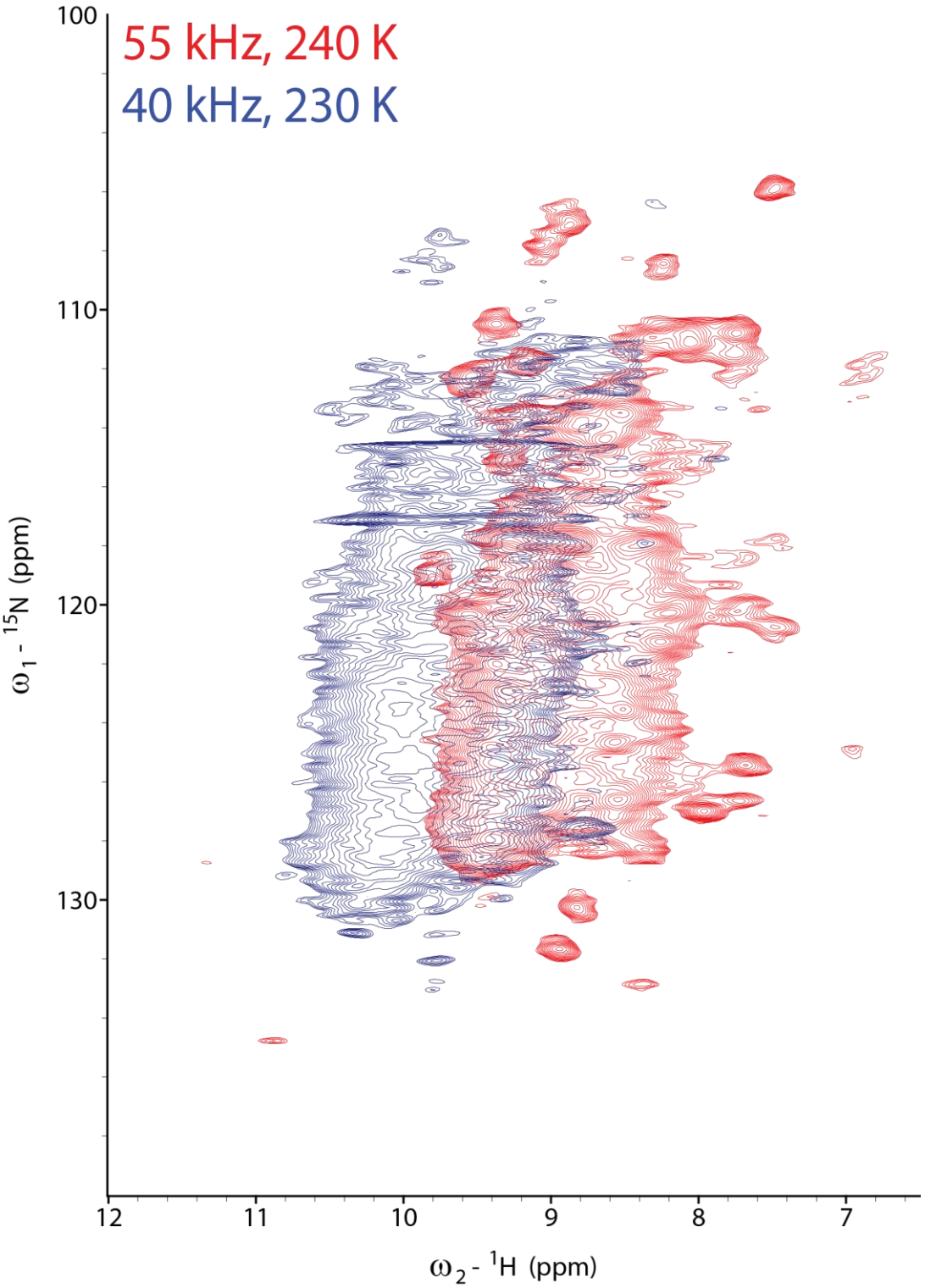

Figure 34: FROSTY-NMR hNH-spectra of perdeuterated Opa60. Samples contained 20% glycerol. MAS rate and set temperature are indicated. Contour levels and shifts have been adjusted for visibility.

7.4. Structure calculation of Opa60

7.4.1. Restraints

Distance restraints used in the Opa60 structure calculation which were derived from the HNhhNH spectrum are shown in Table 8. TALOS-N derived angle restraints are given in Table 9.

Table 8: Distance restraints used for the structure calculation of Opa60 derived from contacts found in the HNhhNH spectrum.

Contact		Upper limit [Å]	Lower limit [Å]
9 GLY H	62 ASP O	2	1.8
9 GLY N	62 ASP O	3	2.7
9 GLY O	62 ASP N	3	2.7
9 GLY O	62 ASP H	2	1.8
11 TYR H	60 GLY O	2	1.8
11 TYR N	60 GLY O	3	2.7
11 TYR O	60 GLY N	3	2.7
11 TYR O	60 GLY H	2	1.8
12 VAL H	237 TYR O	2	1.8
12 VAL N	237 TYR O	3	2.7
12 VAL O	237 TYR N	3	2.7
12 VAL O	237 TYR N	2	1.8
13 GLN H	58 SER O	2	1.8
13 GLN N	58 SER O	3	2.7
13 GLN O	58 SER N	3	2.7
13 GLN O	58 SER H	2	1.8
14 ALA H	235 VAL O	2	1.8
14 ALA N	235 VAL O	3	2.7
14 ALA O	235 VAL N	3	2.7
14 ALA O	235 VAL H	2	1.8
15 ASP H	56 ARG O	2	1.8
15 ASP N	56 ARG O	3	2.7
15 ASP O	56 ARG N	3	2.7

15 ASP O	56 ARG H	2	1.8
16 LEU H	233 LEU O	2	1.8
16 LEU N	233 LEU O	3	2.7
16 LEU O	233 LEU N	3	2.7
16 LEU O	233 LEU H	2	1.8
57 VAL H	72 TYR O	2	1.8
57 VAL N	72 TYR O	3	2.7
57 VAL O	72 TYR N	3	2.7
57 VAL O	72 TYR H	2	1.8
59 VAL H	70 ALA O	2	1.8
59 VAL N	70 ALA O	3	2.7
59 VAL O	70 ALA N	3	2.7
59 VAL O	70 ALA H	2	1.8
61 TYR H	68 ILE O	2	1.8
61 TYR N	68 ILE O	3	2.7
61 TYR O	68 ILE N	3	2.7
61 TYR O	68 ILE H	2	1.8
67 ARG H	123 ILE O	2	1.8
67 ARG N	123 ILE O	3	2.7
67 ARG O	123 ILE N	3	2.7
67 ARG O	123 ILE H	2	1.8
69 ALA H	121 SER O	2	1.8
69 ALA N	121 SER O	3	2.7
69 ALA O	121 SER N	3	2.7
69 ALA O	121 SER H	2	1.8
71 ASP H	119 GLY O	2	1.8
71 ASP N	119 GLY O	3	2.7
71 ASP O	119 GLY N	3	2.7
71 ASP O	119 GLY H	2	1.8
73 ALA H	117 SER O	2	1.8

73 ALA N	117 SER O	3	2.7
73 ALA O	117 SER N	3	2.7
73 ALA O	117 SER H	2	1.8
118 LEU H	142 TYR O	2	1.8
118 LEU N	142 TYR O	3	2.7
118 LEU O	142 TYR N	3	2.7
118 LEU O	142 TYR H	2	1.8
120 LEU H	140 VAL O	2	1.8
120 LEU N	140 VAL O	3	2.7
120 LEU O	140 VAL N	3	2.7
120 LEU O	140 VAL H	2	1.8
122 ALA H	138 ALA O	2	1.8
122 ALA N	138 ALA O	3	2.7
122 ALA O	138 ALA N	3	2.7
122 ALA O	138 ALA H	2	1.8
124 TYR H	136 ILE O	2	1.8
124 TYR N	136 ILE O	3	2.7
124 TYR O	136 ILE N	3	2.7
124 TYR O	136 ILE H	2	1.8
133 LYS H	200 GLY O	2	1.8
133 LYS N	200 GLY O	3	2.7
133 LYS O	200 GLY N	3	2.7
133 LYS O	200 GLY H	2	1.8
135 TYR H	198 GLY O	2	1.8
135 TYR N	198 GLY O	3	2.7
135 TYR O	198 GLY N	3	2.7
135 TYR O	198 GLY H	2	1.8
137 GLY H	196 ILE O	2	1.8
137 GLY N	196 ILE O	3	2.7
137 GLY O	196 ILE N	3	2.7
137 GLY O	196 ILE H	2	1.8

139 ARG H	194 GLY O	2	1.8
139 ARG N	194 GLY O	3	2.7
139 ARG O	194 GLY N	3	2.7
139 ARG O	194 GLY H	2	1.8
141 ALA H	192 GLY O	2	1.8
141 ALA N	192 GLY O	3	2.7
141 ALA O	192 GLY N	3	2.7
141 ALA O	192 GLY H	2	1.8
197 ALA H	213 TYR O	2	1.8
197 ALA N	213 TYR O	3	2.7
197 ALA O	213 TYR N	3	2.7
197 ALA O	213 TYR H	2	1.8
199 VAL H	211 ALA O	2	1.8
199 VAL N	211 ALA O	3	2.7
199 VAL O	211 ALA N	3	2.7
199 VAL O	211 ALA H	2	1.8
201 PHE H	209 LEU O	2	1.8
201 PHE N	209 LEU O	3	2.7
201 PHE O	209 LEU N	3	2.7
201 PHE O	209 LEU H	2	1.8
210 ASP H	234 GLY O	2	1.8
210 ASP N	234 GLY O	3	2.7
210 ASP O	234 GLY N	3	2.7
210 ASP O	234 GLY H	2	1.8
212 GLY H	232 SER O	2	1.8
212 GLY N	232 SER O	3	2.7
212 GLY O	232 SER N	3	2.7
212 GLY O	232 SER H	2	1.8
214 ARG H	230 GLU O	2	1.8
214 ARG N	230 GLU O	3	2.7

214 ARG O	230 GLU	N	3	2.7
214 ARG O	230 GLU	H	2	1.8

Table 9: TALOS-N derived angle restraints for the structure calculation of Opa60.

Residue	Angle		Angle margin	
10	PRO	PSI	129.2	174.0
11	TYR	PHI	-172.6	-132.6
11	TYR	PSI	144.2	184.2
12	VAL	PHI	-149.3	-109.3
12	VAL	PSI	126.5	166.5
13	GLN	PHI	-142.3	-92.2
13	GLN	PSI	115.5	155.5
14	ALA	PHI	-160.4	-106.6
14	ALA	PSI	115.4	177.7
15	ASP	PHI	-173.3	-107.2
15	ASP	PSI	125.2	191.8
56	ARG	PHI	-164.9	-81.1
56	ARG	PSI	115.1	162.6
57	VAL	PHI	-138.1	-93.8
57	VAL	PSI	113.7	158.2
58	SER	PHI	-160.4	-107.2
58	SER	PSI	126.1	174.5
59	VAL	PHI	-165.3	-97.7
59	VAL	PSI	118.9	169.5
60	GLY	PHI	-177.6	-112.7
60	GLY	PSI	142.8	182.8
61	TYR	PHI	-160.4	-118.1
61	TYR	PSI	122.0	162.0
62	ASP	PHI	-158.3	-65.3
62	ASP	PSI	90.3	158.7
68	ILE	PHI	-155.2	-107.5
68	ILE	PSI	121.6	176.9
69	ALA	PHI	-154.8	-100.9
69	ALA	PSI	113.7	153.7
70	ALA	PHI	-130.7	-88.4
70	ALA	PSI	109.8	158.7
71	ASP	PHI	-153.4	-108.7
71	ASP	PSI	137.5	177.5
72	TYR	PHI	-161.0	-109.7
72	TYR	PSI	119.6	165.3
73	ALA	PHI	-172.7	-100.3
73	ALA	PSI	118.8	178.5
115	VAL	PHI	-154.6	-98.9
115	VAL	PSI	136.2	176.2
116	SER	PHI	-173.1	-125.7
116	SER	PSI	143.6	183.6
117	SER	PHI	-163.4	-95.0
117	SER	PSI	115.3	155.3
118	LEU	PHI	-139.3	-92.3
118	LEU	PSI	109.9	149.9
119	GLY	PHI	-147.6	-90.0
119	GLY	PSI	132.9	172.9
120	LEU	PHI	-153.5	-112.0
120	LEU	PSI	117.8	157.8
121	SER	PHI	-153.9	-87.4
121	SER	PSI	119.6	163.2
122	ALA	PHI	-150.8	-99.3
122	ALA	PSI	110.9	159.6
123	ILE	PHI	-142.7	-102.7
123	ILE	PSI	112.8	156.3
124	TYR	PHI	-133.5	-85.1
124	TYR	PSI	115.4	155.6
125	ASP	PHI	-178.7	-54.0
125	ASP	PSI	85.7	194.9
133	LYS	PHI	-156.9	-16.9

133	LYS	PSI	95.5	188.3
135	TYR	PHI	-159.6	-104.3
135	TYR	PSI	132.8	172.8
136	ILE	PHI	-154.9	-114.9
136	ILE	PSI	128.3	168.3
138	ALA	PHI	-170.6	-112.7
138	ALA	PSI	134.7	174.7
139	ARG	PHI	-162.0	-89.8
139	ARG	PSI	112.0	154.2
140	VAL	PHI	-142.0	-96.3
140	VAL	PSI	122.2	169.4
141	ALA	PHI	-149.3	-105.6
141	ALA	PSI	111.7	151.7
142	TYR	PHI	-127.5	-87.5
142	TYR	PSI	104.3	144.3
144	HIS	PHI	-197.8	-58.9
144	HIS	PSI	89.7	192.4
193	LEU	PHI	-154.4	-114.4
193	LEU	PSI	129.7	170.6
194	GLY	PHI	-198.7	-90.7
194	GLY	PSI	124.8	202.0
195	VAL	PHI	-154.3	-110.3
195	VAL	PSI	129.6	169.6
196	ILE	PHI	-149.8	-109.8
196	ILE	PSI	122.9	162.9
197	ALA	PHI	-165.8	-123.5
197	ALA	PSI	136.2	178.5
198	GLY	PHI	-191.5	-134.6
198	GLY	PSI	145.9	195.1
199	VAL	PHI	-166.8	-118.5
199	VAL	PSI	132.3	172.3
207	LEU	PHI	-144.6	-104.6
207	LEU	PSI	112.2	152.2
208	THR	PHI	-139.7	-92.8
208	THR	PSI	110.3	150.3
209	LEU	PHI	-131.1	-91.1
209	LEU	PSI	107.9	147.9
210	ASP	PHI	-139.9	-95.0
210	ASP	PSI	107.9	147.9
212	GLY	PHI	-177.8	-115.9
212	GLY	PSI	136.2	190.5
213	TYR	PHI	-149.9	-109.9
213	TYR	PSI	125.8	165.8
214	ARG	PHI	-149.1	-91.6
214	ARG	PSI	114.4	154.4
215	TYR	PHI	-132.3	-92.3
215	TYR	PSI	113.9	153.9
216	HIS	PHI	-153.2	-113.2
216	HIS	PSI	114.3	156.4
225	ARG	PHI	-159.6	-95.3
225	ARG	PSI	113.8	163.4
226	PHE	PHI	-148.5	-97.8
226	PHE	PSI	112.5	152.5
227	LYS	PHI	-153.2	-103.5
227	LYS	PSI	129.6	171.7
228	THR	PHI	-160.3	-114.8
228	THR	PSI	130.5	170.5
229	HIS	PHI	-159.1	-109.8
229	HIS	PSI	126.5	166.5
230	GLU	PHI	-161.5	-87.7
230	GLU	PSI	125.2	165.2
231	ALA	PHI	-158.7	-113.5
231	ALA	PSI	128.9	168.9
232	SER	PHI	-162.2	-117.1
232	SER	PSI	130.4	170.4
233	LEU	PHI	-164.6	-107.2
233	LEU	PSI	122.2	164.7
235	VAL	PHI	-152.4	-112.4
235	VAL	PSI	133.8	173.8
236	ARG	PHI	-135.9	-95.9
236	ARG	PSI	107.2	163.8
237	TYR	PHI	-99.4	-42.7
237	TYR	PSI	114.1	164.4

7.4.2. CYANA output of Opa60 structure calculation

Structural statistics:

str	target	upper limits			lower limits			van der Waals			torsion angles		
	function	#	rms	max	#	rms	max	#	sum	max	#	rms	max
1	0.85	1	0.0510	0.55	0	0.0140	0.15	3	2.1	0.27	0	0.009	0.09
2	0.97	1	0.0513	0.55	0	0.0142	0.15	2	3.0	0.22	0	0.213	2.43
3	1.16	2	0.0625	0.55	0	0.0155	0.15	4	3.2	0.26	0	0.220	2.33
4	1.19	1	0.0517	0.55	0	0.0137	0.15	5	2.9	0.25	0	0.196	2.17
5	1.20	1	0.0510	0.55	0	0.0141	0.15	4	3.2	0.27	0	0.209	2.41
6	1.37	1	0.0511	0.55	0	0.0139	0.15	4	3.3	0.32	0	0.215	2.44
7	1.60	1	0.0514	0.55	0	0.0141	0.15	5	5.0	0.27	0	0.221	2.47
8	1.60	1	0.0508	0.55	0	0.0142	0.15	7	4.1	0.25	0	0.205	2.36
9	1.83	1	0.0601	0.55	0	0.0142	0.15	8	5.4	0.26	0	0.280	2.64
10	3.23	5	0.0990	0.55	0	0.0142	0.15	8	6.2	0.34	2	1.280	11.41
11	4.75	5	0.1243	0.85	0	0.0139	0.15	5	4.5	0.40	2	2.773	22.84
12	4.94	5	0.1319	0.88	0	0.0138	0.15	5	4.9	0.34	2	2.740	22.30
13	5.07	5	0.1325	0.91	0	0.0140	0.15	6	5.3	0.33	2	2.747	22.75
14	5.22	5	0.1244	0.86	0	0.0143	0.15	11	5.4	0.40	2	2.751	22.68
15	5.91	4	0.0944	0.59	0	0.0151	0.16	20	12.0	0.40	2	1.133	10.77
16	6.52	7	0.1577	1.40	0	0.0007	0.01	15	9.3	0.32	3	1.882	14.71
17	7.20	8	0.1484	0.99	0	0.0143	0.15	8	6.8	0.50	4	3.441	27.24
18	8.70	9	0.1659	0.90	0	0.0154	0.16	11	8.6	0.40	4	3.697	24.30
19	10.22	7	0.1767	1.17	0	0.0002	0.00	12	10.0	0.51	5	4.032	27.89
20	11.30	6	0.2326	1.58	0	0.0141	0.15	12	9.7	0.65	2	2.200	22.70

Ave 4.24 4 0.1034 0.78 0 0.0129 0.14 8 5.7 0.35 2 1.522 12.45

+/- 3.19 3 0.0530 0.30 0 0.0042 0.04 4 2.7 0.11 2 1.368 10.22

Min 0.85 1 0.0508 0.55 0 0.0002 0.00 2 2.1 0.22 0 0.009 0.09

Max 11.30 9 0.2326 1.58 0 0.0155 0.16 20 12.0 0.65 5 4.032 27.89

Cut 0.20 0.20 0.20 5.00

Restraints violated in 6 or more structures:

				#	mean	max.	1	5	10	15	20
Upper	O	VAL	12 - N	TYR 237	2.00	20	0.62	1.40	++++++++++++++*++++		
VdW	O	VAL	12 - N	TYR 237	2.75	13	0.18	0.21	+++ + ++++ ++* ++		
VdW	HA	VAL	161 - CD	PRO 162	2.60	7	0.12	0.27	+ + * + +++		

1 violated distance restraint.

2 violated van der Waals restraints.

0 violated angle restraints.

RMSDs for residues 1..252:

Average backbone RMSD to mean : 16.29 +/- 3.84 A (10.27..26.77 A; 20 structures)

Average heavy atom RMSD to mean : 16.58 +/- 3.72 A (10.77..26.59 A; 20 structures)

7.4.3. Hα contacts and assignments

A list of all assigned Hα atoms is given in Table 10. In the hXhhXH spectrum, between the following residues Hα-mediated contacts were identified:

- Asp15 – Gly234
- Tyr72 – Leu118
- Pro134 – Val199
- Ile136 – Ala197
- Val140 – Leu193

Table 10: Assignments of Hα atoms from the protonated Opa60 sample at 950 MHz. No stereospecific assignment for Gly residues is available. Chemical shifts are not referenced to DSS but rather stem from overlaying Cα atoms with the data from the perdeuterated sample.

Residue	Atom	Nucleus	Standard deviation	Assignments
Y11	HA	5.693	0.000	1
A14	HA	5.304	0.068	4
D15	HA	5.742	0.051	2
L16	HA	4.477	0.000	1
R56	HA	5.135	0.023	2
V57	HA	5.388	0.018	2
S58	HA	5.926	0.000	1
V59	HA	4.844	0.028	2
G60	QA	3.351	0.000	1
Y61	HA	4.364	0.035	2
D62	HA	5.011	0.047	4
F63	HA	4.283	0.000	1
R67	HA	5.665	0.000	1
I68	HA	5.504	0.079	2
A69	HA	5.163	0.020	2
A70	HA	5.934	0.023	3
D71	HA	5.822	0.032	3
Y72	HA	5.577	0.032	2
A73	HA	4.360	0.000	1
H113	HA	5.521	0.038	4
A114	HA	3.599	0.000	1
L118	HA	5.819	0.023	2
G119	QA	3.271	0.073	2
L120	HA	5.477	0.074	2
S121	HA	5.759	0.057	3
A122	HA	5.520	0.029	2
I123	HA	4.819	0.006	2
R124	HA	5.597	0.000	1
D125	HA	5.162	0.045	3
P134	HA	5.457	0.013	2
Y135	HA	5.614	0.000	1
I136	HA	5.418	0.030	3
A138	HA	5.308	0.064	4
V140	HA	5.328	0.024	2

A141	HA	5.594	0.013	2
H144	HA	5.397	0.049	2
L193	HA	5.460	0.029	3
V195	HA	5.321	0.000	1
I196	HA	5.595	0.000	1
A197	HA	5.441	0.040	3
V199	HA	4.492	0.005	2
P205	HA	4.465	0.000	1
K206	HA	4.369	0.000	1
L207	HA	5.605	0.000	1
T208	HA	5.196	0.078	4
L209	HA	5.064	0.085	3
D210	HA	5.575	0.000	1
A211	HA	5.561	0.001	2
G212	HA	5.112	0.005	2
Y213	HA	5.883	0.006	2
Y215	HA	5.517	0.000	1
H216	HA	4.328	0.048	2
N217	HA	4.968	0.040	3
W218	HA	4.238	0.045	2
T224	HA	5.612	0.000	1
R225	HA	5.729	0.000	1
K227	HA	5.665	0.002	2
T228	HA	5.736	0.000	1
E230	HA	5.457	0.002	2
A231	HA	5.805	0.000	1
L233	HA	5.478	0.021	3
G234	HA	5.209	0.000	1
V235	HA	5.325	0.043	2
R236	HA	5.304	0.045	2
Y237	HA	5.292	0.000	1
G9	HN	1H	0.030	6
G9	N	15N	0.228	7
P10	CA	13C	0.000	1
P10	CB	13C	0.000	1
Y11	C	13C	0.000	1
Y11	CA	13C	0.013	3

Y11	CB	13C	0.000	1
Y11	HN	1H	0.059	8

7.5. TREDOR

7.5.1. Restraints for SH3 structure calculation

Distance restraints for the SH3 structure calculation are given in Table 11 and TALOS-N angle restraints are given in Table 12.

Table 11: Distance restraints for SH3 structure calculation in CYANA format given as upper and lower boundaries (10% error imposed on fitted distance). Ambiguous restrains are given in the CYANA format with an upper/lower limit of 0 Å.

Contact		Upper limit [Å]	Lower limit [Å]
8 LEU N	8 LEU CG	3.44	2.82
8 LEU N	8 LEU CD1	3.91	3.2
8 LEU N	8 LEU CD2	0	0
8 LEU N	7 GLU CB	3.78	3.09
9 VAL N	9 VAL CG1	3.44	2.81
9 VAL N	9 VAL CG2	3.31	2.71
10 LEU N	10 LEU CG	3.92	3.21
10 LEU N	10 LEU CD1	0	0
10 LEU N	10 LEU CD2	0	0
10 LEU N	9 VAL CB	3.77	3.09
10 LEU N	9 VAL CG2	4.3	3.52
10 LEU N	61 LEU CD1	4.73	3.87
10 LEU N	61 LEU CD2	0	0
11 ALA N	10 LEU CD1	3.51	2.87
11 ALA N	10 LEU CD2	0	0
12 LEU N	12 LEU CG	3.6	2.94
12 LEU N	12 LEU CD1	0	0
12 LEU N	12 LEU CD2	0	0
12 LEU N	58 VAL CG1	4.28	3.51
13 TYR N	11 ALA CB	4.54	3.71
13 TYR N	27 LYS CB	4.77	3.9
14 ASP N	27 LYS CB	4.53	3.7
15 TYR N	14 ASP CB	4.77	3.24
15 TYR N	25 MET CG	4.45	3.64

15 TYR N	25 MET CE	5.05	4.01
16 GLN N	16 GLN CG	4.33	3.54
17 GLU N	17 GLU CG	3.76	3.08
17 GLU N	16 GLN CB	3.6	2.94
18 LYS N	18 LYS CG	3.3	2.7
18 LYS N	17 GLU CB	3.62	2.96
19 SER N	18 LYS CB	3.82	3.12
19 SER N	17 GLU CB	4.93	4.03
19 SER N	22 GLU CG	4.78	3.91
19 SER N	18 LYS CG	4.97	4.07
22 GLU N	22 GLU CG	3.91	3.2
22 GLU N	21 ARG CG	4.39	3.59
23 VAL N	23 VAL CG1	3.79	3.1
23 VAL N	22 GLU CB	3.18	2.6
23 VAL N	17 GLU CB	4.03	3.29
23 VAL N	23 VAL CG2	3.6	2.94
24 THR N	24 THR CG2	4.03	3.29
24 THR N	23 VAL CB	3.49	2.86
24 THR N	23 VAL CG2	4.23	3.46
24 THR N	17 GLU CB	4.34	3.55
25 MET N	25 MET CG	3.44	2.82
25 MET N	24 THR CG2	4.34	3.55
26 LYS N	26 LYS CG	4.02	3.29
26 LYS N	26 LYS CD	4.7	3.85
26 LYS N	25 MET CB	4.4	3.6
26 LYS N	25 MET CG	4.09	3.35
27 LYS N	27 LYS CG	4.02	3.29
27 LYS N	26 LYS CB	3.79	3.1
27 LYS N	26 LYS CD	4.69	3.83
28 GLY N	27 LYS CB	3.79	3.1
28 GLY N	27 LYS CG	3.79	3.1
28 GLY N	11 ALA CB	4.59	3.75
29 ASP N	11 ALA CB	4.7	3.85
30 ILE N	30 ILE CG1	3.49	2.86
30 ILE N	30 ILE CD1	4.5	3.68
31 LEU N	30 ILE CG1	4.03	3.29
31 LEU N	30 ILE CB	4.32	3.58

32 THR N	32 THR CG2	3.98	3.26
33 LEU N	33 LEU CD1	3.73	3.05
33 LEU N	33 LEU CD2	0	0
33 LEU N	33 LEU CG	4.07	3.33
33 LEU N	44 VAL CG1	4.75	3.88
34 LEU N	34 LEU CD1	4.31	3.52
34 LEU N	34 LEU CD2	0	0
34 LEU N	34 LEU CD1	4.06	3.32
34 LEU N	34 LEU CD2	0	0
34 LEU N	34 LEU CG	3.44	2.82
35 ASN N	43 LYS CB	4.32	3.53
35 ASN N	34 LEU CG	4.35	3.56
35 ASN N	33 LEU CD1	4.33	3.54
37 THR N	37 THR CG2	3.2	2.62
40 ASP N	39 LYS CB	3.78	3.1
40 ASP N	39 LYS CG	4.05	3.31
43 LYS N	43 LYS CG	4.2	3.44
43 LYS N	42 TRP CB	3.96	3.24
44 VAL N	44 VAL CG2	3.31	2.71
44 VAL N	44 VAL CG1	3.31	2.71
44 VAL N	43 LYS CB	4.02	3.29
44 VAL N	43 LYS CG	4.03	3.3
45 GLU N	44 VAL CG2	4.38	3.59
45 GLU N	44 VAL CG1	4.8	3.93
46 VAL N	46 VAL CG1	4.07	3.33
46 VAL N	50 GLN CB	4.56	3.73
49 ARG N	49 ARG CG	3.64	2.98
50 GLN N	50 GLN CG	3.6	2.95
50 GLN N	49 ARG CG	4.77	3.91
51 GLY N	50 GLN CB	3.36	2.75
51 GLY N	43 LYS CG	4.28	3.51
51 GLY N	23 VAL CG1	4.03	3.29
51 GLY N	23 VAL CG2	4.34	3.55
51 GLY N	23 VAL CB	4.46	3.65
53 VAL N	53 VAL CG1	3.33	2.73
53 VAL N	53 VAL CG2	3.44	2.81
55 ALA N	54 PRO CB	4.03	3.3

56 ALA N	55 ALA CB	3.79	3.1
57 TYR N	56 ALA CB	3.44	2.81
58 VAL N	58 VAL CG1	3.45	2.83
58 VAL N	58 VAL CG2	3.44	2.81
59 LYS N	59 LYS CG	3.79	3.1
59 LYS N	58 VAL CG2	4.34	3.55
59 LYS N	58 VAL CG1	4.78	3.91
60 LYS N	60 LYS CG	4.07	3.33
60 LYS N	59 LYS CG	4.11	3.36
60 LYS N	9 VAL CG1	4.11	3.36
61 LEU N	61 LEU CG	3.44	2.82
61 LEU N	60 LYS CB	4.09	3.34
61 LEU N	61 LEU CD1	4.16	3.4
61 LEU N	61 LEU CD2	0	0
41 TRP NE1	41 TRP CB	3.98	3.26
42 TRP NE1	42 TRP CB	4.03	3.29
42 TRP NE1	55 ALA CB	4.29	3.51
31 LEU N	31 LEU CD2	3.44	2.82
31 LEU N	31 LEU CG	4	3.27
31 LEU N	31 LEU CD1	0	0
31 LEU N	31 LEU CD2	0	0
8 LEU H	8 LEU C	3.1	2.54
9 VAL H	9 VAL C	2.95	2.41
10 LEU H	10 LEU C	2.89	2.37
13 TYR H	13 TYR C	2.81	2.3
13 TYR H	11 ALA C	3.17	2.59
15 TYR H	15 TYR C	2.73	2.23
15 TYR H	25 MET C	3.09	2.53
16 GLN H	16 GLN C	2.65	2.17
17 GLU H	17 GLU C	3.56	2.92
19 SER H	19 SER C	2.66	2.18
23 VAL H	23 VAL C	2.88	2.36
23 VAL H	51 GLY C	3.8	3.11
24 THR H	24 THR C	3.25	2.66
25 MET H	25 MET C	2.76	2.26
25 MET H	15 TYR C	2.76	2.26
27 LYS H	27 LYS C	3.69	3.02

27 LYS H	14 ASP C	3.17	3.17
27 LYS H	13 TYR C	3.56	2.92
28 GLY H	28 GLY C	3.15	2.57
28 GLY H	26 LYS C	3.78	3.1
29 ASP H	29 ASP C	3.04	2.48
29 ASP H	27 LYS C	2.95	2.41
33 LEU H	33 LEU C	2.88	2.36
33 LEU H	31 LEU C	4.2	3.44
35 ASN H	35 ASN C	2.65	2.17
35 ASN H	43 LYS C	3.14	2.57
41 TRP H	41 TRP C	2.75	2.25
41 TRP H	38 ASN C	3.25	2.66
42 TRP H	53 VAL C	3.05	2.49
42 TRP HE1	39 LYS C	4	3.28
42 TRP HE1	38 ASN C	3.76	3.08
42 TRP HE1	36 SER C	3.76	3.08
43 LYS H	43 LYS C	3.22	2.64
44 VAL H	44 VAL C	2.86	2.34
44 VAL H	51 GLY C	2.98	2.44
51 GLY H	51 GLY C	2.7	2.21
51 GLY H	44 VAL C	3.3	2.7
52 PHE H	52 PHE C	2.84	2.32
52 PHE H	21 ARG C	3.07	2.51
53 VAL H	53 VAL C	2.78	2.28
53 VAL H	42 TRP C	3.08	2.52
55 ALA H	55 ALA C	3.54	2.9
55 ALA H	53 VAL C	3.89	3.19
55 ALA H	41 TRP C	3.93	3.21
58 VAL H	58 VAL C	2.89	2.37
61 LEU H	61 LEU C	3.1	2.54
62 ASP H	62 ASP C	3.7	3.02
27 LYS H	14 ASP CG	3.17	2.59
24 THR H	17 GLU CD	4.27	3.49
18 LYS H	22 GLU CD	3.77	3.08
19 SER H	22 GLU CD	2.64	2.16
40 ASP H	38 ASN CG	2.94	2.41
41 TRP H	38 ASN CG	3.25	2.66

50 GLN HE21	45 GLU CD	3.45	2.82	

Table 12: TALOS-N angle restraints used for the structure calculation of SH3.

Residue		Angle	Angle margin	
8	LEU	PHI	-155.7	-108
8	LEU	PSI	135.2	175.2
9	VAL	PHI	-148.2	-108.2
9	VAL	PSI	131.4	171.4
10	LEU	PHI	-145.1	-105.1
10	LEU	PSI	116.5	156.5
11	ALA	PHI	-94.3	-52.8
11	ALA	PSI	106.7	146.7
12	LEU	PHI	-103.9	-63.1
12	LEU	PSI	-60.8	-19.7
13	TYR	PHI	-182.5	-131.4
13	TYR	PSI	138	178
16	GLN	PHI	-149.5	-86.9
16	GLN	PSI	109.4	169.9
23	VAL	PHI	-175.6	-72.5
23	VAL	PSI	129.5	177.3
24	THR	PHI	-132.1	-83.3
24	THR	PSI	111.5	151.5
25	MET	PHI	-151.5	-89.7
25	MET	PSI	113.5	171.6
26	LYS	PHI	-118	-56.7
26	LYS	PSI	130.5	170.5
27	LYS	PHI	-76.5	-36.5
27	LYS	PSI	113.2	153.2
29	ASP	PHI	-84.6	-44.6
29	ASP	PSI	126.3	166.3
30	ILE	PHI	-129.2	-89.2
30	ILE	PSI	104.5	144.5
31	LEU	PHI	-130	-89.1
31	LEU	PSI	103.8	158.4
32	THR	PHI	-97.3	-52.6
32	THR	PSI	107.9	147.9
33	LEU	PHI	-117.8	-50.3
33	LEU	PSI	88.7	168.2
34	LEU	PHI	-79.4	-39.4
34	LEU	PSI	-51.9	-11.9
36	SER	PHI	-88.8	-48.8
36	SER	PSI	-55.9	-15.9
37	THR	PHI	-85.9	-45.9
37	THR	PSI	-59.5	-19.5
38	ASN	PHI	-81.9	-41.9
39	LYS	PSI	-38.9	1.1
40	ASP	PHI	-105.7	-65.7
40	ASP	PSI	-29.6	10.4
41	TRP	PHI	-123.6	-67.1
41	TRP	PSI	112.2	159.1
42	TRP	PHI	-144.3	-104.3
42	TRP	PSI	114.3	175.6
43	LYS	PHI	-138.7	-62.6
43	LYS	PSI	103.5	151
44	VAL	PHI	-146.1	-94.4
44	VAL	PSI	112.9	178.5
50	GLN	PHI	-162.6	-88.7
50	GLN	PSI	132.5	172.5
51	GLY	PHI	153.3	193.3
51	GLY	PSI	-192.9	-152.9
52	PHE	PHI	-119.7	-67
52	PHE	PSI	116.3	163.4
53	VAL	PHI	-157.6	-104
53	VAL	PSI	124.7	175.2
54	PRO	PSI	108.5	148.5
55	ALA	PHI	-82.5	-42.5
55	ALA	PSI	-51.7	-11.7
56	ALA	PHI	-87.5	-47.5
56	ALA	PSI	-39.1	3.8

59	LYS	PHI	-149.6	-94.6	60	LYS	PSI	108.3	148.3
59	LYS	PSI	107.6	172.9	61	LEU	PHI	-104	-50.2
60	LYS	PHI	-99.5	-50.9	61	LEU	PSI	115.2	155.2

7.5.2. CYANA output of SH3 structure calculation

Structural statistics:

str	target	upper limits			lower limits			van der Waals			torsion angles	
	function	#	rms	max	#	rms	max	#	sum	max	#	rms	max
1	2.88	8	0.0703	0.38	3	0.0499	0.30	5	5.9	0.31	0	0.869	3.69
2	3.16	8	0.0948	0.62	0	0.0299	0.19	3	5.0	0.33	4	1.706	7.56
3	3.21	8	0.0988	0.61	1	0.0384	0.37	2	4.2	0.33	4	1.681	7.37
4	3.33	6	0.0978	0.64	2	0.0378	0.37	4	5.7	0.25	3	1.628	8.61
5	3.76	9	0.1041	0.62	1	0.0341	0.21	7	6.0	0.31	1	1.141	5.02
6	3.77	13	0.1085	0.59	2	0.0455	0.31	4	5.1	0.25	4	1.808	7.65
7	3.83	12	0.1048	0.57	3	0.0464	0.37	3	6.1	0.29	3	1.765	7.07
8	3.86	11	0.1058	0.62	3	0.0444	0.31	4	6.3	0.25	3	1.737	7.40
9	3.88	12	0.1062	0.57	2	0.0404	0.32	5	5.3	0.33	3	1.743	7.67
10	3.96	8	0.0957	0.57	3	0.0517	0.29	5	6.8	0.31	3	1.966	9.73
11	3.97	8	0.0954	0.67	6	0.0602	0.36	3	7.3	0.30	1	1.184	8.30
12	4.00	12	0.1064	0.63	1	0.0335	0.21	5	6.9	0.29	1	1.355	6.27
13	4.03	11	0.1120	0.66	3	0.0398	0.26	4	6.7	0.27	3	1.737	7.59
14	4.14	14	0.1162	0.71	2	0.0479	0.37	3	5.5	0.23	4	1.737	7.49
15	4.36	16	0.1170	0.56	2	0.0404	0.23	4	5.6	0.33	4	1.828	7.93
16	4.49	10	0.1055	0.58	3	0.0486	0.36	6	7.0	0.37	4	1.847	7.81
17	4.64	12	0.1108	0.59	3	0.0434	0.35	6	7.0	0.38	3	1.825	7.89
18	5.25	11	0.1067	0.60	2	0.0384	0.31	10	8.8	0.39	6	2.135	9.16

19 5.44 18 0.1269 0.58 2 0.0434 0.34 4 7.5 0.36 4 2.577 10.86

20 5.53 11 0.1113 0.62 2 0.0347 0.27 9 9.5 0.33 6 2.335 10.54

Ave 4.07 11 0.1048 0.60 2 0.0424 0.31 5 6.4 0.31 3 1.730 7.78

+/- 0.70 3 0.0111 0.06 1 0.0070 0.06 2 1.2 0.04 2 0.380 1.60

Min 2.88 6 0.0703 0.38 0 0.0299 0.19 2 4.2 0.23 0 0.869 3.69

Max 5.53 18 0.1269 0.71 6 0.0602 0.37 10 9.5 0.39 6 2.577 10.86

Cut 0.20 0.20 0.20 5.00

Restraints violated in 6 or more structures:

			#	mean	max.	1	5	10	15	20
Upper C	TYR 13 - H	LYS 27	3.56	11	0.23	0.50	+	++++++	+++ *	
Lower CB	ASP 14 - N	TYR 15	3.24	10	0.17	0.36	+	+++++*	++ +	
Upper C	ASP 14 - H	LYS 27	3.17	14	0.37	0.71	+++++ ++	+++*+	+ +	
Upper H	TYR 15 - C	MET 25	3.09	13	0.22	0.52	+	++++++	++*+++	
Upper C	TYR 15 - H	MET 25	2.76	13	0.29	0.61	+	+++ ++	++++++ *	
Lower CB	MET 25 - N	LYS 26	3.60	12	0.19	0.32	+	+++++*	+++++	
Upper N	ILE 30 - CG1	ILE 30	3.49	7	0.11	0.33	++ +	+ +	+ *	
Lower N	LEU 31 - CG	LEU 31	3.27	6	0.22	0.37	+++ *+	+		
N	LEU 31 - CD1	LEU 31								
N	LEU 31 - CD2	LEU 31								
Upper H	ASN 35 - C	ASN 35	2.65	13	0.25	0.63	++	+++ +*+++++	+	
Upper H	ASN 35 - C	LYS 43	3.14	6	0.16	0.38	+	+ * ++	+	
Upper C	SER 36 - HE1	TRP 42	3.76	16	0.23	0.44	+++ +++++	++++++ *+		
Upper CG	ASN 38 - H	ASP 40	2.94	6	0.12	0.45	+ ++	+*+		
Upper C	LYS 39 - HE1	TRP 42	4.00	16	0.43	0.59	+++ +++++	+++++* ++		

Upper C TRP 41 - H ALA 55 3.93 15 0.44 0.62 +++ ++*++ +++++ ++

Upper H TRP 42 - C VAL 53 3.05 15 0.28 0.51 +++ +++++ +++++ *+

Upper N VAL 53 - CG1 VAL 53 3.33 8 0.10 0.24 *+ + ++++ +

VdW N TYR 15 - O MET 25 2.75 9 0.20 0.38 + +++++ +* +

VdW O LYS 26 - C LYS 27 2.80 6 0.16 0.27 ++ +* + +

VdW N LYS 39 - H ASP 40 2.40 17 0.21 0.23 ++++++*++ ++++++++

VdW CE3 TRP 42 - H ALA 55 2.55 8 0.15 0.25 * + ++ ++ + +

VdW CG1 VAL 53 - C VAL 53 2.90 9 0.15 0.33 *+ + + ++++ +

Angle PSI ASP 40 -29.60 10.40 16 6.47 10.11 +++ +++++ ++++++*+

Angle PHI TRP 41 -123.60 -67.10 17 6.69 10.86 +++++++++ ++++++*+

Angle PSI PRO 54 108.50 148.50 15 5.21 8.38 +++ +++++ +++++ *+

16 violated distance restraints.

5 violated van der Waals restraints.

3 violated angle restraints.

RMSDs for residues 1..62:

Average backbone RMSD to mean : 3.19 +/- 1.03 A (1.50..5.16 A; 20 structures)

Average heavy atom RMSD to mean : 3.77 +/- 0.95 A (2.28..5.86 A; 20 structures)

7.5.3. Python script for RMSD calculation

The script works with the determined TREDOR structure loaded as “#0” and the SH3 PDB-structure (2NUZ) as “#1”.

```
from chimera import runCommand as rc
from Midas import rmsd
from math import sqrt
import numpy as np
```

```
rc("mm #1:11-58@CA,N,C,O #0.1-20:11-58@CA,N,C,O")
f = open("rmsd.txt", "a")
f.write("Resid" + "    " + "Struct" + "    " + "RMSD" + "\n")
for resid in range(7, 62):
        for struct in range(1, 21) :
                val = rmsd("#0.{0}:{1}@CA,N,C,O".format(struct, resid)
                f.write(str(resid) + "    " + str(struct) + "    " + str(val) + "\n")

f.close()
```

7.5.4. Multiple quantum terms

The multiple quantum artifacts are exemplarily shown in an H-CO TREDOR spectrum in Figure 35. When the ^{13}C carrier frequency was shifted by 20 ppm, the artifacts also shifted by 20 ppm and could thus be placed away from the signal of interest.

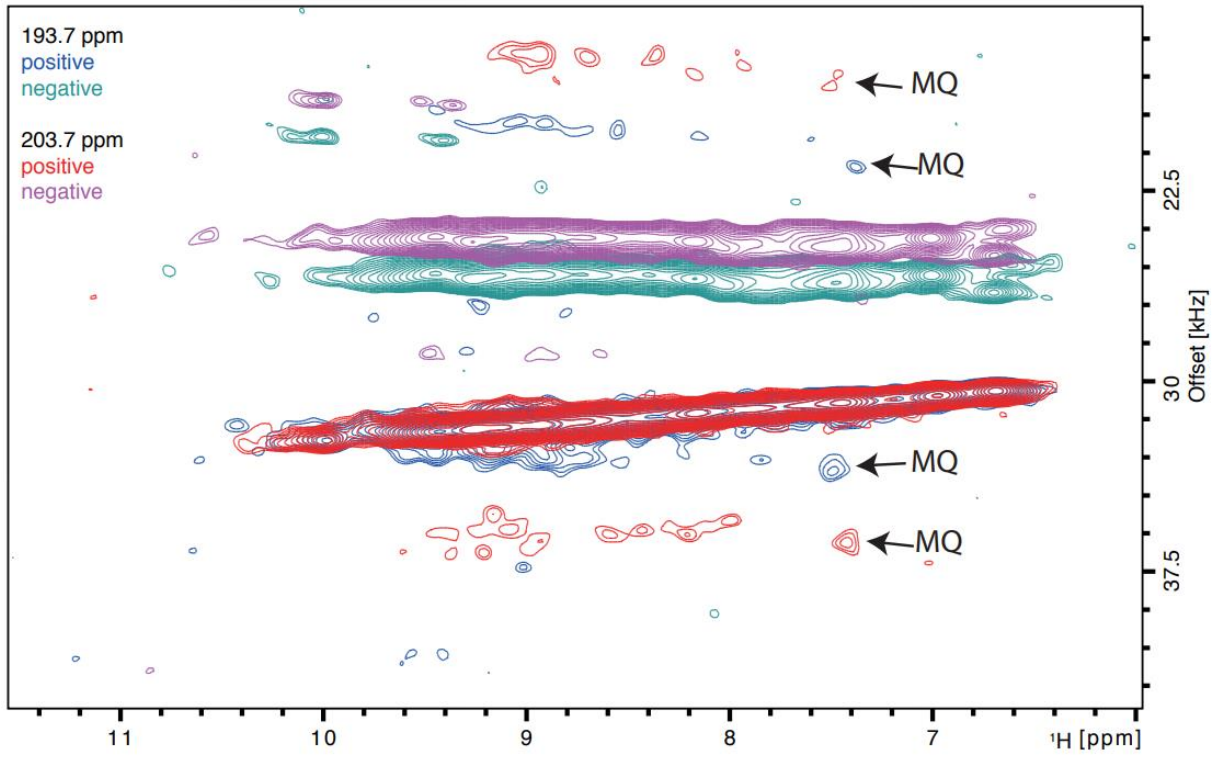

Figure 35: Multiple quantum (MQ) artifacts in TREDOR H-CO spectrum with two different ^{13}C carrier frequencies. The artifacts are labeled and shifting the offset by 20 ppm also shifts the artifacts, thus enabling to place them away from the signal of interest.

7.5.5. Transverse coherence decay

Table 13: T_2 relaxation times as measured in hNH and TREDOR spectra for every residue in SH3 for which the rate could be determined.

Residue	hNH T_2 [ms]	TREDOR T_2 [ms]
7 Glu	19.55	3.87
8 Leu	68.45	4.51
9 Val	67.61	3.52
10 Leu	64.02	4.68
1 1Ala	103.95	0.91
12 Leu	78.37	3.98
13 Tyr	84.67	4.93
14 Asp	109.89	4.79
15 Tyr	74.18	5.17
16 Gln	136.61	5.30
17 Glu	88.34	5.72
18 Lys	83.61	4.42
19 Ser	65.40	5.72
22 Glu	74.35	3.57
23 Val	101.01	4.03
24 Thr	118.62	4.86
25 Met	79.74	3.90
26 Lys	108.70	4.21
27 Lys	106.27	3.73
28 Gly	70.32	6.40
29 Asp	75.13	5.23
30 Ile	91.49	3.59
31 Leu	70.18	3.87
32 Thr	90.33	4.92
33 Leu	98.91	4.46
34 Leu	64.94	4.34
35 Asn	56.15	4.02
37 Thr	70.08	5.82
38 Asn	69.74	4.46
39 Lys	92.85	4.16
40 Asp	49.85	5.12
41 Trp	64.31	3.27
41 Trp Nε1	53.30	4.73
42 Trp	72.10	9.68
42 Trp Nε1	162.07	5.81
43 Lys	86.43	4.08
44 Val	76.05	3.05
45 Glu	79.11	5.30
49 Arg	52.88	6.50
50 Gln	75.24	5.29
51 Gly	69.54	9.48
52 Phe	104.60	4.98
53 Val	77.04	3.50
55 Ala	93.37	4.64
56 Ala	73.42	4.73
57 Tyr	85.84	3.94
58 Val	86.13	3.35
59 Lys	60.28	3.14
60 Lys	119.19	3.64
61 Leu	85.76	3.88